



EXCELENCIA  
MARÍA  
DE MAEZTU



 IFISC \*

 **Universitat**  
de les Illes Balears

 **CSIC**

**PROCEEDINGS OF THE 2021  
SURF@IFISC FELLOWSHIPS**

## Proceedings of the 2021 SURF@IFISC Fellowships

The SURF (Summer Undergraduate Research Fellowships) Program is offered by IFISC since 2013 (only interrupted in 2020 due to the Covid-19 pandemic) with the goal of attracting excellent undergraduate students with majors compatible with IFISC research lines and offers Summer internships at IFISC, typically during the month of July, advised by members of IFISC Claustro.

SURF attracted for the Summer of 2021 a total of 67 candidates (55 male and 12 female) from 28 universities and coming from 7 different countries, with Spain and UK with 5 candidates or more, from which 7 candidates were selected, although one fellowship could not be finally filled.

These are the proceedings:

1. Miguel Ángel González Casado (advisors David Sánchez and José J. Ramasco), *Analysis of the socioeconomic status in the United Kingdom from linguistic variation in Twitter*
2. Dimitrios Chalkiadakis, Rodrigo Martínez, Roberta Zambrini, and Gian Luca Giorgi, *The role of dissipation in Quantum Reservoir Computing*
3. Elsa Rodríguez García and Massimiliano Zanin, *Is air transport recovering from COVID-19? Dynamics of European airfares between November 2020 and June 2021*
4. Guillermo Pérez de Arenaza Pozo, Pere Colet, and Damià Gomila, *Power grid stability in scenarios of large renewable penetration*
5. Bernat Ramis (advisor Tobias Galla), *Game theory and the evolution of cancer*
6. Jorge Valencia, Emilio Hernández-García, and Cristóbal López Emilio Hernández-García, *Particle motion in a Bose-Einstein Condensate*

# Analysis of the socioeconomic status in the United Kingdom from linguistic variation in Twitter

Miguel Ángel González Casado

Supervisors: David Sánchez and José J. Ramasco

Instituto de Física Interdisciplinar y Sistemas Complejos, IFISC (CSIC-UIB)  
Campus Universitat de les Illes Balears, E-07122 Palma de Mallorca, Spain

## Abstract

Language fulfills a crucial social function, unveiling the social background of the speaker. The purpose of this project is to investigate if there exists a correlation between the language usage's geographic distribution in the United Kingdom, specifically the usage of *standard* and *non standard* expressions in English, and the socioeconomic status of English speakers. To do so, we use the data provided by Twitter and the so-called socioeconomic status' indicators. First, we conduct a general analysis about the mentioned geographic distribution, in order to discuss the quality and relevance of the research and the scope of the main results. Second, we study two specific indicators so as to determine if they are good predictors of the sociolinguistic variance: the GVA per Ceremonial County in England, and the rental price of one-bedroom flats per district in London. Interestingly, we find a positive correlation in the latter case, between the usage of standard expressions and the London districts with a higher housing rental price, and we show as well how important it is to choose a correct resolution in the geographic distribution to reveal sociolinguistic differences between inhabitants of the UK.

## 1 Introduction

Language fulfills a basic *semantic* function, in the sense that it is used to transmit meaningful concepts, allowing people within a community to communicate among themselves [1]. On the other hand, language is highly variable, it changes in geographical space and along social dimensions, since people belonging to different social groups or hierarchies and living in different places tend to use different words and expressions due to their economic and educational level, their adherence to social rules and the contexts in which they interact. In this sense, language fulfills a *social* function as well, helping to organize the social world identifying boundaries between social groups, understanding social rules and hierarchies, and shaping the own social identity [2].

Understanding and making a quantitative analysis of this sociolinguistic variability is not trivial at all, and to do so Sociolinguistics has historically used the so-called *linguistic variants* [3]. Linguistic variants are defined as the spectrum of different ways to transmit the same semantic information but with a change in grammar, spelling, vocabulary, etc., that gives information about the social background of the speaker<sup>1</sup>. Studying the usage of linguistic variants enables to identify the connection between language and the social status of the speakers [4]. Specifically, this research focuses in the correlation between the geographic distribution of the usage of *standard* and *non-standard* linguistic variants and the socioeconomic status of the speaker. Although treated later in detail, all in all *standard* linguistic variants could be understood as variants constructed based on the 'official' rules of the language, commonly associated with a higher economic position and high education, whereas *non-standard* variants

---

<sup>1</sup>If two variants transmit the same semantic information, the fact that the speaker chooses one or the other depends not on this semantic content, but in other factors like education, context, formality, related to their socioeconomic status [4].

could be understood as deviations from this 'official' rules, commonly associated with less formal situations, low educational level and a lower economic position [5]. The approach taken by traditional Sociolinguistics to study this sociolinguistic variability via linguistic variants was to use surveys and small experiments in controlled environments where they observe the subjects [6]. Both are limited methods owing to the small number of individuals one can handle in this kind of studies, and the intrinsic bias one could introduce just but controlling the context in which the experiment takes place. Nonetheless, this is currently changing due to the advent of social media and computer social sciences, which offers a renewed approach to the problem. Social media data offers a source for studying the interaction between language, geography and social factors [7] in uncontrolled environments (in other words, closer to real interactions) at a large scale, without a limitation in the number of individuals studied.

Specifically, this project is based on the data provided by Twitter, and the legit question that arises once proposed a study based on the data provided by social media to extract conclusions of sociological character: *Is not the study intrinsically biased and limited due to the nature of the data used?* Short answer, yes, but to be fair we need to give a more specific answer to understand the scope of the analysis. To begin with, there exists a basic bias when posing that every person uses Twitter regardless their gender, age or social class. Besides, one cannot discard the influence over the data owing to Bots presence, people using VPNs or even, since this project compares the English usage between standard and non standard variants, the influence of the predictive keyboard implemented in the vast majority of smartphones, correcting automatically non standard expressions with standard expressions. Furthermore, in Twitter, people interact in a very specific way, a pretty colloquial one [8], something that need to be taken into account when drawing *general* conclusions from the experiment.

Nonetheless, this is not conclusive by any means, and the topic is currently being tested, discussed and improved. For instance, one can argue that VPNs usage is not sufficiently democratized so that it entails a real problem if the statistical sample is big enough. On the other hand, it is possible to detect and eliminate tweets from Bots by identifying duplicated tweets or unusual behavior. Besides, there are plenty of studies focused on analyzing how representative of the society and the socioeconomic status Twitter-provided data is. For instance, there are meta-analysis which study the biases introduced in studies relying on information provided by Twitter [9], their scope and their limitations. Also, in the same paper they analyze in which sector of the population by gender and age these studies are more representative; in [10] they analyze how to treat and interpret such thing as *gender* in studies based on data provided by Twitter, and in [5] they investigate if socioeconomic status' indicators such as level of income, fraction of owners of the land or population density obtained via Twitter correlate between them in a similar way to how they correlate if the same information is provided by the official census data. About the bias introduced by the predictive keyboard, we did not find anything substantial, but it is expected that its influence produces a poorer correlation in the analysis. Finally, there are whole studies dedicated to design new methods to reduce biases and improve the results obtained [11], as well as meta-analysis focused on revising, correcting and completing old studies with updated information [12].

All in all, results from this and other articles must be comprehended jointly with the meta-analysis and papers cited, discussing their own validity and taking into account the influence different elements could have in the correlation degree, determining the scope of the conclusions drawn. All things considered, the question this project wants to answer is: Is there any correlation between the usage of *standard* and *non standard* linguistic variants in Twitter and the socioeconomic status of the speakers?

## 2 Method

The main purpose of this research is to use geolocalized data provided by Twitter to clarify if there exists any correlation between the usage of a more or less standard English in the United Kingdom, and a higher or lower socioeconomic status of the person using it, through indicators like the rental

price of the flats, the educational level or the Gross Value Added. In order to do it, the main strategy is divided in two phases: first, we analyze the geographic distribution of the language usage with different resolutions using the data provided by Twitter; second, we analyze if there exists a correlation between such geographic distribution and the geographic distribution of different socioeconomic status' indicators, provided by official sources like the Office for National Statistics. But before going deeper in details, we need to explain which standard and non standard linguistic variants this study focuses on.

## 2.1 Linguistic Variants: Standard vs Non-Standard

To analyze the mentioned correlation between the *standard/non standard* language usage and the socioeconomic status, we need to find which are the adequate linguistic markers able to represent, with a sufficiently large statistic sample, these sociolinguistic variations. To begin with, *standard* language is defined as the collection of every grammatical structure constructed following the 'official' rules of the language. In relation with it, *non standard* language is defined as the collection of every grammatical structure constructed making mistakes with respect to these 'official' rules, understanding mistakes as deviations from the rule changing only the grammatical structure and leaving unaffected the semantic content. For instance: 'Do you know where my dog is?' vs 'Do you know where is my dog?'. Both expressions transmit the same semantic information without ambiguity, but just the first one is grammatically *correct*. From these definitions, now it is necessary to define specifically which *standard* and *non standard* markers are going to be used to study the existence of the mentioned correlation.

The linguistic marker we chose to represent the *standard - non standard* usage defined above was the third person singular of the present tense of the verbs, whose grammatically correct structure is constructed adding *-s* to the verb in the affirmative form, and adding *doesn't/does not* before the verb in the negative form. As the grammatically incorrect structure we chose the one constructed without the *-s* in the affirmative form, and with *don't/do not* in the negative form<sup>2</sup>. In particular, we used a list of 98 reference verbs presented in the Appendix A chosen for being commonly used verbs, open to be widen in the future.

## 2.2 The Socioeconomic Status

In relation with the previous section, we must define as well what the socioeconomic status is and how one can make a quantitative analysis of it. The socioeconomic status is [5] an abstract variable which quantifies the position of a person at a social, educational, economic, cultural and labor level with respect to the rest within the society and conditions how they are going to behave and interact inside it. Such status is measured as a combination of the so-called socioeconomic status' indicators, quantitative variables like the level of income, the educational level, the employment, the Gross Value Added of the region, its density population, the fraction of owners of the land, the purchase power, etc.

Given that the socioeconomic status is an abstract variable, in order to check if there exists indeed a correlation between this status and the geographic distribution of the language usage, we will have to use the geographic distribution of each of these specific indicators. This is the reason why it is important to take into account not every indicator is a good predictor of the socioeconomic status individually (this will be explained in detail later, in the code), and their quality depends totally on the external entities that provide them. Then, the approach will be to try with different indicators and different resolutions and study in which cases there exists a higher correlation, as well as to determine how representative of the reality that correlation is (because a low correlation could mean either that the correlation does not exist indeed, or that the quality of the data or of the analysis is so poor that the correlation is hidden).

---

<sup>2</sup>It is important to mention that in the research we assumed that people sometimes avoid writing the apostrophe for convenience, regardless of whether they use a standard or a non standard form, so there has been included in the analysis the structures with *doesnt* and *dont* despite they are not grammatically correct.

## 2.3 Data Description

This research relies on the information provided by seven Dataframes, containing tweets written between 2015 y 2021, one Dataframe per year<sup>3</sup>, almost 500 million tweets with information about their location, among other things. A great deal of information is provided about each tweet: date and time when it was written, codified information about the user's identity, its location, the text contained in the tweet, etc. For this study, the only relevant information we considered was the *place* where the tweet was written and, obviously, the text contained in the tweet.

Twitter's privacy policy plays a fundamental role in the quality of the information obtained from the *places*. If the user agrees to be geolocated, the place of their tweet is given by the exact coordinates pointing the location of the tweet. Nonetheless, not every user is that confident and some of them deny permission to be spotted. A fraction of users are in a situation in between, they agree to be traced but only partially, and what the Dataset gives in this case are the coordinates of the vertices of a rectangle which contains the tweet. Here the information is more or less relevant depending on the size the rectangle, and there is a wide spectrum of sizes depending on the place. It could be from a rectangle the size of a point which refers to the so called Points of Interest, places like museums, cafeterias, monuments, etc. to a rectangle the size of the whole country, passing through rectangles of different sizes depending on the areas of cities. In this sense, the resolution that could be obtained in the geographic distribution of the language usage will vary enormously depending on the type of the location given for each tweet, and the strategy to follow must take into account which is the adequate resolution to be able to compare the result with the socioeconomic status' indicators.

## 2.4 Code Fundamentals

The two main tools we used to analyze the data were *Pandas* and *Geopandas*. On the one hand, *Pandas* is a Python library specific for big data analysis and working with Dataframes; on the other hand, *Geopandas* is a Python library specific for geolocalized data analysis and depicting results in maps. In a summarized way, the code works as follows:

- First, it loads the Dataframes and selects all the English tweets (using the Twitter's language detector) placed in the United Kingdom (either in Northern Ireland, Scotland, Wales or England).
- Second, to ease the text processing, the program eliminates from the tweets all the irrelevant information for the linguistic analysis (Hashtags, URLs and Usernames). Besides, it eliminates all the unnecessary information of the Datframe, leaving only the pre-processed text and the place where it was written.
- Third, it pre-selects all the expressions with the structure:

$$he/she + (does\ not/doesn't/doesnt/do\ not/don't/dont) + word$$

where the parentheses means that the presence of what is inside is optional. Furthermore, to ease the comparison with the words list, it lowercases all the text.

- Forth, it compares the preliminary list obtained with the list of verbal forms of 98 verbs, obtaining then a definitive list of *standard* and *non standard* expressions with their information about geolocalization.
- The purpose now is to obtain the geographic distribution of these expressions. To do it, the code creates a grid composed by cells<sup>4</sup> and counts the number of times each *standard* or *non standard* expression of the reference list appears in each cell. In the case in which tweets have the exact location (either the exact point or the so-called Points of Interest), the expression will be located without ambiguity in a certain cell. However, for the tweets with an approximated location given by a rectangle, there could be a situation in which the rectangle gets divided in several parts by

---

<sup>3</sup>The 2021 Dataset is not complete.

<sup>4</sup>The size and shape of the cells is arbitrary, and depending on the cells defined the code will obtain a different resolution and/or it will be easier to compare the distribution with the socioeconomic status' indicators. This will be discussed in the following sections.

the grid, with a fraction of its area inside each cell. In this case, we assumed that expressions inside this rectangle will be homogeneously distributed inside the rectangle. Then, the approach to deal with the count will be to distribute the expressions inside the rectangle between cells overlapped with it proportionally to the fraction of area the rectangle has inside each cell.

- It is necessary to make two comments regarding the method explained in the last point. First, if one makes a distribution proportional to some fraction of area, it could happen that the final count inside some cells was different from an integer. That is why once obtained the final result, the code rounds the number to the closest integer. Second, it is important to take into account Earth is spherical and we can only work with bidimensional projections deforming distances, angles and areas, which is a problem if the distribution is based on the area. That is why it is essential to make a conversion to a different reference system which preserves real areas before distributing the expressions. In the project, the system we chose was the *ESRI:102013 - Europe Albers Equal Area* [13], specific for dealing with areas, although the one we used to depict maps was the original one, *EPSG:4326 - Geographic Coordinates*, to ease visualization.
- Finally, in this first phase the code uses the final count obtained to depict in a map the linguistic polarization for each cell (the concept of linguistic polarization will be explained in the next section) in a color scale, so that each cell has a color depending on its polarization. It is worth mentioning that the code computes the polarization only for cells with more than ten coincidences with the reference list. Cells with less coincidences are considered statistically irrelevant.

The code's first phase gives a generic map of the polarization depicting the geographic distribution of the language usage. Now, the second phase's objective is to compare this distribution with the distribution of specific socioeconomic status' indicators.

- First, we select a socioeconomic status' indicator we consider relevant. For instance, in this specific research we used two indicators: the rental price of one-bedroom flats per district in London and the Gross Value Added per Ceremonial County in England. Once selected, the code analyzes the type of geographical division used by the source that provides the information (districts, counties, parishes, etc.).
- Second, the code repeats the first phase transforming the grid in a grid composed by cells that are the actual geographic divisions used by the source for the indicator so as to compare both distributions. For instance, if the first indicator is the rental price per district in London, the grid is composed by cells that are the districts. Here it is clear why the choice of the shape and size of the cells is arbitrary, the most effective approach is to select them depending on the specific indicator being analyzed.
- In this point it is understood why some indicators are better predictors than others individually. Actually, it is due to the fact that the resolution that can be obtained in the first phase, in the language usage distribution, is limited and depends absolutely on the size and shape chosen for the cells<sup>5</sup>. Then, when comparing with the indicator in the second phase, the analysis will not always give a high correlation, since the information which is being obtained from Twitter has a poor quality, regardless whether or not such correlation exists indeed.
- Once we obtain the information about both maps, the code calculates finally the Pearson correlation coefficient between the language polarization and the socioeconomic status' indicator, as well as the p-value, to check if there exists a correlation between the two variables.

#### 2.4.1 Linguistic Variables: Polarization

Finally, we need to define the mentioned variable that allows us to make a quantitative analysis of such thing like the *language usage* of standard and non standard expressions based on the count of expressions inside cells, and visualize its geographic distribution in a map. This variable is the so-called *polarization*  $V_w^c$ , defined for each expression  $w$  y inside each cell  $c$  in an analogous way to the

---

<sup>5</sup>If cells are too small, there will be a lot of them with a little number of tweets and the statistical sample will not be relevant, and if the cells are too big, socioeconomic differences will be homogenized inside each cell (since it will contain both higher status and lower status individuals) and there will be no important differences between cells.

one in [14]:

$$V_w^c = \frac{(NS)_w^c - (S)_w^c}{(NS)_w^c + (S)_w^c} \quad (1)$$

In this definition,  $(NS)_w^c$  refers to the number of times each non standard expression  $w$  is used in the cell  $c$ , and  $(S)_w^c$  refers to the same for the standard expression, so that the polarization equals -1 if only standard expressions are used in the cell and +1 if only non standard expressions are used in the cell. Using this definition, the *average polarization*  $V^c$  is computed taking the mean of the polarizations of every expression that appears in the cell.

$$V^c = \frac{\sum_w V_w^c}{N^c} \quad (2)$$

Where  $N^c$  is the number of different pairs standard - non standard that appear in the cell. From this value it can be computed the global polarization for all the map taking the average of all the polarizations of all the cells. It needs to be mentioned that in every map the polarization is depicted using a color spectrum to ease visualization.

## 2.5 Validity Test

In order to test the code's functioning, a few reference tweets are pre-selected to check if the program is able to process and clean them, isolate the relevant expressions and collect information about the location. Nevertheless, making sure the code works at a large scale, i.e., it does not present errors when aggregating the data based on their location and depicting the maps, is not a trivial task at all. In this project we performed a validity test trying to reproduce the results obtained in [14], in which they carry out a similar analysis to the one here, substituting the *standard - non standard* expressions with *British - American* expressions.

As a brief explanation of the paper, without going deeper into the details because it is not the purpose of this project, they use as well two lists of reference expressions, in this case a first list with 130 *Vocabulary* variants between British and American English, and a second list with 263 *Spelling* variants. Following a similar strategy using a similar code, defining an analogous *polarization* such that -1 corresponds to a purely British polarization and +1 corresponds to a purely American polarization, and choosing a grid with square cells of  $0.25^\circ \times 0.25^\circ$ , the code gave the following geographic distribution:

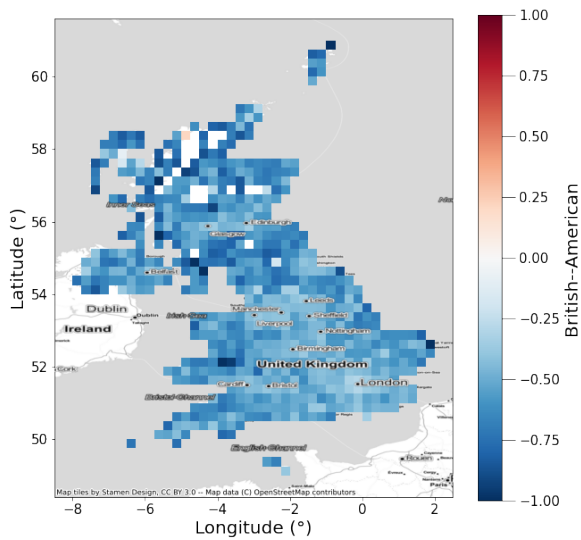


Figure 1: Map of the geographic distribution of the language usage for the *Spelling* variants between British and American English per  $0.25^\circ \times 0.25^\circ$  square cell in the United Kingdom.

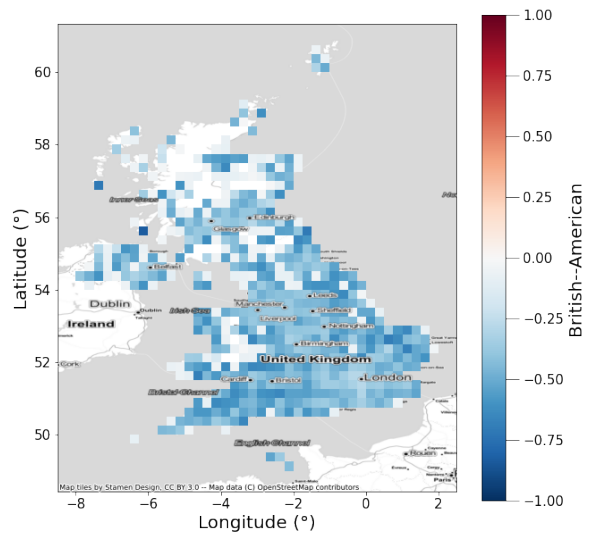


Figure 2: Map of the geographic distribution of the language usage for the *Vocabulary* variants between British and American English per  $0.25^\circ \times 0.25^\circ$  square cell in the United Kingdom.

Analyzing both maps it can be seen that the *Spelling* has a lower polarization (closer to a purely British polarization) than the *Vocabulary*, which could be explained because people learn how to spell in the school, where they learn British rules, while they acquire their vocabulary through films, series or books, things deeply influenced by the American culture. Besides, in both maps larger cities present a higher polarization due to the heterogeneity of the population there. Additionally, for the whole United Kingdom, the average polarization calculated is:

$$V_{Spelling}^c = -0.58 \pm 0.14 \quad (3)$$

$$V_{Vocabulary}^c = -0.37 \pm 0.19 \quad (4)$$

This result is really close to the one provided in the article, and the geographic distribution in the maps shows the expected behavior, so we can conclude that the code works as expected also at a large scale.

### 3 Results and discussion

#### 3.1 Preliminary analysis

To begin with, we conducted a generic analysis about the language usage in order to study the differences between maps with different resolutions of the grid and discuss the statistical relevance of the results. To do it, we defined three different grids covering the whole territory of the United Kingdom, composed by square cells of different sizes:  $0.125^\circ \times 0.125^\circ$ ,  $0.25^\circ \times 0.25^\circ$  y  $0.5^\circ \times 0.5^\circ$  (in the system *EPSG:4326*). The three maps are presented below:

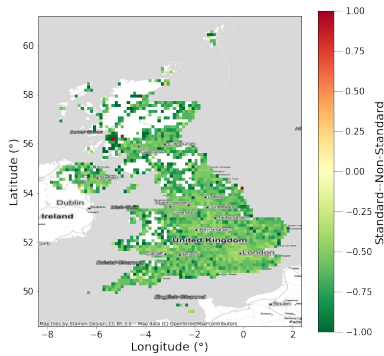


Figure 3: Map of the geographic distribution of the linguistic polarization per  $0.125^\circ \times 0.125^\circ$  square cell in the United Kingdom.

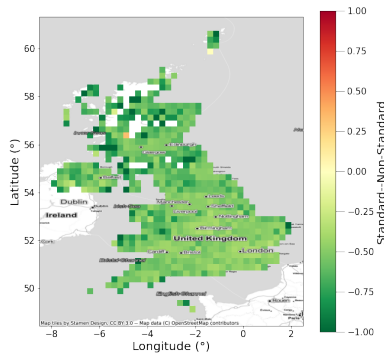


Figure 4: Map of the geographic distribution of the linguistic polarization per  $0.25^\circ \times 0.25^\circ$  square cell in the United Kingdom.

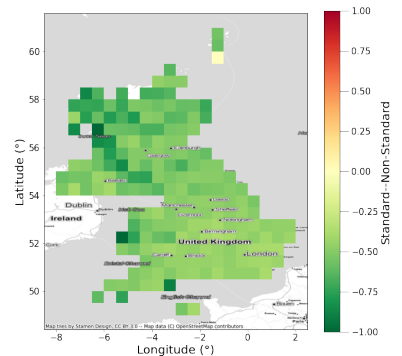


Figure 5: Map of the geographic distribution of the linguistic polarization per  $0.5^\circ \times 0.5^\circ$  square cell in the United Kingdom.

The main conclusion that can be drawn from these three maps is the one mentioned about the importance of the resolution chosen. On the one hand, focusing for example on the region of Scotland, when cells are big almost the whole map is covered by them, whereas when cells are small the region is almost empty, illustrating that due to the small number of tweets in that region a wrong choice of resolution was faking results about a place that was actually empty. It will be discussed later, but just analyzing these three maps it is clear that apart from Edinburgh and Glasgow, almost the whole Scottish statistical sample is poor and cannot be used for the analysis. In general, the wrong resolution could lead to wrong results for certain regions if cells are too big and cover regions where there are no tweets at all together with regions with a lot of tweets. On the other hand, as mentioned, when cells are big the map is quite homogeneous since differences are homogenized inside each cell. Nonetheless, when cells become smaller, local differences start to appear in some regions. This is why it is important to choose the correct resolution if we want to find a latter correlation with some indicator.

These conclusions are confirmed if we perform a deeper statistical study. We show below three more maps depicting the number of tweets containing expressions from the reference list per cell, the number of unique expressions of the reference list per cell, and the standard deviation of the polarization per cell:

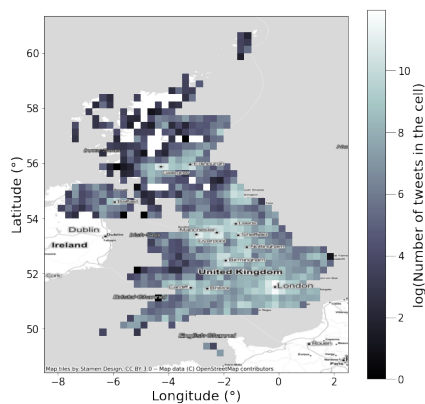


Figure 6: Map depicting in a color scale the natural logarithm of the number of tweets containing expressions from the reference list per  $0.25^\circ \times 0.25^\circ$  square cell in the United Kingdom.

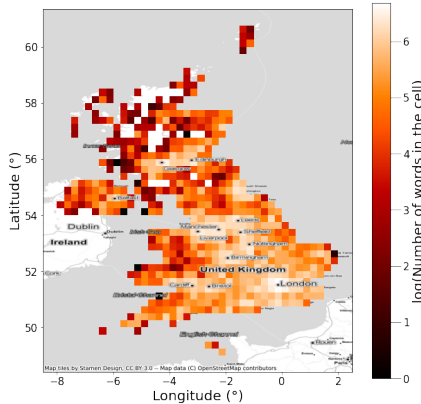


Figure 7: Map depicting in a color scale the natural logarithm of the number of unique expressions of the reference list per  $0.25^\circ \times 0.25^\circ$  square cell in the United Kingdom.

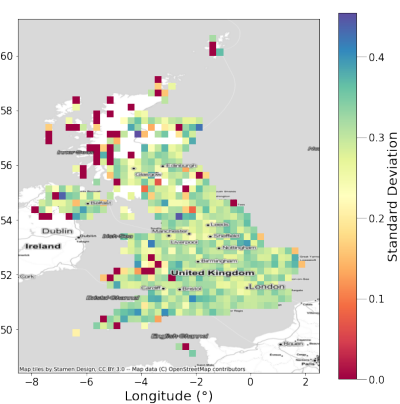


Figure 8: Map depicting in a color scale the standard deviation of the polarization per  $0.25^\circ \times 0.25^\circ$  square cell in the United Kingdom.

Focusing first in the previous example, now it is clear why the Scottish statistic sample is poor: except for regions around Edinburgh and Glasgow (biggest cities), in the rest of Scotland both the number of tweets per cell and the number of unique expressions from the standard list is too low. Furthermore, the map depicting the standard deviation shows a mistake in some cells of the region: red cells show standard deviation 0, and this is because this standard deviation is computed with just one expression of the reference list (which implies the polarization computed with just one value, and no standard deviation). By and large, these three maps show that the most statistically relevant regions to study are the biggest cities in a smaller resolution and the territory of England in a bigger resolution. This is the reason why the following and future analysis will be focused in these specific parts of the country.

### 3.2 Gender usage

When studying the geographic distribution of the language usage, we discovered that there exists a significant difference between the number of expressions of the reference list with subject *he* used and the number of expressions of the reference list with subject *she*. This discovery motivated a further research, and we found that expressions containing *he/his/him* entail around 71% of the expressions, whereas expressions containing *she/her/hers* entail around 29% of the expressions. Comparing with the last analysis conducted in January 2021 [15], the proportion of masculine users is 68.5% while the feminine one is 31.5%.

On the other hand, a second study was performed to check if the usage of the so-called *neutral gender*<sup>6</sup> has grown through the years. Below it is shown a temporal series depicting a variable defined as *neutral-gender usage*, which consists of the number of times words like *they/them/their/theirs* appear per year divided by the number of tweets written per year.

<sup>6</sup>Gender used to refer to people who either did not specify their gender, it is unknown or they prefer to be considered like that.

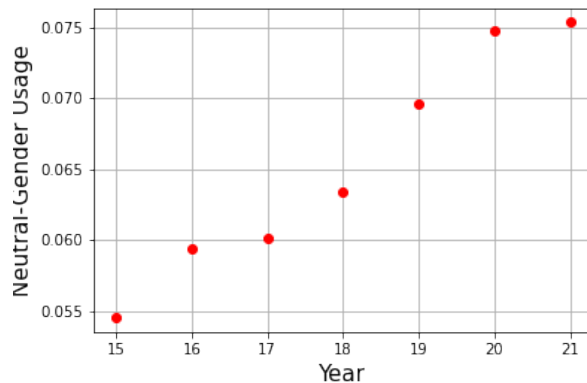


Figure 9: Evolution between 2015 and 2021 of the variable defined as *neutral-gender usage*. The errorbars are depicted but they are so small they fit inside the points.

Undoubtedly, its usage has grown since 2015. Nonetheless, as shown in papers like [10], it is really difficult to draw conclusions about gender and gender usage from data provided by social media, it is not as simple as considering masculine, feminine and neutral markers. A whole new project should be made in order to interpret and improve the previous results, so this analysis will not go deeper in this topic.

### 3.3 GVA per ceremonial county in England

In the first analysis comparing the geographic distribution of the linguistic polarization with the socioeconomic status, the indicator we chose was the Gross Value Added (GVA), which is defined as [16] an economic productivity metric that measures the contribution of a corporate subsidiary, company, or municipality to an economy, producer, sector, or region. The GVA provides a dollar value for the amount of goods and services that have been produced in a country, minus the cost of all inputs and raw materials that are directly attributable to that production. We expect it to correlate with the geographical distribution of the language usage because in places with a higher GVA, education tends to be more accessible for a bigger fraction of the population, so that they are expected to use standard expressions.

Nonetheless, as mentioned before, this is strongly conditioned by the resolution of the grid used and this is what we are testing in this part of the project. In this case, the data used consists of the GVA per Ceremonial County<sup>7</sup> in England. It is important to mention that the quality of the data used in this case is poor because it is not updated regularly with detail by the Office for National Statistics (ONS) of the United Kingdom, the institution in charge.

All things considered, on the one hand, we repeated the geographic distribution analysis using as grid the one in which the cells are the British Ceremonial Counties, so as to compare with the GVA data provided by the ONS. On the other hand, in another map we illustrated the GVA per Ceremonial County using colors, in an analogous way to the linguistic polarization, to be able to compare both maps visually as well as using the Pearson correlation coefficient. We present both maps below, along with the Pearson correlation coefficient and the p-value.

<sup>7</sup>Ceremonial Counties are a British administrative division.

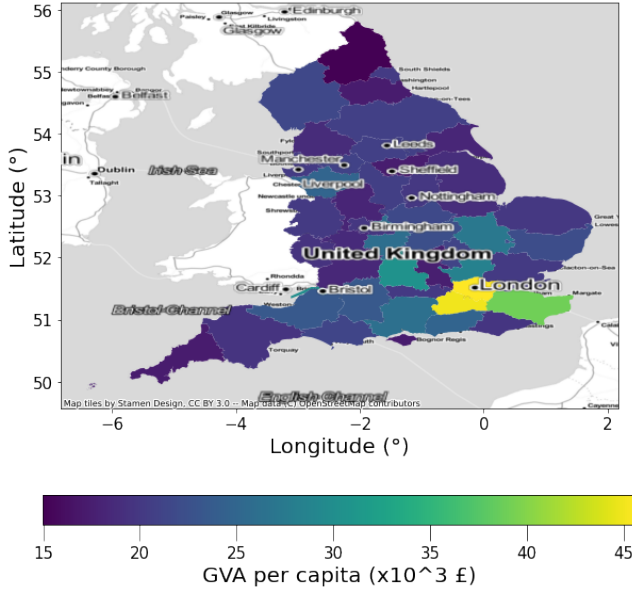


Figure 10: Map of the geographic distribution of the Gross Value Added in pounds per Ceremonial County in England.

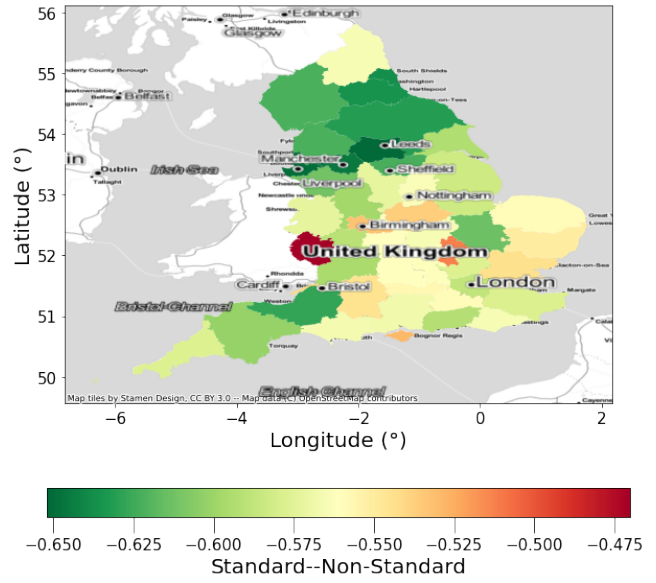


Figure 11: Map of the geographic distribution of the language usage per Ceremonial County in England.

$$R = 0.070 ; p = 0.642 \quad (5)$$

Both maps do not show visually a similar behavior at all, and a Pearson correlation coefficient close to zero, as well as a high p-value obtained confirm that. Several explanations could account for this result. First, last time GVA data was updated by the ONS was in 2013, whereas data used from Twitter covers between 2015 and 2021. Despite the fact that the data compared are from different periods, it is expected that in a country like the United Kingdom, the GVA maintains a more or less similar behavior in a period of time that short between Ceremonial Counties. Nonetheless, this is just an assumption which could be perfectly wrong. Besides, as previously mentioned, the resolution of the grid plays a fundamental role in the quality of the results obtained. On the one hand, it could happen that the Ceremonial County was an administrative division big enough to homogenize socioeconomic differences between its inhabitants, i. e., it is possible that there exist indeed differences in the language usage inside each County, not observed in average because ones balance others, and when comparing between Ceremonial Counties no correlation is observed at all, even if that correlation exists at a different scale. On the other hand, not all Ceremonial Counties share the same population density or the same proportion of Twitter users, so it is possible that these results are more representative in some Counties than others.

For all these reasons, it is crucial first to repeat the analysis when the ONS updates the data, and second to conduct a more exhaustive statistical research from these preliminary results to determine their scope, reliability and representativeness.

### 3.4 Rental price of one-bedroom flats per districts in London

Due to the results obtained for the GVA per Ceremonial County, we decided to repeat the analysis changing the resolution of the grid to a smaller scale, making more difficult to socioeconomic and linguistic differences to homogenize inside each cell. This is why the new cells chosen were districts, specifically the socioeconomic status' indicator chosen was the rental price of one-bedroom flats per district in London, data provided by the London Assembly. We chose this indicator because rental prices vary depending on the purchase power of the inhabitants of the region, which is directly related with access to education and therefore, their usage of a *standard* or a *non standard* English, and one-bedroom flats were chosen because they are the most commonly rented flats.

Again, as in the previous case, we repeated the language usage’s geographic distribution with a new grid in which the cells were the London districts, and we obtained another map depicting the rental price of the flats using a color scale. Besides, we computed the Pearson correlation coefficient and the p-value between the polarization and the rental price. We present the results obtained below:

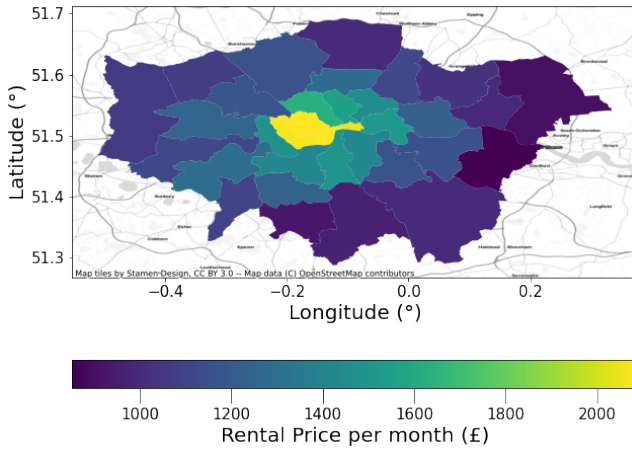


Figure 12: Map of the geographic distribution of the rental price of one-bedroom flats in pounds per district in London.

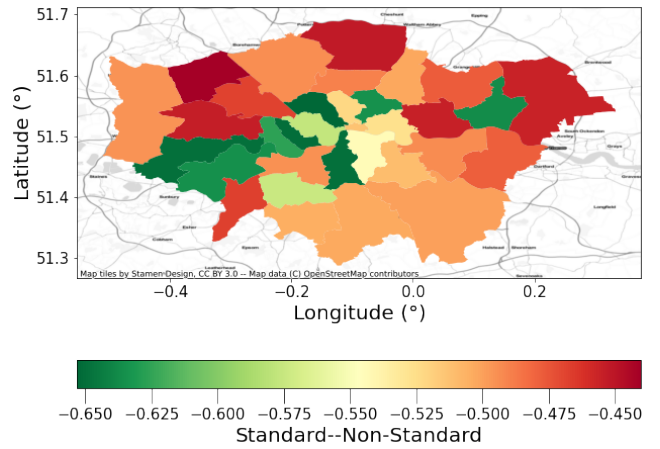


Figure 13: Map of the geographic distribution of the language usage per district in London.

$$R = -0.474 \quad ; \quad p = 0.005 \quad (6)$$

As we can see, now both maps do present a similar behavior in some regions compared to the previous case, specially between center-south-west districts and the surroundings, something confirmed by the Pearson correlation coefficient. The p-value shows that the result is statistically significant, and although the Pearson coefficient is not high enough to consider there is a clear correlation<sup>8</sup>, its value is much higher than the previous case<sup>9</sup>. This result could confirm the hypothesis about the importance of the resolution chosen, as well as the one about the quality of the socioeconomic data and the analysis (now the rental prices are updated and London has a rich statistical sample, big enough, with the highest number of tweets in the whole country).

## 4 Conclusions

To begin with, specifically about the project, it is important to highlight this is just a preliminary analysis with the purpose of serving as a basis for a deeper research in the future, which gives a basic notion about the main features that must be taken into account when elaborating a study in this topic.

For instance, the statistical study we presented along with the correlation analysis of the two socioeconomic status’ indicators and the comparison between different resolutions chosen for the grid have illustrated first, that the most statistically relevant regions are big cities at a small scale and the region of center-south-east England at a large scale, and second, that the resolution chosen for the grid is crucial to be able to observe linguistic differences, avoiding homogenization between close regions inside big cells or drawing false conclusions about empty regions. Both things considered, we must conduct a further research comparing different resolutions for the grid (districts or parishes) between big cities, inside them or at a large scale, focused on the mentioned region of England, and for that it is important to chose adequate socioeconomic status’ indicators, not only with the preferred administrative divisions, but updated from official sources. Also, it would be interesting to analyze, once established the optimal resolution of the grid, which indicators are better predictors of the linguistic variations. This investigation shows as a promising starting point a positive correlation

<sup>8</sup>Its absolute value should be equal or bigger than 0.7

<sup>9</sup>Besides, its value is negative, which is something expected since the higher the rental price is, the lower the polarization should be, because a lower polarization implies a more *standard* language usage.

between the rental price in London and the language usage when the grid is composed by districts. Apart from that, the study could be improved by adding more *standard* and *non standard* variants to the reference list, in order to widen the statistical sample, and by correcting details that could be blurring the correlation between the polarization and the indicators, like the presence of tweets written by non residents in the Dataframe.

As a collateral conclusion, a whole new study could arise from the results obtained about the gender usage, taking into account the necessary precautions mentioned in articles like [10], which offer a guide about how to treat gender in computer sociolinguistic studies like this one. Related to this, it is important to remember that the results given by this and further analysis must be understood along with the papers and meta-analysis mentioned in the introduction about the limitations present when using data provided by social media for a study of sociolinguistic nature, being aware of the intrinsic bias and problems, to comprehend their representativeness and their scope.

All in all, it need not be said what a revolution in Sociolinguistics has entailed the branch of computer social science, allowing a cross-disciplinary approach to the problem, widening possible outcomes in such complex disciplines like *gender* or *socioeconomic status*, so as to gain insight into the origin and nature of socioeconomic differences and deal with inequalities within our society.

## Acknowledgments

I would like to thank my supervisors, David Sánchez and José J. Ramasco, for their guidance and support during the project. As well, I would like to acknowledge Thomas Louf, for his patience during my sessions of infinite basic questions. Thanks to professor Lucía Loureiro-Porto, from the department of Spanish Philology, Modern and Classic, of the University of the Balearic Islands, for the list of words used in the analysis. This work was supported by the SURF@IFISC 2021 fellowship.

## References

- [1] Charles Boberg, John Nerbonne, Dominic Watt, *The Handbook of Dialectology*, Wiley-Blackwell (2018)
- [2] Katherine D. Kinzler, Emmanuel Dupoux, Elizabeth S. Spelke. *The native language of social cognition*. Proceedings of the National Academy of Sciences **104**, 12577 (2007)
- [3] Jack K. Chambers, *Sociolinguistic theory: linguistic variation and its social significance*, Wiley-Blackwell, Cambridge (1995)
- [4] Kathryn Campbell-Kibler, *New directions in sociolinguistic cognition*, University of Pennsylvania Working Papers in Linguistics **15**, 31 (2010).
- [5] Jacob Levy Abitbol, Márton Karsai, Jean-Philippe Magué, Jean-Pierre Chevrot, Eric Fleury, *Socioeconomic Dependencies of Linguistic Patterns in Twitter: A Multivariate Analysis\**, Proceedings of the 2018 World Wide Web Conference, 1125 (2018).
- [6] Bruno Gonçalves, David Sánchez, *Crowdsourcing Dialect Characterization through Twitter*, PLoS one, 9(11):e112074 (2014).
- [7] Jacob Levy Abitbol, Márton Karsai, Eric Fleury, *Location, Occupation, and Semantics based Socioeconomic Status Inference on Twitter*, 2018 IEEE 18th International Conference on Data Mining - IWSC'18 2nd International Workshop on Social Computing, (2018).
- [8] Gonzalo Donoso, David Sánchez *Dialectometric analysis of language variation in Twitter* In Proceedings of the Fourth Workshop on NLP for Similar Languages, Varieties and Dialects, 16 (2017)
- [9] Umashanthi Pavalanathan, Jacob Eisenstein *Confounds and Consequences in Geotagged Twitter Data*. EMNLP, (2015)
- [10] David Bamman, Jacob Eisenstein, Tyler Schnoebelen *Gender identity and lexical variation in social media*. Journal of Sociolinguistics **18**, 135 (2014)
- [11] Vivek Kulkarni, Bryan Perozzi, Steven Skiena, *Freshman or Fresher? Quantifying the Geographic Variation of Language in Online Social Media.*, In ICWSM, (2016)
- [12] Dhouha Ghazouani, Luigi Lancieri, Habib Ounelli, Chaker Jebari, *Assessing Socioeconomic Status of Twitter Users: A Survey.*, Proceedings of Recent Advances in Natural Language Processing, 388 (2020)
- [13] <https://epsg.io/>
- [14] Bruno Gonçalves, Lucía Loureiro-Porto, José J. Ramasco, David Sánchez, *Mapping the Americanization of English in space and time* PLOS ONE **13**, (2018)
- [15] <https://es.statista.com/estadisticas/1203008/porcentaje-de-usuarios-de-twitter-por-genero/>
- [16] <https://www.investopedia.com/terms/g/gross-value-added.asp>

## A Appendix: List of Verbs

Here we present the list of the 98 verbs used for the analysis:

get	go	take	happen	make	see	say	come	give	work
tell	try	talk	find	change	win	ask	start	continue	help
look	keep	play	show	kill	pay	lose	bring	stay	use
stop	turn	hear	want	call	move	vote	live	spend	meet
become	miss	cut	buy	send	feel	fight	hold	know	eat
break	throw	stand	pick	write	like	pass	think	fall	build
walk	learn	save	create	raise	solve	lead	add	love	believe
sell	sleep	provide	cause	afford	imagine	understand	handle	expect	remember
reach	produce	serve	offer	begin	watch	choose	drink	survive	control
grow	tweet	forget	enjoy	catch	mean	speak	trust		

# The role of dissipation in Quantum Reservoir Computing

Dimitrios Chalkiadakis, Rodrigo Martínez, Roberta Zambrini, Gian Luca Giorgi  
 Instituto de Física Interdisciplinar y Sistemas Complejos, IFISC (CSIC-UIB)  
 Campus Universitat de les Illes Balears, E-07122 Palma de Mallorca, Spain

## Abstract

We investigate the use of a transverse Ising field model with dissipation, described by the lowering Pauli operator, as the reservoir layer for quantum reservoir computing purposes. We show that this system exhibits the basic properties of convergence and separability which are required in reservoir computing. Finally, we present some results about its performance on a simple linear task.

## 1 Introduction

Reservoir computing (RC) is a brain inspired machine learning technique which is used for real-time computing[1]. A typical RC algorithm consists of three layers. The first one is responsible for injecting the input into the system, therefore it is called the input layer. The next layer, which is called the reservoir, contains nodes which are connected recursively and, therefore, are able to “remember” the input history. The reservoir should also transform non linearly the input and hold the two following properties:

- Fading memory: The initial conditions of the reservoir should not affect the overall performance of the algorithm, thus the reservoir needs to forget its long-past states.
- Separability of different output: The reservoir should be able to respond differently to different inputs.

Lastly, in the output, or readout, layer some quantities  $X_i$  which are measured from the reservoir are multiplied with a matrix of coefficients  $\mathbf{W}$  in order to produce the final output  $Y_{out}$ , like in Fig. 1. During training we vary  $\mathbf{W}$  using linear regression in order to match  $Y_{out}$  and the teacher or target signal  $\bar{Y}$ , while the rest of the reservoir’s parameters are kept fixed.

The aforementioned training procedure combines low training costs and fast learning in contrast to other learning algorithms like back-propagation. We can achieve even more energy and time efficiency if a physical system is used as the reservoir instead of some “virtual” system simulated by a computer[3]. Using this unconventional computing paradigm, we exploit the natural non linear dynamics of the physical system while avoiding the losses which are inherited to every von Neumann architecture. Quantum reservoir computing (QRC) goes a step further by using a

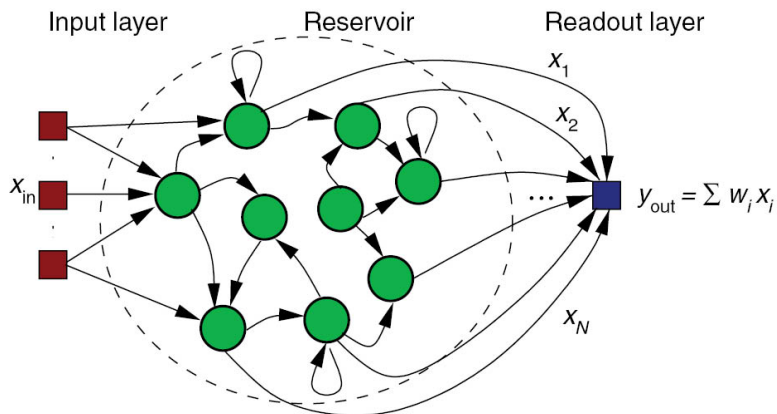


Figure 1: A typical reservoir computing architecture. Taken from [2].

quantum system as the reservoir[4]. The fact that the degrees of freedom of a quantum system increase exponentially with its size indicates that such reservoirs will need less nodes in order to outperform their competitors.

## 2 Theoretical model

In previous works it has been demonstrated that a closed transverse-field Ising system contains rich dynamics which can enhance its performance as a reservoir[5]. The system consists of  $N$  spins which are coupled together and forced by some externally applied magnetic field  $B$ . The Hamiltonian is provided by:

$$H_{ising} = \sum_{i,j}^N J_{ij} \sigma_i^x \sigma_j^x + B \sum \sigma_i^z, \quad (1)$$

where  $J_{ij}$  is the coupling between the  $i$ -th and the  $j$ -th spin ( $J_{ii} = 0$ ) and is randomly drawn from the uniform distribution  $[-\frac{1}{2}, \frac{1}{2}]$  and  $\sigma_i^a$  ( $a = x, y, z$ ) are the Pauli matrices. Let us assume that the input we want to analyze is the sequence  $s = \{s_0, s_1, \dots, s_k, \dots\}$  where  $s_k$  is randomly chosen between  $\{1, 2\}$ . In previous works the injection protocol was to override the state of some spin according to the input[4, 5]. More specifically, at each time  $t = k dT$ , where  $k = 1, 2, 3, \dots$  the wavefunction of the spin was replaced with:  $|\psi_k\rangle = \sqrt{1-s_k}|0\rangle + \sqrt{s_k}|1\rangle$ . Thus, the  $dT$  parameter shows the amount of time that the system is evolved until the injection of the next input. In this project, however, we chose a more experimentally realistic protocol where the input is injected through the magnetic field, according to:

$$B = hs(s(t) + 2), \quad (2)$$

where  $hs$  is the scale of the magnetic field and  $s(t) = s_k$  for  $dT(k-1) < t < dTk$ . When the system is closed, that is when it does not interact with the environment, its time evolution is given by the Schrodinger equation:

$$\frac{d|\psi(t)\rangle}{dt} = -i\hbar H_{ising} |\psi(0)\rangle \implies |\psi(t)\rangle = e^{-iH_{ising}t} |\psi(0)\rangle. \quad (3)$$

When a quantum system is in a mixed state, or ensemble, of pure states, described by the probability  $p_i$  of being on the pure state  $|\psi_i\rangle$ , we define the density operator as:

$$\rho = \sum_i p_i |\psi_i\rangle \langle \psi_i|, \quad (4)$$

which contains all the information about the system. The evolution of the density matrix in the aforementioned Ising system is given by combining Eqs. 3-4 as:

$$\dot{\rho} = -i[H_{ising}, \rho]. \quad (5)$$

The system we considered in this project is an open quantum system as there are interactions with the environment. More specifically, the dissipation of each individual spin is described by the ‘‘jump’’ operator  $\sigma_i^- = \sigma_i^x - i\sigma_i^y$  which forces a spin looking upwards ( $|1\rangle$ ) to fall in the ground state ( $|0\rangle$ ) with the emission of a photon. Then, the evolution of the density matrix follows[6]:

$$\dot{\rho}(t) = -i[H_{ising}, \rho] + \gamma^2 (\sigma^- \rho \sigma^+ - \frac{1}{2} \{\sigma^+ \sigma^-, \rho\}), \quad (6)$$

where  $\gamma$  is the dissipation strength. Finally, any observables of the system could be used as the aforementioned quantities  $X_i$ . In our case, we used the projections of each spin over the ‘‘z’’ axis  $\langle \sigma_i^z \rangle$ .

## 3 Results and discussion

### 3.1 No input injection

The simplest case of a system which evolves under no input injection was firstly examined. Therefore, the external field was always constant and equal to  $B = hs$ . All simulations ran in Python[7], while we used functions from the QuTip library for the numerical integration of Eqs. 6. Each simulation needed a considerable amount of time so we could not search the parameter space with high

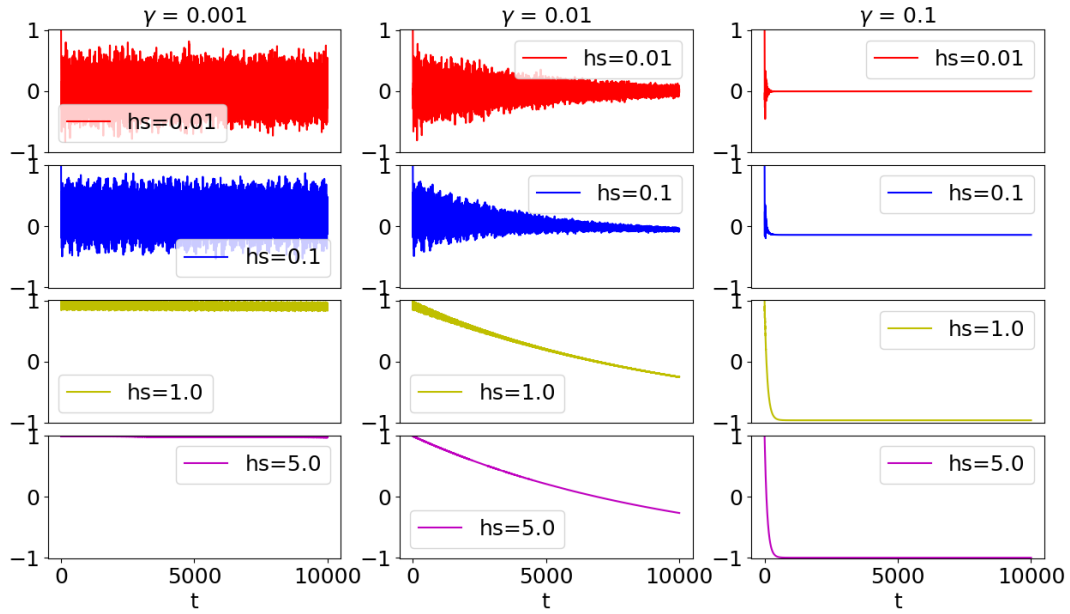


Figure 2: Evolution of the expectation value  $\langle \sigma^z \rangle$  of the first spin for different values of  $(\gamma, hs)$ . All spins were initialised in the  $|1\rangle$  direction.

resolution. As a result we investigated the grid  $(\gamma, hs) = (\{0.001, 0.01, 0.1\}, \{0.01, 0.1, 1.0, 5.0\})$ . The parameter  $dT$  is undefined here as there is no injection. Figure 2 shows that the behaviour of the expectation values of the system change dramatically for different parameter values. More specifically:

- For  $\gamma \rightarrow 0$  dissipation becomes negligible as shown in the first column of Fig. 2. On the contrary, the middle and right columns show that greater dissipation forces the system to relax at some fixed point.
- On the other hand, the parameter  $hs$  determines the strength of the magnetic field with respect to the coupling between the spins. For  $hs \rightarrow 0$  the magnetic field becomes negligible which explains the highly oscillatory behaviour on the first two rows of the first column. Note that the spins converge to different fixed points for  $hs = 0.01, 0.1$  and for  $hs = 1.0, 5.0$ . That implies that in the interval  $0.1 \leq hs \leq 1.0$  there is a phase transition, which agrees with previous works[5].

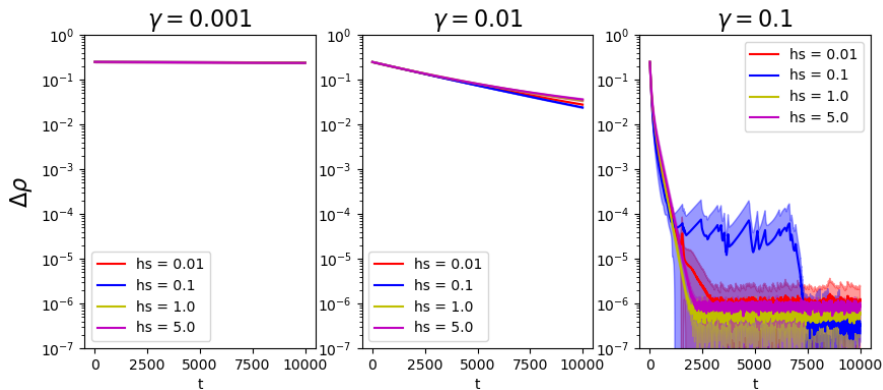


Figure 3: Convergence of two different random initial conditions. The Frobenius norm of the difference of the density matrices decreases with different rates as  $\gamma$  increases. The opaque lines depict the average, while the transparent ones depict the standard deviation, over four different realizations. The asymmetry on the deviation for  $\gamma = 0.1$  is because  $y$  axis is in logarithmic scale.

The next step was to inspect whether this system converges or not. For this reason we evolved two different random initial conditions and stored at each timestep the Frobenius norm of the difference between their density matrices. The above procedure was repeated three more times using different random couplings and random initial conditions. Figure 3 depicts the average convergence over all different initialisation.

Note that for  $\gamma = 0.1$  and  $hs = 0.1$  convergence follows a strange path where it firstly stays in a plateau for a while and then it falls to a lower one. This is due to the dependence of the convergence on the initial conditions and random couplings. Out of the four different realization we used, the three of them converged normally without any second plateau. Nonetheless, in the fourth random realisation, the convergence decreased with two jumps as seen in the figure, affecting the overall average value. The origin of this behaviour is unknown to us at this moment. More random realisations should be simulated if we want to extract safer results.

### 3.2 Input injection

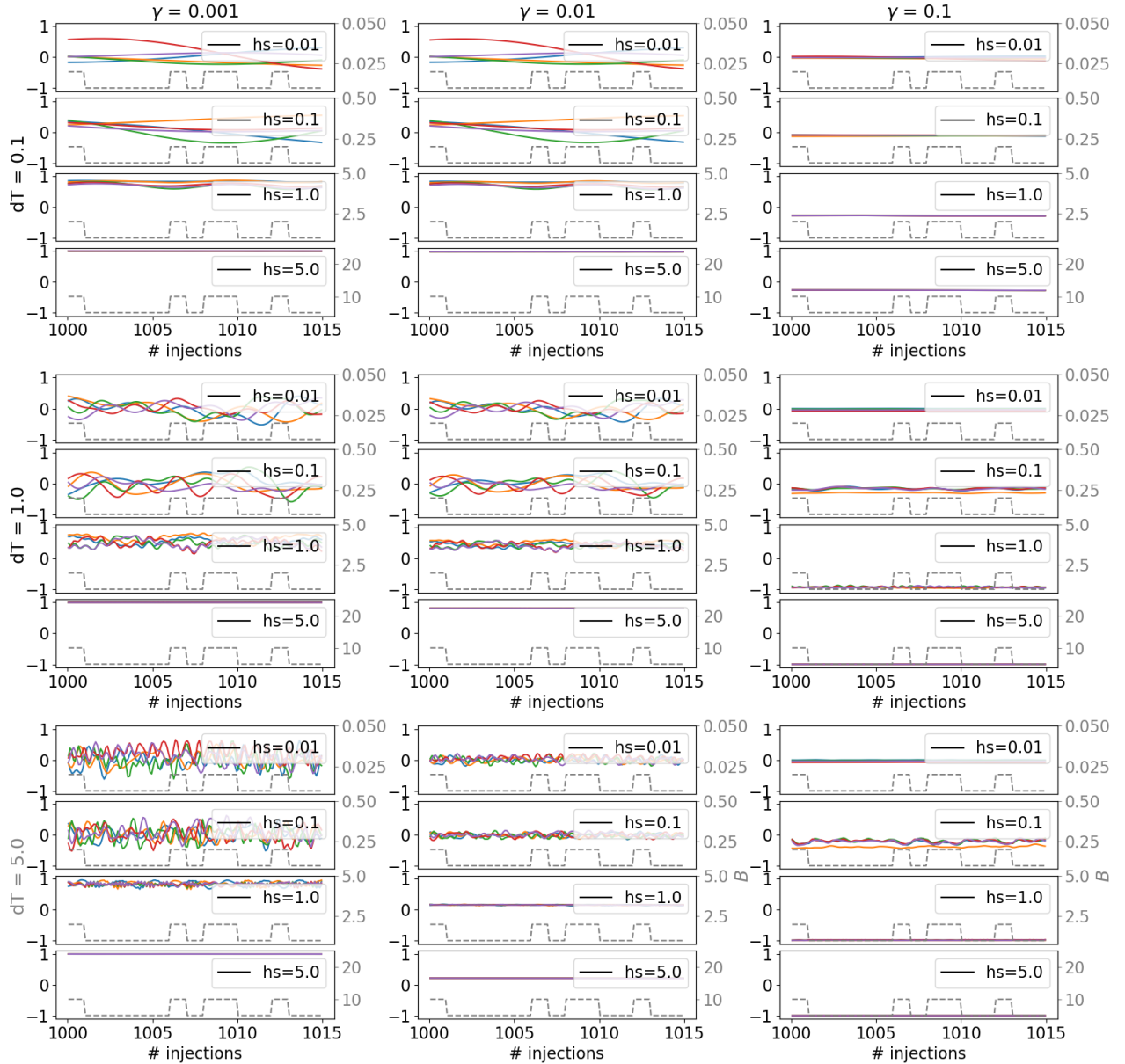


Figure 4: All five observation values  $\langle \sigma_i^z \rangle$  for different values of  $(\gamma, hs, dT)$  depicted as solid lines for a single realization. The externally applied magnetic field  $B$  is depicted as a dashed grey line. Initial conditions as in Fig. 2. The system is visualised between the 1000th and the 1015th injection.

Afterwards, we examined how the input injection affects the dynamics of the system. The

externally applied magnetic field is  $B_k = hs(s_k + 2)$  where  $s_k \in \{0, 1\}$  as mentioned earlier. We remind that the parameter  $dT$  shows for how long we apply  $B_k$  until we introduce the next input  $B_{k+1}$  to the system. Figure 4 visualises the dynamics of all spins in the z-direction along with the applied input. To our understanding there is no clear correlation between the input and the response. Note also that increasing  $dT$  increases the timescale of the simulations, which explains why the third row has more pronounced oscillations than the first one.

In order to understand whether the system truly responds to the variation of the magnetic field or not, we investigated the input separability. For this reason we constructed two identical Ising systems in which we injected two different input sequences  $s_a$  and  $s_b$  respectively. In Fig. 5 we depict the quantity  $\Delta\sigma_{\vec{1}}^z = \sigma_{\vec{1},a}^z - \sigma_{\vec{1},b}^z$  which takes low absolute values for small separability and high otherwise. Note that for the lowest and the highest magnetic scaling values,  $hs = 0.01$  and  $hs = 5.0$  respectively, the differences tend to be lower than those for the middle ones, that is for  $hs = 0.1$  and  $hs = 1.0$ . This is explained for low  $hs$  because the input is negligible with respect to the coupling. On the other hand, when the scaling factor is high the dynamics are saturated and the temporal variation between  $2hs$  and  $3hs$  does not affect them. This is already visualised in the plots where  $hs = 5.0$  of Fig. 4.

### 3.3 Performance

Finally, we wanted to test the performance of a system whose reservoir is the aforementioned Ising spin network. In order to do that we firstly decreased the space of the parameters we were investigating. Figure 3 shows that  $\gamma = 0.001$  should not be used due to low convergence. On the other hand,  $hs = 5.0$  should also be avoided because there is no input separability, as shown in Fig. 5. We also fixed  $dT = 1.0$ .

The task which was chosen was the linear temporal task with delay  $\tau$ . In this benchmark problem the output of the system at timestep  $k$  ( $y_k$ ) must be equal to the input at timestep  $k - \tau$  ( $s_{k-\tau}$ ). In this project we fixed  $\tau = 1$  because the performance falls rapidly for greater delays. For the training process we need to choose the number of ‘‘washing’’ steps which are performed  $N_{wash}$ , that is the number of input we need to inject into the system so that it forgets its initial conditions. During washing we do not store any observables because the system is not ready yet for training. Afterwards, we also need to pick the number of training data ( $N_{train}$ ). The output layer reads the projections  $\sigma_i^z, \sigma_i^x, \sigma_i^y, \forall i$ . Thus, the output of the reservoir consist of a 2D matrix  $\mathbf{X}$  of ( $N_{train}, 15$ ) dimensions. As mentioned above, the output of the system is provided by the linear transformation  $\vec{y} = \mathbf{X}\vec{W}$ , where the vector  $\vec{W}$  is calculated using the linear regression method.

After training we evaluate the performance of the system on the same training set using the metric:

$$C = \frac{cov^2(y, \vec{y})}{\sigma^2(y)\sigma^2(\vec{y})}, \quad (7)$$

which is bounded in the interval  $[0, 1]$  with 0 meaning that the output and the target are not linearly correlated at all, while 1 means that they are completely correlated.

In Fig. 6 we depict the performance of the system for all the aforementioned parameter values. Note that the correlation squared metric remains relative low for all values of  $(\gamma, hs)$  except for  $\gamma = hs = 0.1$  suggesting that there is some phase transition which enhances the capabilities of the system. On top of that, it seems that the overall performance is affected by the interplay between separability and convergence. This is demonstrated by the fact that the performance is unexpectedly better for relatively low values of separability (shown in Fig. 5), that is for  $\gamma = 0.1$ , probably because in this regime the convergence is higher (shown in Fig. 3).

Furthermore, the fact that the performance does not change dramatically with respect to  $N_{train}$ , except for the first column ( $N_{train} = 50$ ), indicates that there is no overfitting. On the other hand, the system performs better for  $N_{wash} > 200$ , which was expected because greater  $N_{wash}$  implies that the system ‘‘remembers’’ less about the initial conditions.

## 4 Conclusions

In this project we conducted a preliminary investigation on the role of dissipation on QRC while we also used a different input injection than in previous works by encoding the input sequence on the externally applied magnetic field. Therefore, the system we studied is more realistic than the models which are usually used in QRC.

We showed that this reservoir holds the basic properties of separability and convergence while it performs relatively well in a linear task which requires memory, for specific parameter values.

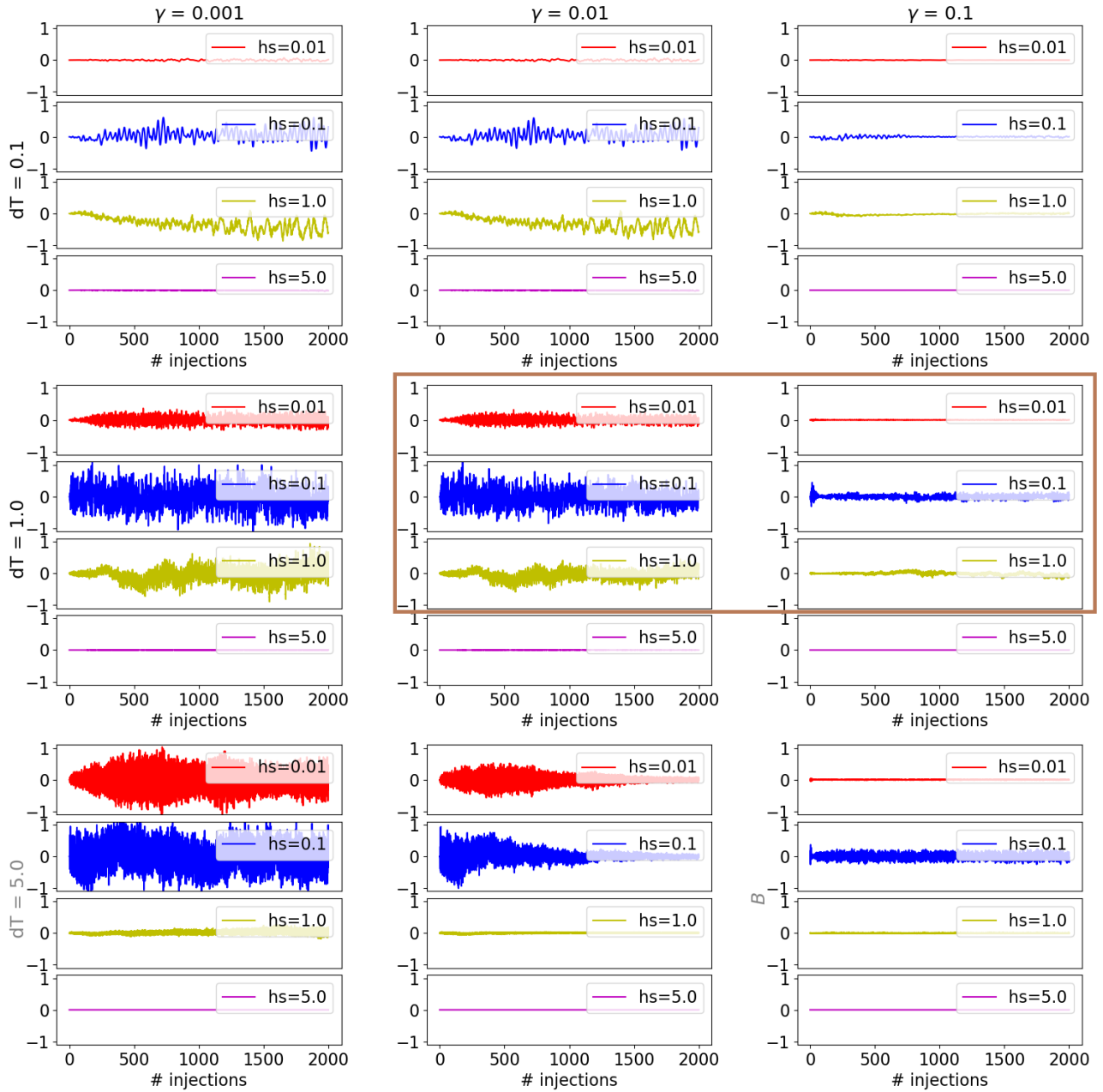


Figure 5: Separability of the system for different parameter values. In the plots we depict the quantity  $\Delta\sigma_1^z$  for two different input signals. Initial conditions as in Fig. 2. The brown box indicate the subparameter space which is used in Fig. 6.

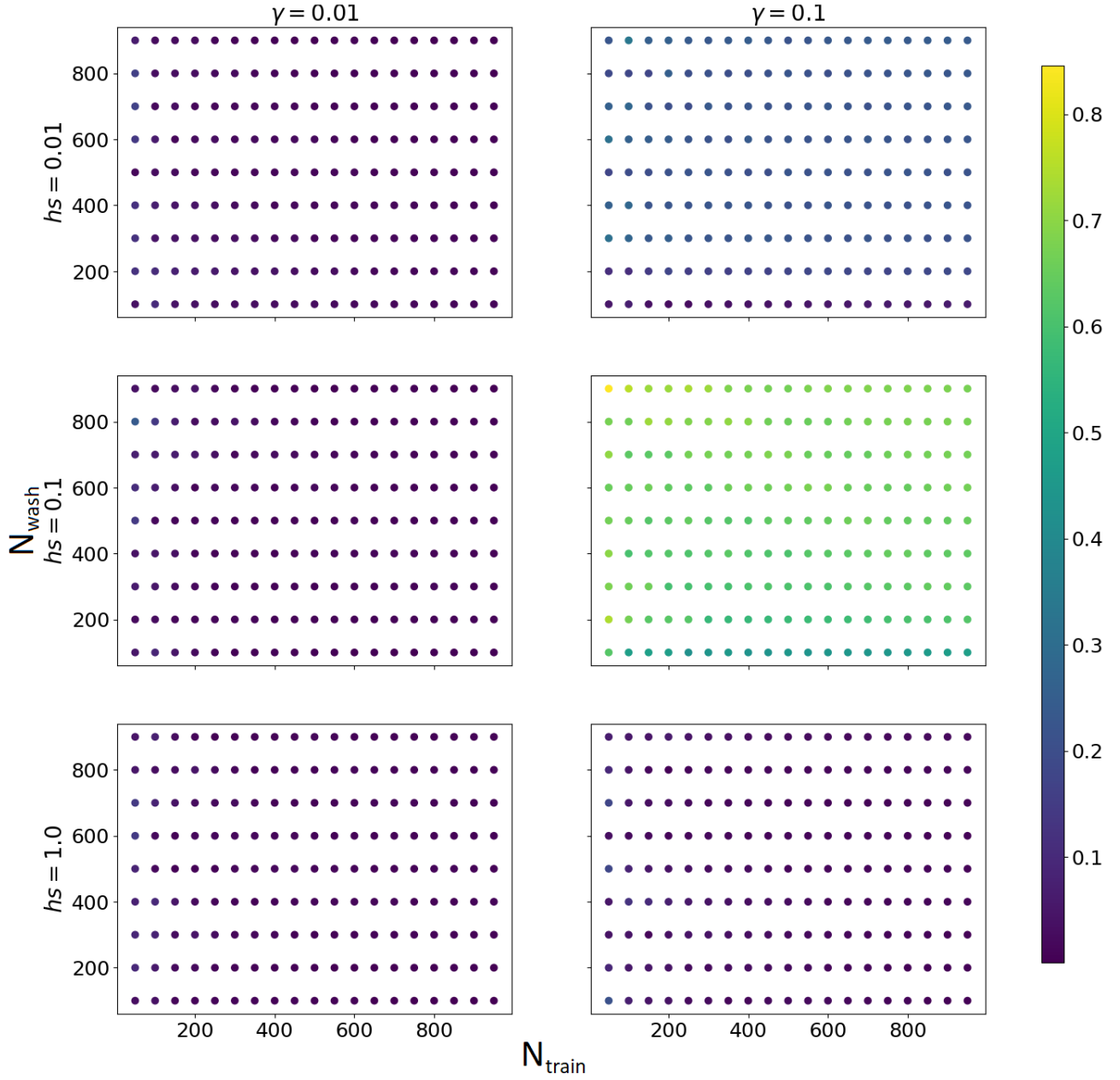


Figure 6: Performance of the QRC system for different number of washing and training data. Other varied parameters:  $hs, \gamma$ . Fixed parameters:  $dT = 1.0, \tau = 1$ . Initial conditions as in Fig. 2.

More research should be conducted in order to link the underlying dynamics of the reservoir with its performance. In this way, the computational abilities of the model will be enhanced and more realistic non-linear problems could be solved.

Finally, in a more broader perspective, different models of dissipation and different ways of input injection should be exploited in order to find the most realistic and yet efficient in terms of performance, reservoir.

## **Acknowledgments**

This work was supported by the SURF@IFISC fellowship.

## References

- [1] Mantas Lukoševičius and Herbert Jaeger. “Reservoir computing approaches to recurrent neural network training”. In: *Computer Science Review* 3.3 (2009), pp. 127–149. ISSN: 1574-0137. DOI: <https://doi.org/10.1016/j.cosrev.2009.03.005>. URL: <https://www.sciencedirect.com/science/article/pii/S1574013709000173>.
- [2] Guy Van der Sande, Daniel Brunner, and Miguel C. Soriano. “Advances in photonic reservoir computing”. In: *Nanophotonics* 6.3 (2017), pp. 561–576. DOI: [doi:10.1515/nanoph-2016-0132](https://doi.org/10.1515/nanoph-2016-0132). URL: <https://doi.org/10.1515/nanoph-2016-0132>.
- [3] Gouhei Tanaka et al. “Recent advances in physical reservoir computing: A review”. In: *Neural Networks* 115 (2019), pp. 100–123. ISSN: 0893-6080. DOI: <https://doi.org/10.1016/j.neunet.2019.03.005>. URL: <https://www.sciencedirect.com/science/article/pii/S0893608019300784>.
- [4] Keisuke Fujii and Kohei Nakajima. “Harnessing Disordered-Ensemble Quantum Dynamics for Machine Learning”. In: *Phys. Rev. Applied* 8 (2 Aug. 2017), p. 024030. DOI: [10.1103/PhysRevApplied.8.024030](https://doi.org/10.1103/PhysRevApplied.8.024030). URL: <https://link.aps.org/doi/10.1103/PhysRevApplied.8.024030>.
- [5] Rodrigo Martínez-Peña et al. *Dynamical phase transitions in quantum reservoir computing*. 2021. arXiv: [2103.05348](https://arxiv.org/abs/2103.05348) [quant-ph].
- [6] Daniel Manzano. “A short introduction to the Lindblad master equation”. In: *AIP Advances* 10.2 (Feb. 2020), p. 025106. ISSN: 2158-3226. DOI: [10.1063/1.5115323](https://doi.org/10.1063/1.5115323). URL: <http://dx.doi.org/10.1063/1.5115323>.
- [7] J.R. Johansson, P.D. Nation, and Franco Nori. “QuTiP: An open-source Python framework for the dynamics of open quantum systems”. In: *Computer Physics Communications* 183.8 (2012), pp. 1760–1772. ISSN: 0010-4655. DOI: <https://doi.org/10.1016/j.cpc.2012.02.021>. URL: <https://www.sciencedirect.com/science/article/pii/S0010465512000835>.

# Is air transport recovering from COVID-19? Dynamics of European airfares between November 2020 and June 2021

Elsa Rodríguez, Massimiliano Zanin

Instituto de Física Interdisciplinar y Sistemas Complejos, IFISC (CSIC-UIB)  
Campus Universitat de les Illes Balears, E-07122 Palma de Mallorca, Spain

## 1 Introduction

Since the World Health Organization declared the COVID-19 outbreak a pandemic in March 2020, societies around the world have had to cope with changes never seen in modern times. In addition to causing more than 4 million deaths around the world, COVID-19 has taken a huge toll in most economic sectors, with air transport possibly being the hardest hit (Suau-Sanchez, Voltes-Dorta, and Cugueró-Escofet 2020). Due to unprecedented decrease in passenger demand and national and international travel restrictions, airlines had to stop most operations and grounded entire fleets (Adrienne, Budd, and Ison 2020), many airports have closed their runways, and most companies in the aviation sector are working with minimum staffing on strict rotation. Even surviving flights required stricter hygiene standards, thus adding complexity to operations (Pongpirul et al. 2020). IATA's (International Air Transport Association) latest economic forecast reveals that in 2021 Europe is expected to be the worst-hit global region, with 22.2 billion net losses for airlines, 1.7 billion fewer passengers and a reduction of intra-European traffic of a 54%.

Within this gloomy picture, much hope is put on the 2021 summer season. Thanks to large-scale vaccination programs, the number of infections and their severeness has steadily been decreasing throughout 2021, allowing a relaxation of travel restrictions and an increase of air travel demand, especially associated with tourism. The magnitude of this recovery, and especially how healthy (from an economic perspective) this recovery is, are nevertheless still unknowns.

As well known in economic theory, market prices reflect to some extent the equilibrium between supply and demand, which is affected by exogenous and endogenous shocks and regulations. In other words, analysing price evolution allows to reconstruct a useful (if at times incomplete) picture of the market, and of the equilibrium of forces affecting it. A number of studies have used airfares in the past to analyse the air transport market dynamics, mainly focusing on the effects of the appearance of low-fare airlines in the market (Whinston and Collins 1992; Dresner, Lin, and Windle 1996; Morrison 2001; Brueckner, Lee, and Singer 2013), price and demand interactions (Zhang, Derudder, and Witlox 2014; Ren 2020), and impact of oil prices on airfares (Kaufmann 2017; Scotti and Volta 2018). These studies are usually limited by the complexity associated with securing airfare data, especially not aggregated and up-to-date ones.

In this contribution we analyse intra-European flight price dynamics in the November 2020 - June 2021 time period, with the objective of understand how the air transport market has evolved towards the summer 2021. We specifically compare how prices and number of flights between the 25 most important European airports have evolved; the former being a proxy of the demand, at least as perceived by airlines, and the latter of the offer. We further base our analysis on the hypothesis that a healthy recovery, i.e. a recovery mostly demand-driven, should reflect either in an increase in traffic (i.e. in offer) or in prices. In other words, either airlines try to catch a larger number of passengers, keeping their unitary revenue equal; or they try to increase the revenue per passenger, while maintaining a reduced number of flights (and hence, reducing operational costs). Most surprisingly, results show that, while traffic substantially increased, price did not, and actually lowered as summer 2021 was approaching. In other words, most of the recovery seems to have been supply-driven. This, together with a reduced difference between prices of tickets bought 7 and 30 days in advance, suggests

that demand did not fully recover possibly due to the uncertainty about the future evolution of the pandemic.

## 2 Airfares and auxiliary data sets

The main data set analysed in this work comprises prices of commercial (scheduled) direct flights between the 25 top European airports between November 2020 and June 2021. The list of all airports and associated main characteristics are reported in Tab. 1; note that, due to the decommissioning of Berlin Tegel Airport at the end of 2020, the data set effectively covers 24 airports. Information about the eight airlines here studied is also reported in Tab. 2. Prices have been collected daily using the Skypicker (lately known as Kiwi, see <https://docs.kiwi.com/>) API, using the following parameters in the search: only direct (no stopovers allowed) and one-way flights, one adult with no extra baggage, and with prices directly converted to Euro. Additionally, on each day, two searches have been executed, respectively for flights departing 7 and 30 days in the future. A total of  $25 \times 24 \times 2 = 1,200$  searches per day have been executed, and all yielded offers (with a limit of 100 results per search) have been saved for subsequent analysis. This amounts to a grand total of 1,197,835 records and 1.32GB of information. Note that, due to technical problems in the interface with the API, data for April 9th - 22nd and May 7th - 13th are missing.

In order to simplify the analysis of this data set, the lowest price offered by each airline for each route and for each day has been extracted and subsequently used. While multiple prices were usually available for each flight, e.g. corresponding to different seat classes, we only focused on the cheapest one as this better represent the offer - or ideally, the perception of the demand from the point of view of the airline. Similarly, whenever more than one flight of the same airline was available in one day, only the cheapest one has been retained.

The previous data set has been complemented by two additional sources of information. First of all, the number of flights daily operated between the aforementioned 25 airports has been extracted using the OpenSky Network API (see <https://opensky-network.org/apidoc/>, (Schäfer et al. 2014)), and specifically using the “flights” request. Secondly, we obtained the number of weekly diagnosed COVID-19 cases in Europe from the website [www.statista.com](http://www.statista.com) (Statista 2021).

## 3 Results and discussion

### 3.1 Global price evolution

We start by analysing the global evolution of prices, i.e. independently of specific routes and airlines. Fig. 1 reports the evolution of the average price in Europe (black lines), both for trips booked 7 (left panel) and 30 days in advance (right panel). These time series are divided by the first of their values, in order to create an index of price evolution. The resulting time series thus represent how airfares have in general evolved throughout Europe, with values greater than one indicating an increase with respect to the initial day (November 21th, 2020). It can be appreciated that the average price varied little in the considered time period, except within two abnormal windows. The first approximately corresponds to the first week of December 2020 for the 7 days graph, and to the last weeks of November 2020 in the 30 days graph. Prices in this window increased between 20 and 50%, both for tickets bought 7 and 30 days in advance; this, combined with the increase in the number of operations in the following weeks (red lines), suggests that airlines were reacting to a substantial increase in demand caused by the winter holidays. The second window started at around May 2020, and continued essentially until the end of available data. In this case, airfares initially increased in the case of 7 days, but decreased for 30 days; and, in both cases, they converged back to values close to the initial ones. The behaviour during summer 2021 will be further analysed in Sec. 3.2.

For the sake of completeness, Fig. 1 also reports the evolution of the average price for all flights departing from each airport (see the 50 blue thin lines in both panels). It can be appreciated that individual airports present a high variability, also associated with a weekly periodicity. Finally, the

Airport name	IATA code	Num. flights	Num. records	Airport name	IATA code	Num. flights	Num. records
Heathrow Airport	LHR	4,508	58,598	Humberto Delgado Airport	LIS	2,770	49,248
Paris Charles de Gaulle Airport	CDG	5,189	79,550	Copenhagen Airport, Kastrup	CPH	1,371	35,732
Amsterdam Airport Schiphol	AMS	6,438	126,724	Palma de Mallorca Airport	PMI	3,176	71,288
Frankfurt Airport	FRA	7,250	92,578	Manchester Airport	MAN	2,714	14,672
Adolfo Suárez Madrid - Barajas Airport	MAD	2,958	118,570	Milan Malpensa Airport	MLX	1,361	14,713
Barcelona - El Prat Airport	BCN	4,084	85,218	Oslo Airport	OSL	1,808	23,378
Istanbul Airport	IST	72	52,387	Brussels Airport	BRU	1,738	27,789
Munich Airport	MUC	4,376	53,695	Athens International Airport Eleftherios Venizelos	ATH	66	19,259
Rome - Fiumicino International Airport	FCO	393	37,733	Paris Orly Airport	ORY	198	18,439
Dublin Airport	DUB	2,221	26,648	London Stansted Airport	STN	3,592	6,785
Vienna International Airport	VIE	878	37,521	Stockholm Arlanda Airport	ARN	1,602	34,523
Zurich Airport	ZRH	2,770	41,370	Düsseldorf Airport	DUS	3,229	32,465

Table 1: List of the 24 airports considered in this study, along with their IATA designator, and the recorded number of flights and price records. Airports are ordered according to their number of passengers through 2019. Note that the 25th airport, Berlin Tegel, has been excluded due to it been decommissioned at the end of 2020.

Airline	Number of flights	Number of records
Air France	12,878	103,549
Lufthansa	12,922	163,026
Iberia	6,252	115,585
British Airlines	1,079	34,539
TAP Portugal	2,123	50,511
KLM Royal Dutch Airlines	7,159	166,130
Swiss International Airlines	2,165	39,147
Alitalia	14,418	24,761

Table 2: List of the eight major airlines analysed in this study, along with the corresponding recorded number of flights and price records.

bottom graph (gold lines) represents the number of weekly diagnosed COVID-19 cases in Europe throughout the considered time period.

In order to understand how airlines have adapted to different levels of demand, the top panels of Fig. 2 report scatter plots of the average airfares across Europe for each day  $t$ , as a function of the number of operations recorded for the same day  $t$ . Both graphs are dominated by the final part of the data set, for which the traffic substantially increased (see again Fig. 1). Notably, while no statistically significant change in prices is observed for 7 days, they significantly decreased with traffic in the case of 30 days. The bottom panels of Fig. 2 further depict the evolution of the average airfares weighted by the number of operations. In other words, for each pair of airports, the normalised price is multiplied by the number of flights detected between them; the final number is then calculated as the average over all pairs of airports. This weighted price can thus be understood as a proxy of the quantity of money involved in all flights in the system, with highly connected pairs of airports contributing more to the final result. Both in the 7 and 30 days cases, a statistically significant positive correlation is observed. When combined with the previous results, this suggests that the increase in demand (and hence in the flight offer) has been mostly driven by a reduction in prices; the significance of this will

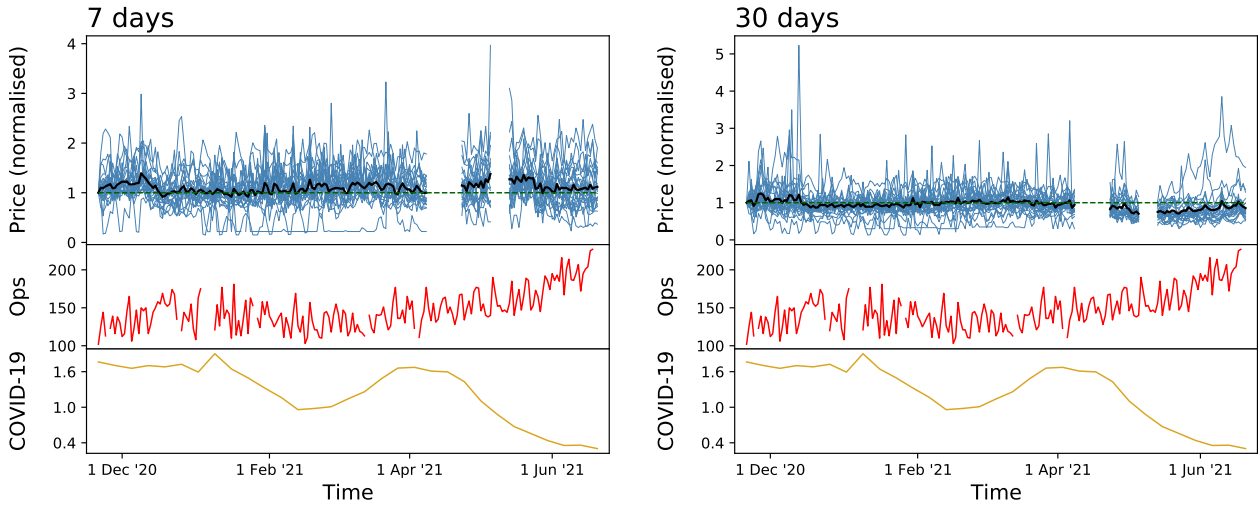


Figure 1: Evolution of average airfares. The left and right top panels respectively depict the average prices, normalised according to the average price in the first day, for flights bought 7 and 30 days in advance. The 50 blue thin lines correspond to the average price of flights departing from each one of the 50 considered airports, and the two black thick lines the average across all airports. Bottom panels further reports the evolution of the daily number of operations (red lines) and of the weekly number of reported new COVID-19 cases (gold lines).

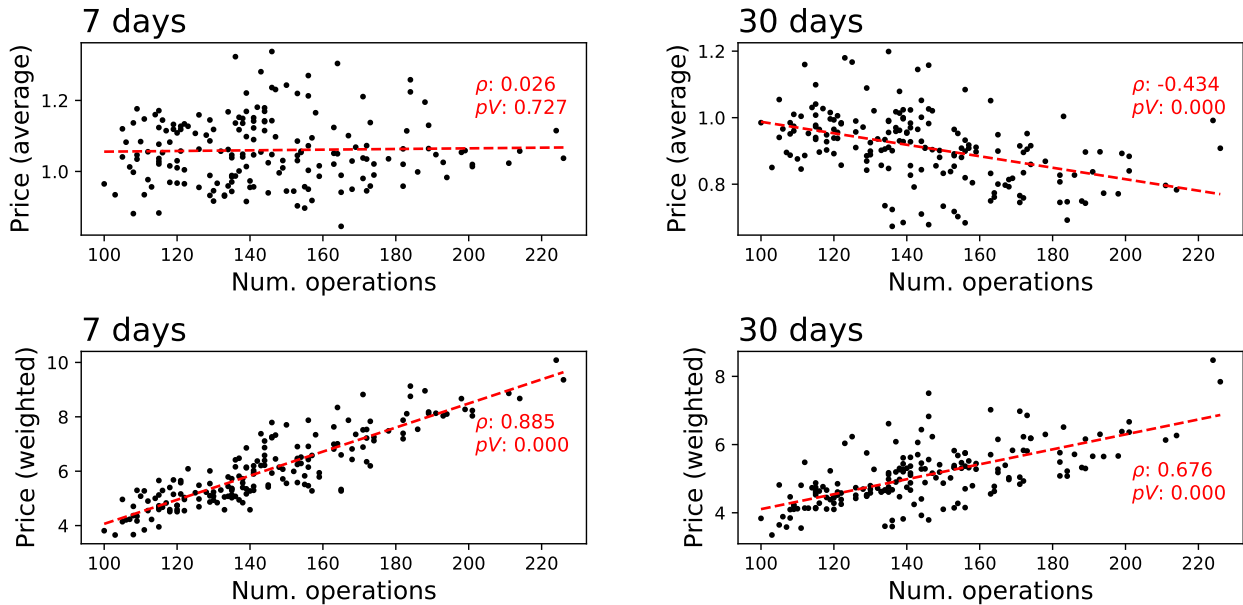


Figure 2: Relationship between prices and traffic volume. The two top panels report scatter plots of the average daily prices (across all airports) as a function of the number of operations; the two bottom panel, plots of the prices weighted by number of operations (see main text for details), also as a function of the number of operations. Left and right panels respectively correspond to tickets bought 7 and 30 days in advance. Red dashed lines report the best linear fit, with the corresponding slope ( $\rho$ ) and  $p$ -value ( $pV$ ) included in each panel.

further be explored in Sec. 4.

We further analyse the evolution of the difference between prices of flights booked 7 and 30 days in advance. Fig. 3 reports the such difference as  $\Delta p(t) = \log_2 \langle p_7(t) \rangle / \langle p_{30}(t) \rangle$ , with  $p_7(t)$  and  $p_{30}(t)$

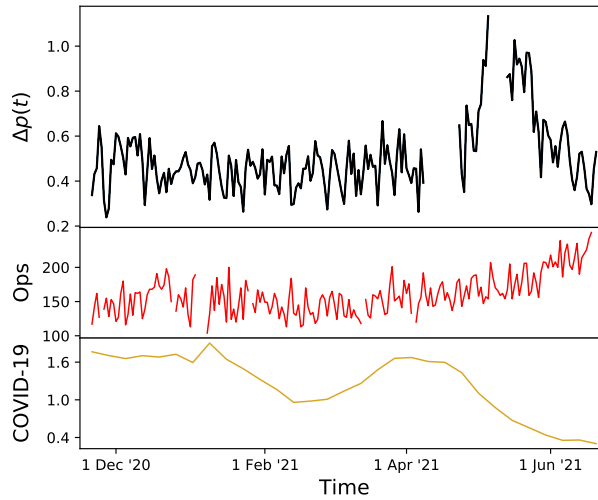


Figure 3: Evolution of the differential between prices of tickets bought 7 and 30 days in advance ( $\Delta p(t)$ , see main text for definition) as a function of time. Bottom panels further report the evolution of the daily number of operations and of the daily number of reported new COVID-19 cases in millions, as per Fig. 1.

respectively been prices of flights booked 7 and 30 days in advance, and  $\langle \rangle$  the mean operator. Positive (respectively, negative) values of  $\Delta p(t)$  thus indicate that prices were higher (lower) for flights booked 7 days in advance with respect to 30 days; specifically, a value of  $\Delta p(t) = 1$  implies that  $\langle p_7(t) \rangle$  was double than  $\langle p_{30}(t) \rangle$ . While pricing dynamics can at times be more complex and may depend on the considered city pair (Malighetti, Paleari, and Redondi 2010; Law et al. 2011),  $p_7(t)$  is usually expected to be higher than  $p_{30}(t)$ , as tickets bought with four weeks in advance are usually more sensitive to price variations. It can be appreciated that  $\Delta p$  has been positive all the time, as is to be expected, but with values stable around 0.4, i.e. indicating small differences; only during May 2021 it did increase above 1.0. The small difference between  $p_7(t)$  and  $p_{30}(t)$  can then point towards a scenario in which airlines struggle to fill aircraft, thus being forced to keep prices low even when the day of the flight is approaching, in order to catch any residual demand. This finding will further be interpreted in Sec. 4.

Moving to a higher level of detail, Fig. 4 reports the evolution through time of the average prices of flights operated by each airline. For the sake of clarity, the eight airlines here considered have been organised in two groups, respectively depicted in left and right panels. Additionally, the top panels correspond to the evolution of prices for flights booked 7 days in advance, bottom panels 30 days in advance. It can be appreciated that airfares at the airline level are highly variables. Some of them, as for instance British Airways and KLM, have very cyclic weekly variations; at the same time, again British Airlines and TAP present strong peaks during some specific days. With respect to the results presented in Figs. 1 and 3, Fig. 4 suggests that airlines have changed airfares towards summer 2021 in different ways. Specifically, some of them had little or no increases, as e.g. Lufthansa or Alitalia; on the other hand, significant increases can be observed for other airlines, like Iberia or KLM. This latter one presents an interesting dynamics, with a sharp increase in prices of tickets bought 7 days in advance, but almost no change in the 30 days case. The analysis of the dynamics of airfares during summer 2021 will be the focus of the next section.

### 3.2 Airfare evolution during summer 2021

Previous results seem to suggest that some airlines have changed their airfare policies when approaching summer 2021. To understand whether this change was promoted by a corresponding change in expected demand, we compared ticket prices between January 2021, i.e. a month with little traffic and generally low prices (see Fig. 1), and June 2021.

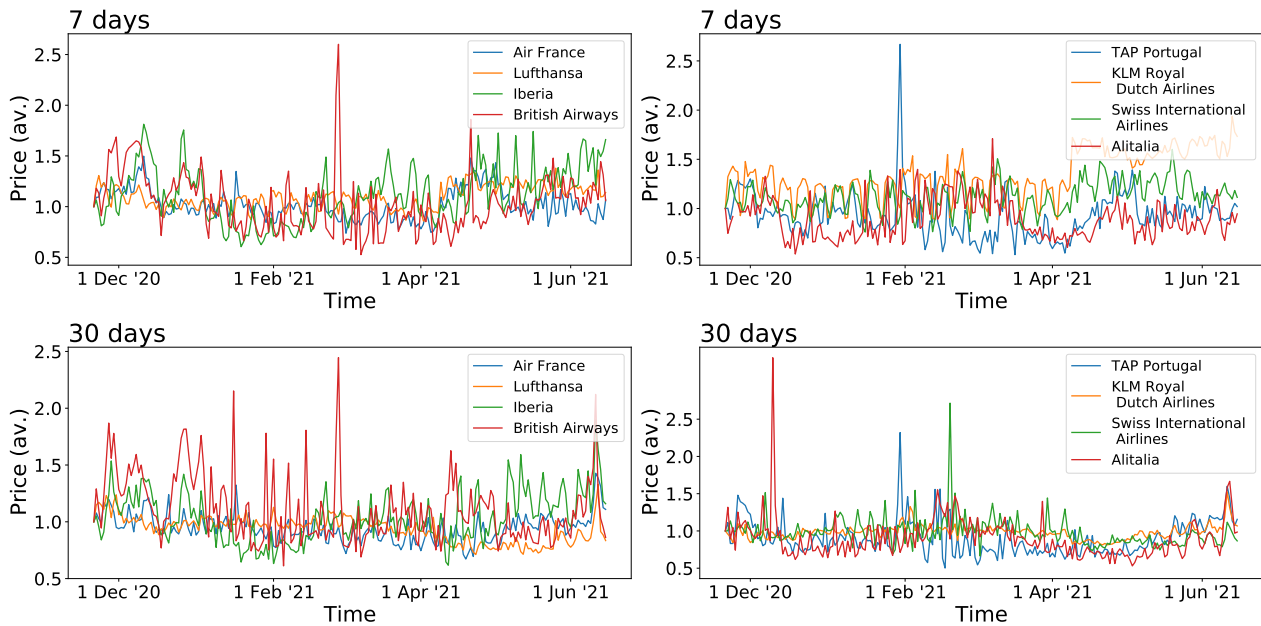


Figure 4: Evolution of average prices per airline. Top and bottom panels respectively correspond to tickets bought 7 and 30 days in advance, and prices are normalised according to the price observed on the first day. The eight considered airlines are organised in two groups, respectively included in left and right panels, for the sake of clarity.

Fig. 5 firstly displays the evolution of average airfares for the eight airlines here considered, both for January (blue columns) and June (orange columns) 2021, and for tickets bought 7 (top panel) and 30 (bottom panel) days in advance. While most airlines have increased their airfares in the 7 days case, the same is not true for the 30 days; on the contrary, Lufthansa, British Airways and Swiss display significant decreases.

If one assumes that an increase in airfares is the direct consequence of an increase in demand, these results can be explained in terms of two opposite forces. On one hand, June 2021 continues a steady trend of reducing COVID-19 incidence, as shown in the bottom panel of Fig. 1; on the other hand, policies concerning international travels (including what regions are deemed safe, the need of tests and quarantines on return, and so forth) were not relaxed, and in some cases even changed abruptly in response to the detection of new variants. While the first factor may have fostered an increase in demand, the second may have hindered longer term plans, and hence actually reduced the demand of flights associated with activities planned one month in advance, as is the case of leisure travel.

This price dynamics has nevertheless not been homogeneous across Europe as shown in Fig. 6, depicting the pairs of airports for which the airfares have mostly increased (red links) and decreased (green links) between January and June. Most of the price increases are focused on Istanbul, with the major exception been flights from Madrid to Balearic Islands. The former cases can be explained by the low prices observed during January (i.e. around 50-60 Euro), and by the recovery of more normal fares with the opening of country's borders. The case of Balearic Islands (and specifically of Palma de Mallorca) can further be explained in terms of increasing touristic trips. The evolution of route prices are further reported in numerical form in Tabs. 3 and 4, respectively for the top-5 routes that experienced the largest increase and decrease in prices.

The lack of homogeneity in price dynamics can also be observed in Fig. 7, which depicts the routes for which the spread between the prices offered by different airlines has changed. This spread is calculated as the difference between the lowest and the highest prices offered by different airlines for the same routes, always considering the lowest one offered by each airline. This spread thus represents the asymmetry in the market, and the fact that one airline can charge a higher fee for the same route thanks to a higher demand in its national market. As can be appreciated in Fig. 7, most routes have an increased spread, especially those starting and ending in Spain and Portugal. This may represent

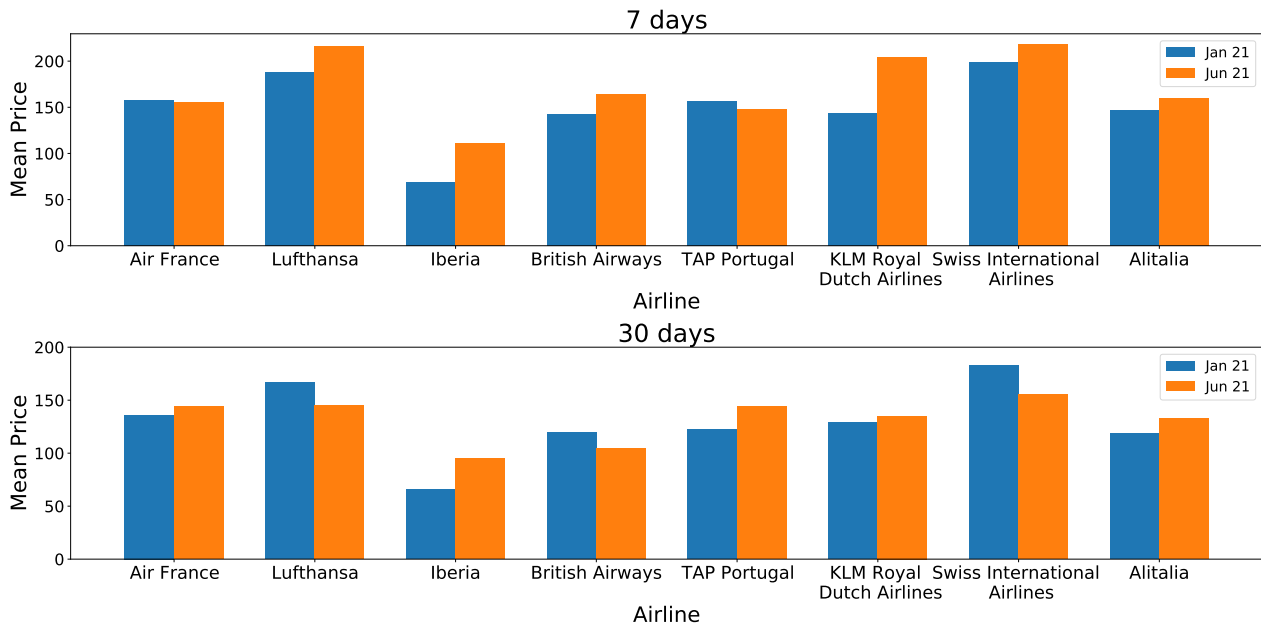


Figure 5: Average airfares per airline, for flights bought in January (blue columns) and June (orange columns) 2021, and bought 7 (top panel) and 30 (bottom panel) days in advance.

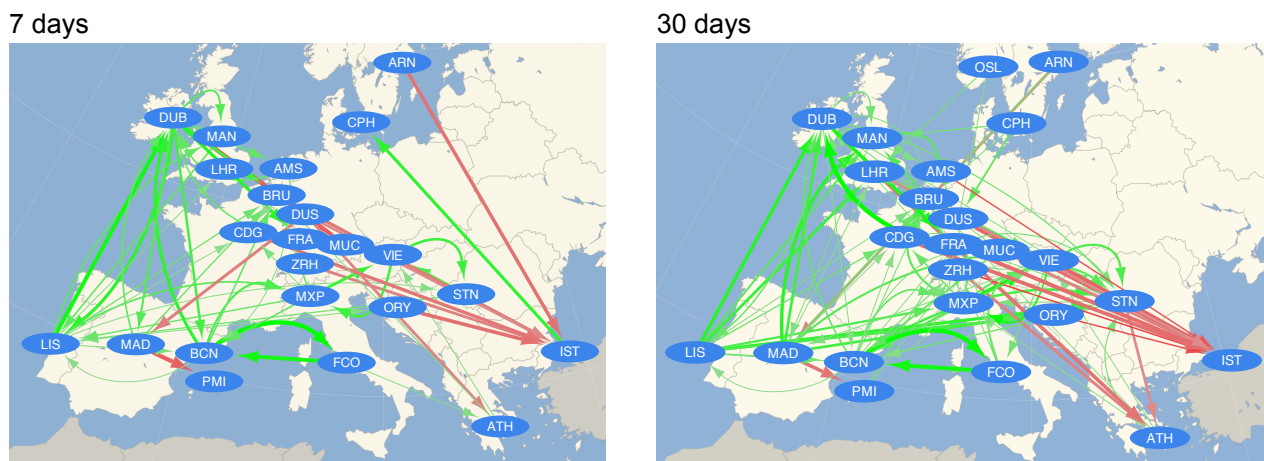


Figure 6: Graphical representation of price evolution by routes. Arrows represent routes for which prices have more than doubled (red) or reduced by half (green), with the thickness and colour shade being proportional to the change. Left and right maps respectively correspond to tickets bought 7 and 30 days in advance.

an asymmetry in demand, i.e. tourists from Germany or UK (possibly booking flights of respectively Lufthansa and British Airways) are more willing to go to Spain, while the opposite (i.e. Spanish tourists travelling abroad through Iberia) is not always true.

## 4 Conclusions

In this contribution we have analysed the evolution of airfares between the 25 largest European airports from November 2020 to June 2021, thus corresponding to the time window in which air transport was recovering from the effects of the COVID-19 global pandemic. The analysis has mainly been based on two complementary aspects: the evolution of prices across the whole time period, and the specific behaviour of the system when approaching summer 2021.

		7 days				30 days	
Dep.	Dest.	Mean price	Mean price	Dep.	Dest.	Mean price	Mean price
Airpor	Airport	January '21	June '21	Airpor	Airport	January '21	June '21
MUC	DUB	74.00	250.52	ZRH	IST	54.00	257.19
MAD	PMI	23.18	74.74	BRU	IST	58.53	256.32
ORY	IST	74.32	204.53	ORY	IST	74.47	295.90
ARN	IST	112.19	299.71	AMS	IST	59.85	220.10
CDG	IST	107.27	273.93	VIE	IST	64.14	203.81

Table 3: List of the five routes that have seen the greatest increase in price between January and June 2021, for tickets bought 7 (left part) and 30 (right part) days in advance. Airports are identified by their IATA code.

		7 days				30 days	
Dep.	Dest.	Mean price	Mean price	Dep.	Dest.	Mean price	Mean price
Airpor	Airport	January '21	June '21	Airpor	Airport	January '21	June '21
VIE	MXP	113.89	11.48	BCN	FCO	324.29	33.35
FRA	DUB	173.35	18.39	LIS	DUB	154.93	18.76
BCN	FCO	220.85	24.39	FCO	BCN	325.26	41.29
MXP	VIE	106.46	12.81	DUB	FRA	175.58	28.10
FCO	BCN	191.89	23.90	DUB	LIS	164.50	27.27

Table 4: List of the five routes that have seen the greatest reduction in price between January and June 2021, for tickets bought 7 (left part) and 30 (right part) days in advance. Airports are identified by their IATA code.

### 7 days



### 30 days

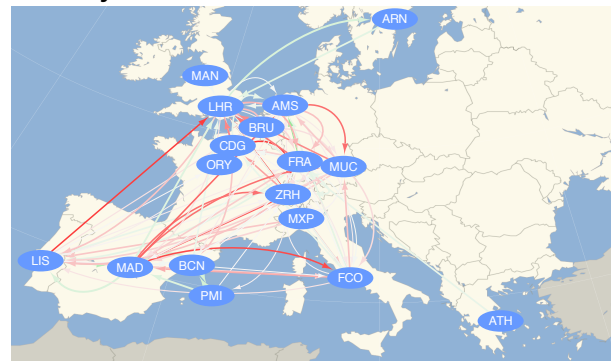


Figure 7: Graphical representation of the routes for which the spread between the prices offered by different airlines has increased (red arrows) or decreased (green arrows). The thickness and colour shade of arrows are proportional to the magnitude of the change. Left and right maps respectively correspond to tickets bought 7 and 30 days in advance.

As well known from economic theory, price reflects demand and supply opposing forces. Both sides are strongly affected by the major exogenous shock represented by the ongoing COVID-19 pandemic. Contrary to exogenous shocks typically considered in the literature, the pandemic is not impulse-like but has its own complex dynamics and quasi-periodicities, and is more or less predictable depending on the phase within each cycle (Tsallis and Tirnakli 2020; Tuli et al. 2020; Zhang, Ma, and Wang 2020; Giuliani et al. 2020). In a recovering scenario, an increase in the air demand (as e.g. due to an increase in tourism) is to be expected. Airlines would then respond in two complementary ways: by maintaining their offer and rising airfares, or by increasing the offer at the expense of maintaining similar prices. What observed in Fig. 1 is nevertheless different: starting from May 2021, traffic has increases at the expense of a reduction in the average airfare, especially for tickets bought 30 days

in advance. This seems to suggest the opposite arrow of causality, i.e. that the increased number of passengers has been due to a decrease in prices, and not by an increase in the demand. In other words, airlines may have increased their activity in exchange for a reduction in their profit margins.

Fig. 3 also sheds light on the evolution of the market. In normal market conditions, prices for tickets bought one week in advance should be substantially higher than the the ones for the same flight booked one month in advance. As can be observed in Fig. 3, this difference was nevertheless minimal until April 2021. In other words, the uncertainty about the evolution of the pandemic prevented people from making long term plans, with a subsequent reduction in the demand. The market explored a more healthy condition throughout May 2021, but the price differential again reduced in June 2021; as previously speculated, this seems to indicate that the higher demand was the result of (and has been fuelled by) lower fares. In addition, the fact that airfares have not generally increased for tickets bought 30 days in advance, but instead have been reduced by some airlines (see Fig. 5), further suggests that the demand has been constrained by the uncertainty associated with changing health policies; in other words, tourists may avoid long-term plans, and only buy tickets one month in advance if their price is below what normally expected.

In synthesis, the analysis here presented suggests a complex scenario. On one hand, traffic volumes have partly recovered pre-pandemic levels, something clearly positive for the air transport sector. On the other hand, this growth also shows negative aspects, as a general reduction of airfares, especially associated with medium-term plans; and a strong asymmetry in price evolution, with only a few destinations (mainly Istanbul and Palma de Mallorca) associated with higher fares. This points towards an unhealthy recovery of air transport, in which traffic is fuelled by lower prices but is not supported by an increase in demand; on the contrary, the latter seems to be hindered by the uncertainty associated with changing health policies and regulations. Note that supply can also have increased for reasons not analysed in this work, as for instance the need of maintaining slots rights at major airports, forcing airlines to fly so-called *ghost flights* (Haanappel 2020; Sun et al. 2021).

As a final point, it is important to highlight the limitations of the present study, which mainly come from the limitations and uncertainties associated to airfare data. On one hand, flight prices can fluctuate throughout the day, and what recorded at a given time can change in the following hours. Additionally, as they are downloaded by an automated software program, even if from a reputable source, mistakes or false data can always appear, resulting in potentially noisy (or not continuous, as the case here) time series. On the other hand, even if price data were completely correct, they only represent one aspect of the market, i.e. the supply side. A more complete picture can only be obtained by combining information about the demand, e.g. actual number of passengers or ticket sold (here only indirectly represented by the number of operated flights), or even by information about the price elasticity of demand (Brons et al. 2002). While here the number of flights has been used as a proxy of the market size, this does not include (and does not substitute) a true assessment of the seats offered, or of the achieved load factor (Kölker, Bießlich, and Lütjens 2016).

## Acknowledgments

This work was supported by the SURF@IFISC fellowship.

## References

- Adrienne, Nena, Lucy Budd, and Stephen Ison. 2020. “Grounded aircraft: An airfield operations perspective of the challenges of resuming flights post COVID.” *Journal of Air Transport Management* 89: 101921.
- Brons, Martijn, Eric Pels, Peter Nijkamp, and Piet Rietveld. 2002. “Price elasticities of demand for passenger air travel: a meta-analysis.” *Journal of Air Transport Management* 8 (3): 165–175.
- Brueckner, Jan K, Darin Lee, and Ethan S Singer. 2013. “Airline competition and domestic US airfares: A comprehensive reappraisal.” *Economics of Transportation* 2 (1): 1–17.
- Dresner, Martin, Jiun-Sheng Chris Lin, and Robert Windle. 1996. “The impact of low-cost carriers on airport and route competition.” *Journal of Transport Economics and Policy* 309–328.

- Giuliani, Diego, Maria Michela Dickson, Giuseppe Espa, and Flavio Santi. 2020. “Modelling and predicting the spatio-temporal spread of COVID-19 in Italy.” *BMC infectious diseases* 20 (1): 1–10.
- Haanappel, Peter PC. 2020. “Slots: use it or lose it.” *Air and Space Law* 45 (Special issue).
- Kaufmann, Robert K. 2017. “Airfares and oil prices: ‘Feathers and Rockets’ adjustments.” *Energy Economics* 68: 515–521.
- Kölker, Katrin, Peter Bießlich, and Klaus Lütjens. 2016. “From passenger growth to aircraft movements.” *Journal of air transport management* 56: 99–106.
- Law, Rob, Rosanna Leung, Basak Denizci Guillet, and Hee “Andy” Lee. 2011. “Temporal changes of airfares toward fixed departure date.” *Journal of Travel & Tourism Marketing* 28 (6): 615–628.
- Malighetti, Paolo, Stefano Paleari, and Renato Redondi. 2010. “Has Ryanair’s pricing strategy changed over time? An empirical analysis of its 2006–2007 flights.” *Tourism management* 31 (1): 36–44.
- Morrison, Steven A. 2001. “Actual, adjacent, and potential competition estimating the full effect of Southwest Airlines.” *Journal of Transport Economics and Policy (JTEP)* 35 (2): 239–256.
- Pongpirul, Krit, Kanitha Kaewpoungngam, Korn Chotirosniramit, and Sinnop Theprugsa. 2020. “Commercial airline protocol during COVID-19 pandemic: An experience of Thai Airways International.” *Plos one* 15 (8): e0237299.
- Ren, Junqiushi. 2020. “Fare impacts of Southwest Airlines: A comparison of nonstop and connecting flights.” *Journal of Air Transport Management* 84: 101771.
- Schäfer, Matthias, Martin Strohmeier, Vincent Lenders, Ivan Martinovic, and Matthias Wilhelm. 2014. “Bringing up OpenSky: A large-scale ADS-B sensor network for research.” In *IPSN-14 Proceedings of the 13th International Symposium on Information Processing in Sensor Networks*, 83–94. IEEE.
- Scotti, Davide, and Nicola Volta. 2018. “Price asymmetries in European airfares.” *Economics of transportation* 14: 42–52.
- Statista. 2021. “Cumulative number of coronavirus (COVID-19) cases in Europe between January 25, 2020 and June 27, 2021.” Accessed 2021-07-01. <https://www.statista.com/statistics/1102896/coronavirus-cases-development-europe/0>.
- Suau-Sanchez, Pere, Augusto Voltes-Dorta, and Natàlia Cugueró-Escofet. 2020. “An early assessment of the impact of COVID-19 on air transport: Just another crisis or the end of aviation as we know it?” *Journal of Transport Geography* 86: 102749.
- Sun, Xiaoqian, Sebastian Wandelt, Changhong Zheng, and Anming Zhang. 2021. “COVID-19 pandemic and air transportation: Successfully navigating the paper hurricane.” *Journal of Air Transport Management* 102062.
- Tsallis, Constantino, and Ugur Tirnakli. 2020. “Predicting COVID-19 peaks around the world.” *Frontiers in Physics* 8: 217.
- Tuli, Shreshth, Shikhar Tuli, Rakesh Tuli, and Sukhpal Singh Gill. 2020. “Predicting the growth and trend of COVID-19 pandemic using machine learning and cloud computing.” *Internet of Things* 11: 100222.
- Whinston, Michael D, and Scott C Collins. 1992. “Entry and competitive structure in deregulated airline markets: an event study analysis of People Express.” *The RAND Journal of Economics* 445–462.
- Zhang, Shengrun, Ben Derudder, and Frank Witlox. 2014. “The determinants of full-service carriers airfares in European hub-to-hub markets.” *European Journal of Transport and Infrastructure Research* 14 (4).
- Zhang, Xiaolei, Renjun Ma, and Lin Wang. 2020. “Predicting turning point, duration and attack rate of COVID-19 outbreaks in major Western countries.” *Chaos, Solitons & Fractals* 135: 109829.

# Power grid stability in scenarios of large renewable penetration

Guillermo Pérez de Arenaza Pozo, Pere Colet and Damià Gomila  
Instituto de Física Interdisciplinar y Sistemas Complejos, IFISC (CSIC-UIB)  
Campus Universitat de les Illes Balears, E-07122 Palma de Mallorca, Spain

## Abstract

Our society is nowadays facing an enormous challenge, due to ecological, economic, cultural, social, and political factors we must transition to renewable energies. Thus, the EU and Spain have done huge investments to develop the pertinent infrastructures [1]. Promoting clean energies has resulted in a significant increment of their penetration in the power grid, changing its properties and behavior. The electrical grid plays a vital role on our daily lives, that is why we need to ensure its reliability. Consequently, renewable energies penetration growth must be accompanied with improvements on the electrical grid frequency control systems.

In despite of the obvious benefits that renewable energy has, there are many downsides to these types of technologies (lower reliability, less power density, generation driven by natural phenomena. . .). We will focus on those affecting the power grid; low reliability and generation dependance on natural phenomena.

This paper is a study on the consequences of large renewable penetration in Gran Canaria's power grid. We will discuss the stability and reliability of the power grid as well as possible actions that can be taken to improve its properties.

## 1 Introduction

The electrical grid is a network that connects producers and consumer, they vary in size, some cover vast surfaces providing electricity to whole countries or continents while others are very small providing services to only a few thousand people. They consist of power stations (produce energy), electrical substations (step up/down voltage), transmission lines (carry power over very long distances), distribution lines (carry power to populations) and load (the users).

Electricity is very difficult to store, nowadays Spain has a storage capacity of 8.3 GWh [2], very little compared to the total installed power of 111,17 GW [3]. Thus, there must be a continuous balance between the electricity generated and the demand. If this balance is not reached, there will be a deviation from the nominal frequency (50 Hz). European regulation forces the electric grid operator (Red Electrica Española, REE) to maintain those deviations within a range of frequencies.

There are three main mechanism that can be used to control the frequency. The first one is known as primary frequency response, it is responsible for limiting the frequency drop/rise, so the deviation is not too big. It works very fast (in a few seconds), but it does not restore the frequency to 50 Hz. Once the primary regulation accomplishes its target, the frequency is still different from 50 Hz, the secondary frequency response brings back the frequency to 50 Hz. In order to do it, there are special generators using reserve power, this reserve is a percentage of the generator total power capacity. Finally, we have the tertiary control, which replenish the reserves of the other two mechanisms.

Most of the conventional power plants (hydroelectric, diesel, combined cycle. . .) are able to adapt their generation to the demand. Every day, REE does a forecast of the expected electricity consumption, and the power plants plan their production to match the demand [4], during the day little modifications of the production are done to cover for small errors in the forecast. Following this protocol, frequencies mechanisms are only necessary when abrupt changes take place (for example a big consumer or producer disconnects from the grid).

One of the main problems that renewable energies entail is that these power plants cannot adapt their generation to the demand, especially wind power and photovoltaic plants. As these technologies depend on natural phenomena (wind and solar irradiation), if there is an increase on the load, they are not able to cope with it. Nowadays, in the Spanish electric market, solar and wind power plants always generate as much power as they can, without taking into account the

demand forecast, the rest of the power needed to match with the load it produced by conventional plants, which can adapt to the user's consumption.

This model works because the demand is much higher than the power produced by renewable energies. In this paper we will study a scenario where there is a greater penetration of renewable energies, we will discuss if this model is still valid and what improvements (if any) should be made. In order to simplify our study, we are going to focus on the electric grid of the island of Gran Canaria. Its share of sources of energy is the following [5]:

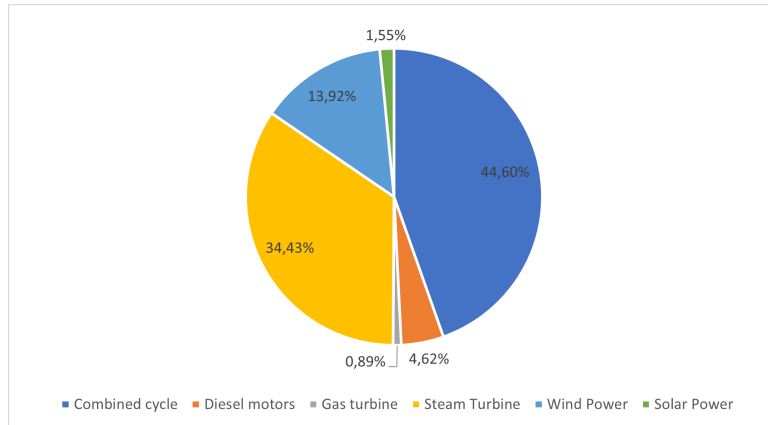


Figure 1: Share of power generation in Gran Canaria

As it is observed in figure 1, only a 14.47% of the energy produced in Gran Canaria is renewable energy. The Spanish government has imposed the objective of at least a 42% [6] of renewable energies by 2030. In only a few years the electrical grid will have to cope with twice as much renewable energy.

In this paper, we will first develop a model that simulates the energy production in the island. In order to simplify it, we consider that all the generation is concentrated in a theoretical generator that represents all of the producers in Gran Canaria. Once we have the model, using real data from the frequency in the electrical grid, we will adapt the model so it controls correctly the frequency. That model is going to be our reference model (it represents how currently power generation works on Gran Canaria).

Once we have the reference model, we will increase the share of renewable energies up to 30%. This way we can study how it affects to the electrical grid stability and reliability. Finally, we will adapt the model (changing its control parameters) in order to get a reliable frequency control, through this procedure we will be able to know which changes have to be made in the power grid control system.

The frequency control system are part of the conventional energy producers. Even if the renewable energies grow greatly, we must still maintain at least part of the conventional generators for the shake frequency stability. Figure 2 shows the share of installed power in Gran Canaria.

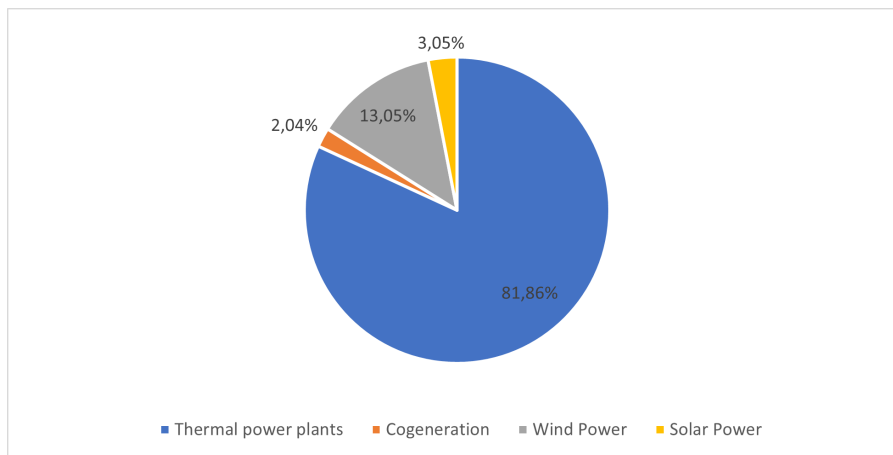


Figure 2: Share of installed power in Gran Canaria

## 2 Theoretical model

In this part we will describe the theoretical model of a conventional electric generator. An electric generator is a device which transforms mechanical energy into electrical one using electromagnetic induction. Using a fuel source (gasoline, oil, coal, moving water...), they move a rotating component called rotor, which generates a rotating magnetic field. Inside the generator we can also find the stator, a stationary component, which is made up of three sets of coils. The magnetic field produced by the rotor generates an electric current in the coils of the stator.

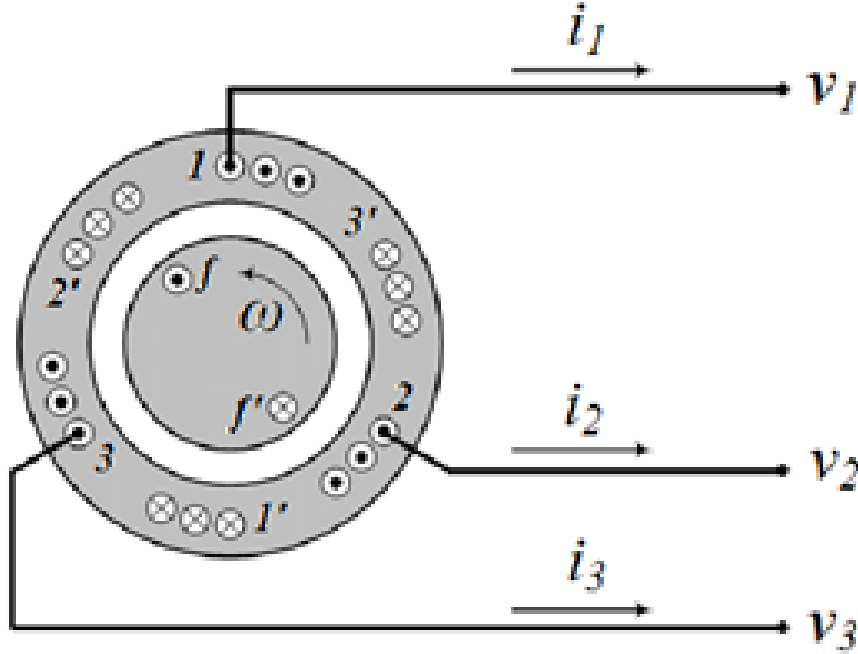


Figure 3: diagram of synchronous generator with three phases. Source: [https://www.researchgate.net/figure/Schematic-diagram-of-a-three-phase-synchronous-generator\\_fig12\\_274194617](https://www.researchgate.net/figure/Schematic-diagram-of-a-three-phase-synchronous-generator_fig12_274194617)

In this study, we will aggregate all the generators power by a single generator with a mechanical power of  $P_m$ , analogously we will model the electric demand as a single load:  $P_l$ . Thus, the generator will be asked for  $P_l$  electric power, which will be produced with  $P_m$  mechanical power. This relation is described by Eq. (1):

$$J \frac{dw}{dt} = T_m - T_e. \quad (1)$$

Where  $w$  is the angular frequency at which the rotor is spinning, the  $J$  is the moment of inertia, and  $T_e$  and  $T_m$  are the electrical and mechanical torque respectively. From Eq. (1) we can directly infer the effect that the balance between the load and the production will have over the frequency. If there is more demand than production ( $T_e > T_m$ ) the frequency of the electrical grid will decrease, on the other hand if there is more production than load ( $T_e < T_m$ ) the frequency will increase.

The power and torque are related by Eq. (2):

$$P_m = T_m w. \quad (2)$$

Thus, if we multiply Eq. (3) by  $w$  we will get the following equation:

$$wJ \frac{dw}{dt} = P_m - P_e. \quad (3)$$

In parallel, we can define the inertia constant of the generator  $H$  by the ratio between the kinetic energy of the system and the MVA rating of the generator ( $P_n$ ), this relation is described in Eq. (4).

$$H = \frac{1}{2} \frac{Jw^2}{P_n}. \quad (4)$$

Using Eq. (4) in Eq. (3) we get the following expression:

$$\frac{2HP_n}{w} \frac{dw}{dt} = P_m - P_e. \quad (5)$$

From Eq. (5) we can directly infer that the change of frequency due to the balance of load and produced power is:

$$\frac{dw}{dt} = \frac{w}{2HP_n} (P_m - P_e). \quad (6)$$

From here on, we will call  $w$  the frequency deviation from its nominal value ( $w_{ref} = 50Hz$ ), thus the real frequency the system ( $w_r$ ) has is:

$$w_r = w + w_{ref}. \quad (7)$$

In order to describe the change of frequency in the system correctly, we should take into account that some of the users (such as motors) change their consumption with frequency

$$P_e(t, w) = (1 + \frac{D}{w_r} w) P(t). \quad (8)$$

Finally, Using Eq. (7) and Eq. (8) in Eq. (6) we get the final expression:

$$\frac{dw}{dt} = \frac{w_r^2}{2HP_n(w + w_r)} (P_m - (1 + \frac{D}{w_r} w) P_l). \quad (9)$$

Where  $P_m$  is the mechanical power and  $P_l$  is the load that the generator has to bear. In order to describe fully the generator, we also need to take into account the frequency control systems that regulate its behaviour. The following equation describes the primary and the secondary control systems respectively:

$$\frac{\partial P_m}{\partial t} = \frac{1}{\tau} (P_s - P_m - \frac{P_r}{R} \frac{w}{w_r}). \quad (10)$$

$$\frac{\partial P_s}{\partial t} = -k \frac{w}{w_r}. \quad (11)$$

Finally, with Eq. (9), Eq. (10) and Eq. (11) the generator model behaviour is fully described. There are many constants which values have not been yet established, in order to do so we will use public data from REE of the demand in 2019 [7], and frequency measurements provided by the IFISC [?]. The demand data will allow us to adapt (giving the correct values for the model's constant) the generator to Gran Canaria's demand.

With the frequency data we will establish the quality of the current electric grid as a reference for the discussions of different scenarios. In order to analyse it we will choose the following statistical indicators: the pdf, the standard deviation and the Kurtosis. Additionally we will calculate how much time the deviation surpasses 0.2 Hz and the peak frequency deviation.

With the objective of having a thorough study, we will develop a model for energy storage. In order to simplify model, we will assume that it behaves similarly to a conventional generator, with a few differences. Unlike a generator, a battery has an energy limit (it cannot provide power indefinitely). Thus, we will add a variable  $Q_{max}$ , indicating the nominal capacity of the battery. The capacity relation with the provided power is described in the following equation.

$$\frac{dQ_{max}}{dt} = -P_b. \quad (12)$$

Where  $P_b$  is the given power of the battery. For the simulation we have a battery with enough capacity to bear during an hour with the electric demand. The maximum demand was of 530 MW, consequently  $Q_{max} = 530MWh$ . This is a realistic scenario, as in Gran Canaria it is planned to build a reversible hydroelectric plant of 3.2 GWh of capacity and 200 MW [7].

Thereupon, we will proceed to merge both models in order to study a possible mechanism to control the frequency in scenarios of large renewable sources penetration.

### 3 Results and discussion

We will start analysing the frequency data. In first place we draw the frequency pdf:

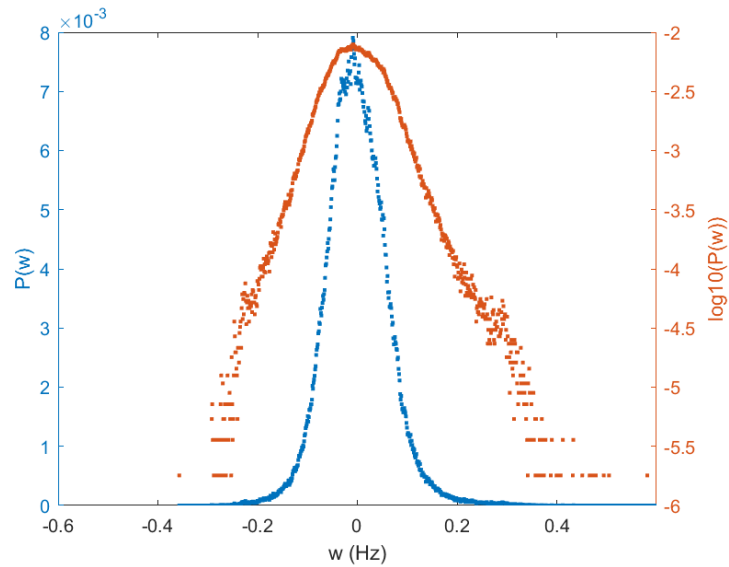


Figure 4: Distribution of the frequency deviation from measurements

As we can observe in Figure 4, the frequency deviation follows a Gaussian distribution around zero. It is important to notice the tail of the distribution, which will be vital in order to evaluate an scenario's stability. Additionally, the standard deviation is 0.062 Hz and the Kurtosis is 5.1414. This means that the tails of the frequency deviation distribution are slightly bigger than the ones in the normal distribution. Furthermore, we know that the deviation is greater than 0.2 Hz only 0.8% of the time and the peak deviation is 0.695 Hz.

The aim of this model imitates a generator that satisfies Gran Canaria's electric demand in 2019, but this generator runs on fossil fuels (it is only valid for conventional energy production). In order to get a model which faithfully represents the production we have to take into account the renewable energies in 2019. In Gran Canaria we only have wind and solar energy, which cannot be regulated like conventional power plants; for every moment the energy produced just depends on the irradiance and the wind. Thus, we will consider the wind and solar power production as immediate demand relief (we can subtract the renewable energy's production from the demand).

Following this analysis, we will configure our model to match the frequency results obtained. We get a good model approximation for  $H = 4(s)$ ,  $P_n = 250 \cdot 10^6(MW)$ ,  $D = 1.5$ ,  $\tau = 0.5(s)$ ,  $P_r = 30 \cdot 10^6(MW)$ ,  $R = 0.05$ ,  $K = 8.5 \cdot 10^6(MW/s)$ . As we have seen in Eq. (9), Eq. (10) and Eq. (11), the  $H$ ,  $D$  and  $P_n$  will affect to how the rotor behaves, the  $\tau$ ,  $P_r$  and  $R$  will condition the primary control and  $k$  will govern the secondary control. With this constants we get the results of Figure 5 and Figure 6: the standard deviation is 0.062 Hz and the Kurtosis is 4.483, in a similar way to the measurements, the tails of our distributions are greater than the ideal ones. In addition, our model only deviates more than 0.2 Hz during only 0.57% of the time and its peak deviation is just 0.48 Hz.

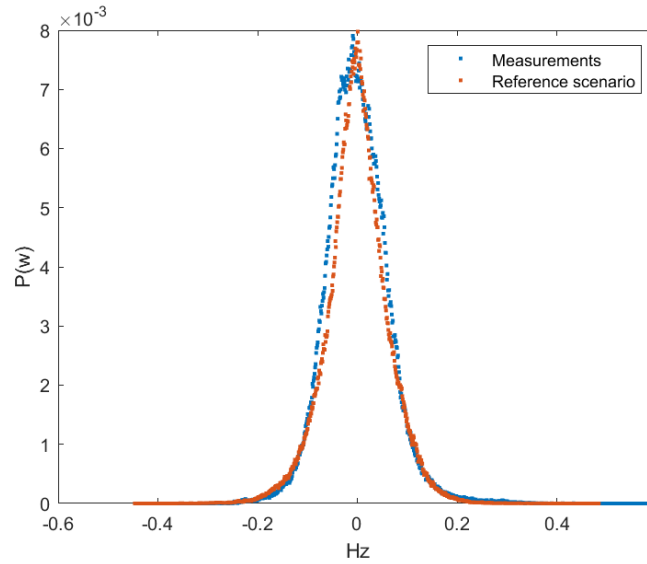


Figure 5: Lineal comparison between measurements and reference scenario

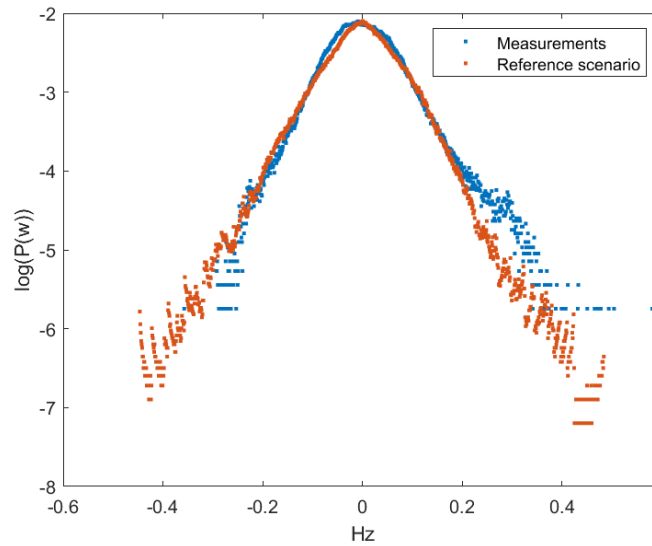


Figure 6: Logarithmic comparison between measurements and reference scenario

From now on, we will take this model as a reference of the actual system in Gran Canaria, and compare it with the different scenarios of penetration of renewable energies in the power grid. First we will start increasing the share of renewable power from 14.47% to 20%, maintaining the rest of the variables constant. As we can observe in Figure 7 and Figure 8, we obtain that the standard deviation is 0.073 Hz and the Kurtosis is 5.206. Moreover, this in scenario the frequency deviates more than 0.2 Hz during 1.62% of the time and its peak deviation is 0.68 Hz.

Although the results with 20% are worse than the original case, it is still a reasonable scenario. We will keep increasing the share of renewable power from 20% to 30%, maintaining the rest of the variables constant. Fromn Figure 7 and Figure 8, we obtain that the standard deviation is 0.098 Hz and the Kurtosis is 6.36. Additionally, our model deviates more than 0.2 Hz during 5.26% of the time and its peak deviation is just 1.05 Hz.

To confirm the trends have already observed, we will further increase the share of renewable power from 30% to 40%, maintaining the rest of the variables constant. As we can see in Figure 7, Figure 8 and Figure 9, we obtain that the standard deviation is 0.126 Hz and the Kurtosis is 7.063. Additionally, our model deviates more than 0.2 Hz during 10.26% of the time and its peak deviation is just 1.42 Hz. We must notice that in this scenario, there is an overproduction of 11.97 GWh (0.128% of Gran Canaria's annual consumption).

There is a clear trend, the more wind and solar generator produce, the more unstable the power grid is. The reason for this phenomena is that renewable energy production is unreliable, it depends on the meteorological conditions, thus a sudden change on the clouds or the wind speed can affect the production. This effects grow in importance as the penetration of wind and solar energies increases. In order to study this tendency we will plot the evolution of the standard deviation, the Kurtosis, the time the deviation surpasses 0.2 Hz with the penetration of renewable energies and the maximum deviation.

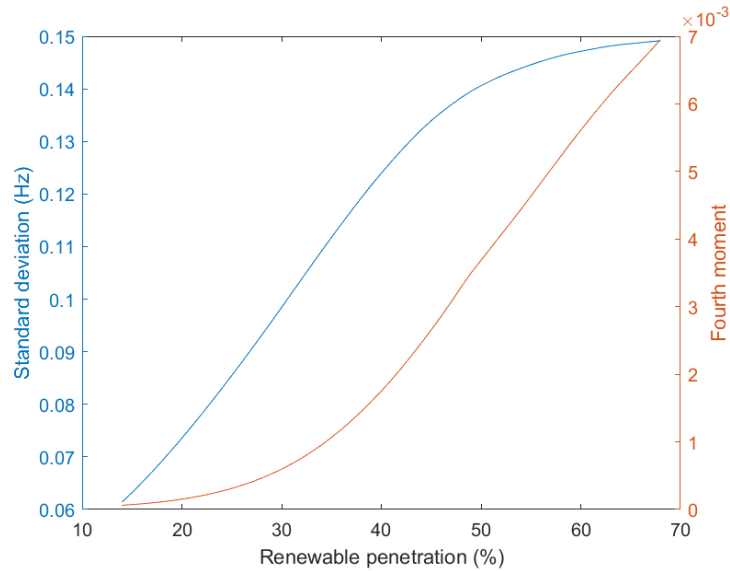


Figure 7: Frequency statistics evolution

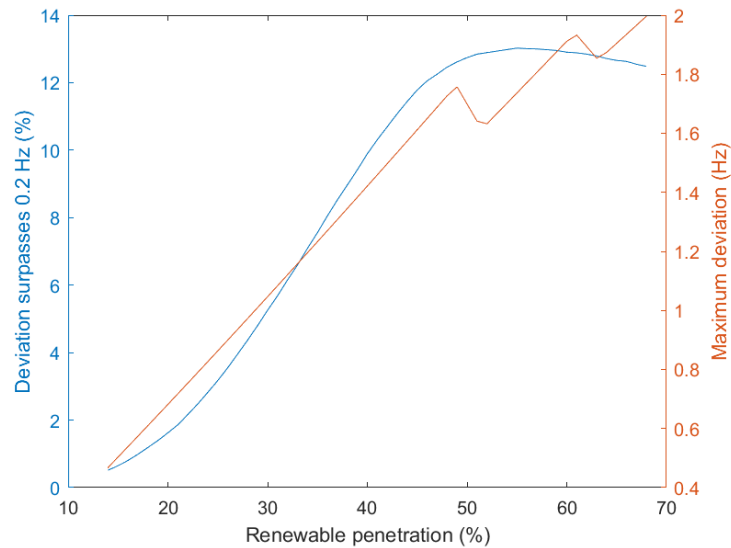


Figure 8: Frequency stability evolution

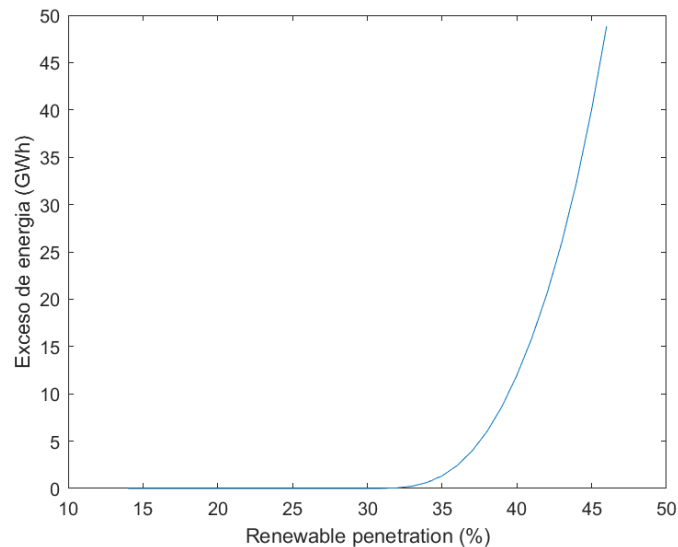


Figure 9: Energy excess due to greater production than demand

Fig. 7, fig. 8 and fig. 9 have been simulated from 14% to 68%, when the renewable energy penetration is higher, the system cannot control the frequency. As we already expected, there is a clear correlation between the percentage of the energy produced from renewable sources and the stability of the power grid. As we have seen, increasing the penetration of wind and solar power without adapting the electrical grid is not sustainable. Furthermore, in all this scenarios we have supposed that the same frequency control was maintained, if there is more renewable energies production, it is logical to have conventional power plants closed, as they will no longer produce energy. Thus, the frequency control (which is carried out in this type of plants) must also decrease. We are going to repeat the previous scenarios but reducing the frequency control proportionally to the increase of renewable energies.

First we will start increasing the share of renewable power from 14.47% to 20%, and reducing the frequency control to a 93,53% of its previous value. As we can observe in Figure 10 and Figure 11, we obtain that the standard deviation is 0.078 Hz and the Kurtosis is 5.195. Moreover, this in scenario the frequency deviates more than 0.2 Hz during 2.19% of the time and its peak deviation is 0.73 Hz.

Although the results with 20% are worse than the original case, it is still a reasonable scenario. We will keep increasing the share of renewable power from 20% to 30%, and reducing the frequency control to a 77.81% of its original value. From Figure 10 and Figure 11, we obtain that the standard deviation is 0.125 Hz and the Kurtosis is 6.326. Additionally, our model deviates more than 0.2 Hz during 10.09% of the time and its peak deviation is just 1.35 Hz. In this scenario the electric grid has an unacceptable frequency control, which could affect to the final users and the devices connected to the grid.

To confirm the trends have already observed, we will further increase the share of renewable power from 30% to 40%, and reducing the frequency control to a 57,45% of its previous value. As we can observe in Figure 10, Figure 11 and Figure 12, we obtain that the standard deviation is 0.216 Hz and the Kurtosis is 7.019. Additionally, our model deviates more than 0.2 Hz during 26.72% of the time and its peak deviation is just 2.53 Hz. We must notice that in this scenario, there is an overproduction of 11.97 GWh (0.128% of Gran Canaria's annual consumption).

Similarly to the previous experiments, there is a clear trend; the more wind and solar generator produce, the more unstable the power grid is. This phenomena combined with a reduction of the electric grid capacity to control frequency leads to an unstable scenario with penetrations greater than 30%. In order to study this tendency we will plot the evolution of the standard deviation, the Kurtosis, the time the deviation surpasses 0.2 Hz with the penetration of renewable energies and the maximum deviation.

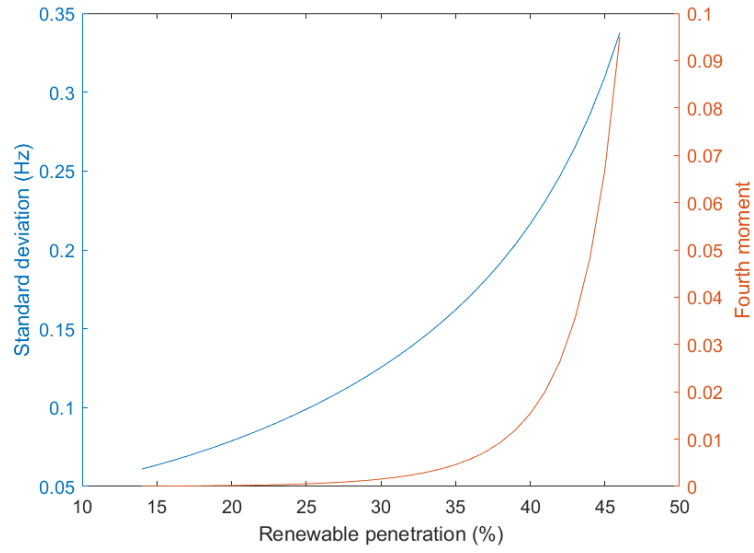


Figure 10: Frequency statistics evolution

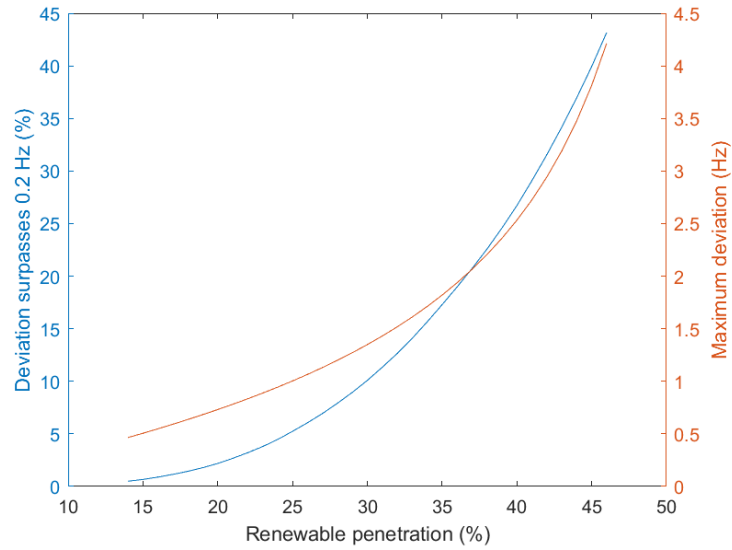


Figure 11: Frequency stability evolution

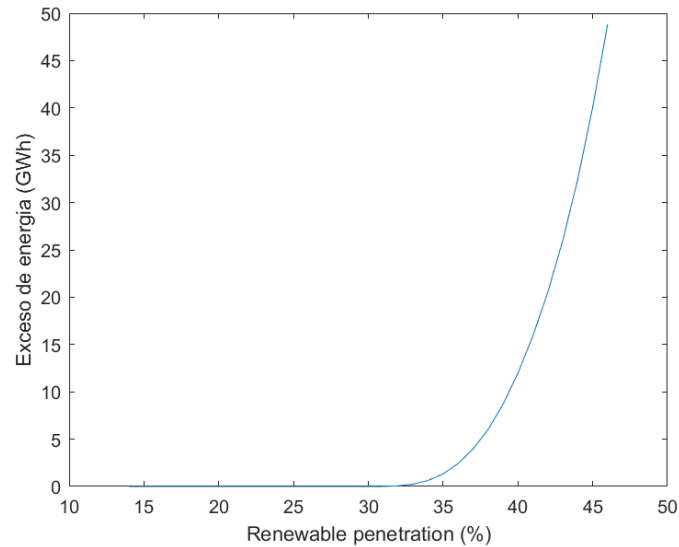


Figure 12: Energy excess due to greater production than demand

In this case, fig. 10, fig. 11 and fig. 12 have been simulated from 14% to 46%, when the renewable energy penetration is higher, the system cannot control the frequency. As expected, the electrical grid capacities from this second experiment are worse than the previous experiment. As we can observe in fig. 1, the share of wind power 13,92 while solar power only produces 1,55% of the total annual energy consumption. This is because in Canary Islands, wind power has much more potential than solar power. In a realistic scenario, the increment of renewable energies will come from wind farms, thus we will repeat the last experiment but increasing only wind power.

First we will start increasing the share of wind power from 13,92% to 18,45%, and reducing the frequency control to a 93,09% of its previous value. As we can observe in Figure 13 and Figure 14, we obtain that the standard deviation is 0.077 Hz and the Kurtosis is 5.124. Moreover, this in scenario the frequency deviates more than 0.2 Hz during 1,93% of the time and its peak deviation is 0.7 Hz.

Although the results with 20% are worse than the original case, it is still a reasonable scenario. We will keep increasing the share of renewable power from 18,45% to 28,45%, and reducing the frequency control to a 77.81% of its original value. From Figure 13, and Figure 14, we obtain that the standard deviation is 0.122 Hz and the Kurtosis is 6.448. Additionally, our model deviates more than 0.2 Hz during 9,46% of the time and its peak deviation is just 1.31 Hz. In this scenario the electric grid has an unacceptable frequency control, which could affect to the final users and the devices connected to the grid.

To confirm the trends have already observed, we will further increase the share of renewable power from 28,45% to 38,45%, and reducing the frequency control to a 54% of its original value. From Figure 13, Figure 14 and Figure 15, we obtain that the standard deviation is 0.167 Hz and the Kurtosis is 7.303. Additionally, our model deviates more than 0.2 Hz during 25.55% of the time and its peak deviation is just 2.49 Hz. We must notice that in this scenario, there is an overproduction of 9.88 GWh (0.1058% of Gran Canaria's annual consumption).

Similarly to the previous experiments, there is a clear trend; the more wind and solar generator produce, the more unstable the power grid is. In this scenarios, the increment was only made in the wind power, we can observe that the results are better when you only enlarge wind power. In order to study this tendency we will plot the evolution of the standard deviation, the Kurtosis, the time the deviation surpasses 0.2 Hz with the penetration of renewable energies and the maximum deviation.

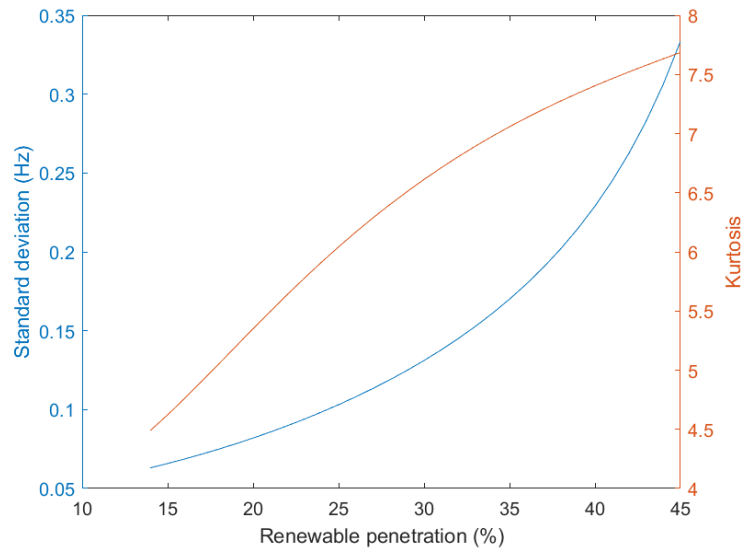


Figure 13: Frequency statistics evolution

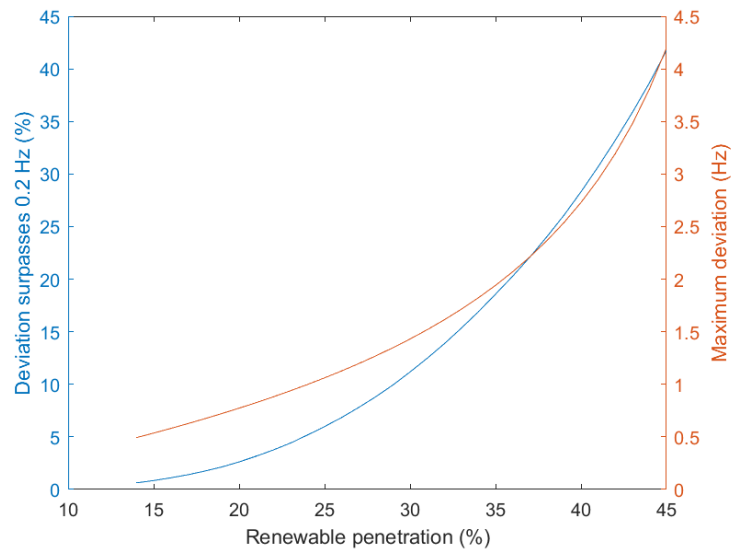


Figure 14: Frequency stability evolution

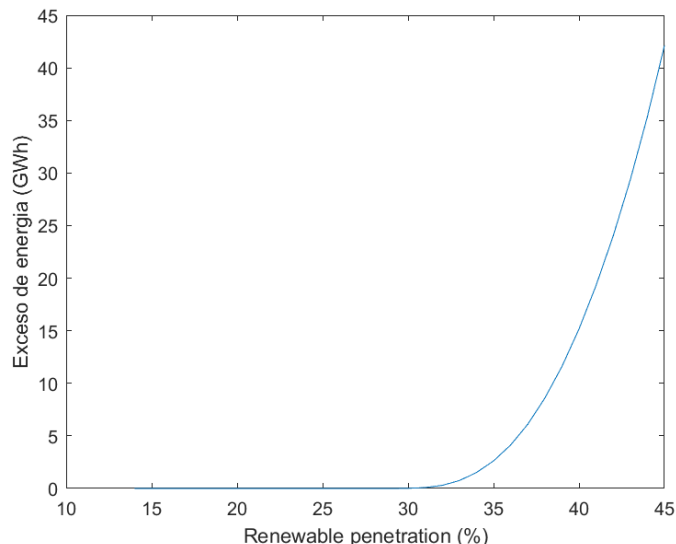


Figure 15: Energy excess due to greater production than demand

After this experiments, we can conclude that it is not possible to just increase the amount of installed wind power. A greater renewable energy penetration in the grid must be accompanied with the appropriate frequency control mechanisms. Consequently we must perform a study of the necessary infrastructures to maintain the quality of the power grid. We will start by analysing the 20% penetration scenario, the most important parameter is the secondary control (governed by the  $k$ ), thus we will change the  $k$  until we get a frequency distribution similar to the one from the measurements. By increasing  $k$  a 15% from its original value we obtain that the standard deviation is 0.0629 Hz (in the real data it is 0.062) and the Kurtosis is 5.184 (measurements is 5.1414). Additionally, our model deviates more than 0.2 Hz during 0.78% of the time and its peak deviation is just 0.57 Hz.

Now we will analyse the 30% penetration scenario, by increasing  $k$  a 60% from its original value we obtain that the standard deviation is 0.0621 Hz (in the real data it is 0.062) and the Kurtosis is 6.6167 (measurements is 5.1414). Additionally, our model deviates more than 0.2 Hz during 0.95% of the time and its peak deviation is just 0.64 Hz.

Finally we will increase to the 40% penetration scenario, by increasing  $k$  a 105% from its original value we obtain that the standard deviation is 0.0632 Hz (in the real data it is 0.062) and the Kurtosis is 7.4612 (measurements is 5.1414). Additionally, our model deviates more than 0.2 Hz during 1.13% of the time and its peak deviation is just 0.67 Hz. In this scenario we have an overproduction of 9.88 GWh (0.1058% of Gran Canaria's annual consumption).

These results confirm the need for additional frequency control mechanism when increasing the renewable penetration. Following the results of the last experiments, an greater presence of wind power will actually mean having to install additional conventional plants in order to regulate the power grid. This result is counter-intuitive, as the objective of having more renewable energies is to eradicate the conventional sources. This dilemma can be avoided using energy storage methods, which are having a great development and advances in the last few years.

The objective of energy storage is to compensate for the uncertainty and variability of renewable energies. Thus, the battery should only operate when a sudden fluctuation takes place. In addition to the battery model already described, we will impose a condition: The battery will only operate when the frequency deviation is positive or the frequency deviation is less than  $-0.1\text{Hz}$ .

On the one hand, if the frequency deviation is positive, it means that there is more production than demand, in this case we can use this spare energy to charge the batteries. On the other hand, if the frequency deviation surpasses  $-0.1\text{Hz}$ , it means that there has been a rapid change in the demand or in the production which endangers the electric grid stability. Thus, the battery start delivering power until it discharges or the frequency is compensated over that  $-0.1\text{Hz}$  limit. In the following section we will proceed to dimension and analyse the effects of energy storage in the power grid.

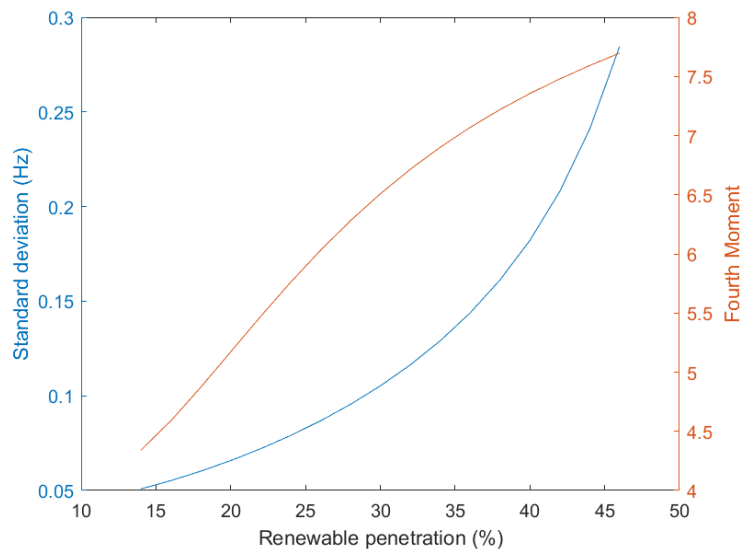


Figure 16: Frequency statistics evolution

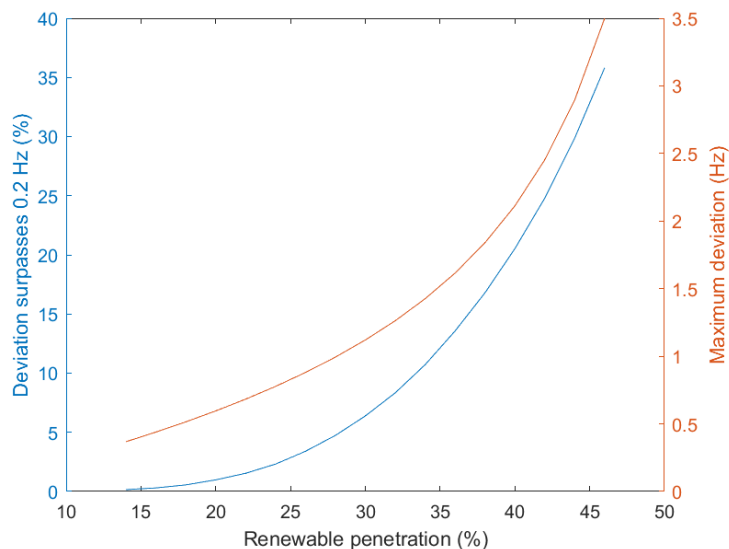


Figure 17: Frequency stability evolution

In fig. 16 and fig. 17 we can observe that the frequency control is excellent, the resulting scenario is better than all previous ones. Both the statistic and the stability evolution show that the electric grid be perfectly managed through energy storage.

This battery allows to perform frequency control until around a 30% of renewable energy penetration. In the future, it would be interesting to expand the capacity of the batteries in order to support greater renewable penetration, this way we will repeat the experiment having ten times more capacity (5.3GWh).

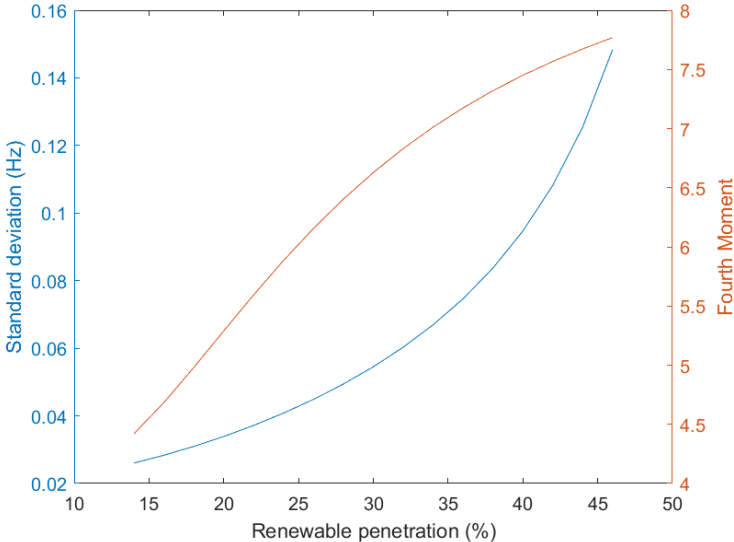


Figure 18: Frequency statistics evolution

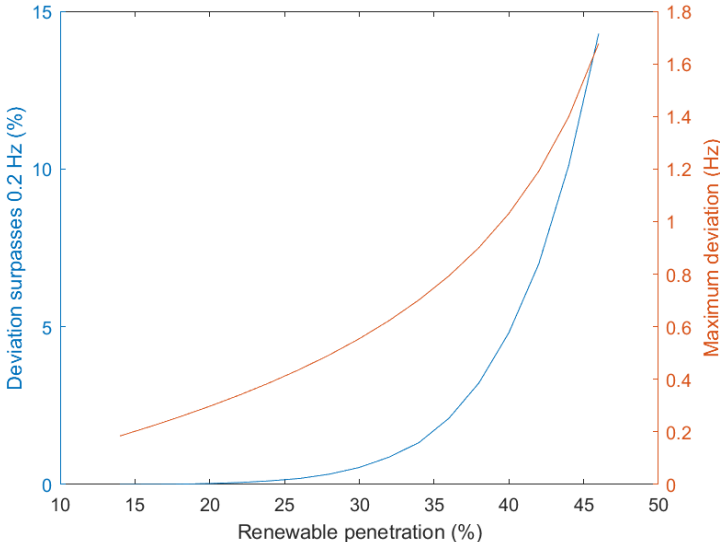


Figure 19: Frequency stability evolution

As seen in Figure 18 and Figure 19, this battery allows to perform frequency control until around a 40% of renewable energy penetration. In order to perform a more complete study, we will duplicate the capacity of the batteries, consequently we will repeat the experiment having 10.6GWh.

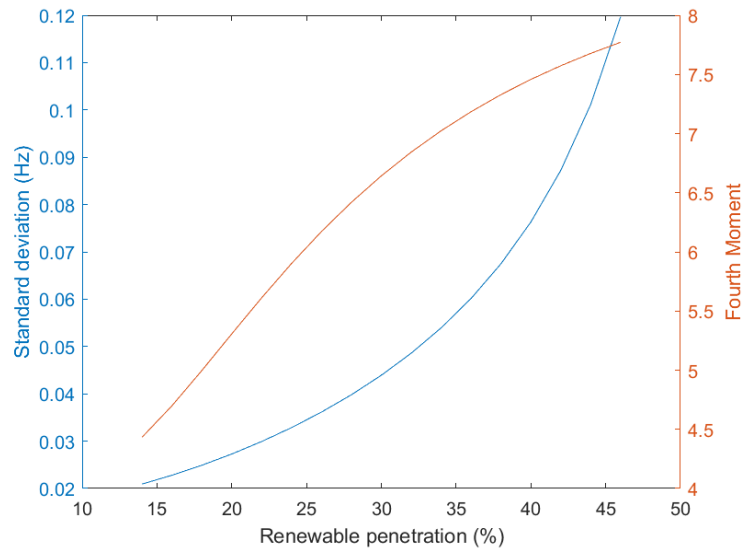


Figure 20: Frequency statistics evolution

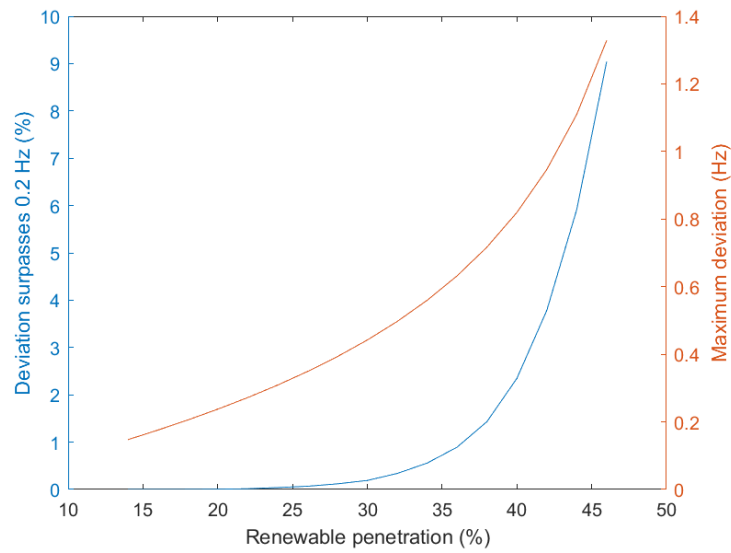


Figure 21: Frequency stability evolution

With fig. 20 and fig. 21 we can conclude that even with enormous penetration ratios, we could guarantee the quality of the power grid to the users.

## 4 Conclusions

We have analyzed different scenarios of renewable energy penetration and we have observed the effects it has on the electric grid. We have measured the reliability of all the scenarios, studying numerous solutions for adapting the power grid to a higher penetration of clean energies.

Finally, the only realistic and coherent ways the power grid could adapt, are either installing more power than needed or having batteries for regulating frequency. On the one hand, having excessive installed power would allow to match the production to the demand by throwing away energy, but it would have a great economic and environmental impact. On the other hand, building batteries for frequency regulation would allow to have a stable and reliable power grid even in large renewable energies penetration scenario.

Considering the high impact that wind farms have and the rapid growth of batteries technologies, the best solution for enlarging the share of clean energies is the use of batteries to regulate frequency. Of course, the implementation of this measures to adapt the electric grid, would be carried out by the REE (Red Eléctrica Española) which is the responsible to ensure the stability of the power grid.

In order to reduce the production of greenhouse effect gases, our society must transition from conventional fuels to clean sources of energies. This will translate into a greater share of renewable energies in the power grid, causing fluctuations and instability. Thus, the REE must ensure its stability by adapting the power grid, this will have a great cost. When discussing renewable sources of energy, it is vital to consider an additional cost; the price of frequency control.

Although developing a clean power grid is essential for our future, all the politics regarding the installation of renewable sources of energy must include measures to increment frequency control. Batteries for frequency control will be the core of the energetic transition in our society.

## Acknowledgments

This paper has been possible thanks to my supervisors Prof. Pere Colet and Dr. Damià Gomila. Thank you for your patience, availability and guidance through the project. I would also like to thank IFISC and its staff for the SURF summer programs which has made possible this paper.

## References

- [1] [https://ec.europa.eu/clima/policies/strategies/2030\\_es](https://ec.europa.eu/clima/policies/strategies/2030_es)
- [2] <https://ieefa.org/spanish-government-approves-strategy-to-double-energy-storage-capacity-by-2030>
- [3] <https://www.ree.es/es/datos/generacion>
- [4] <https://www.ree.es/es/datos/mercados>
- [5] <https://www.energiagrancanaria.com/wp-content/uploads/2020/10/anuarioelectricocanarias2019-pub.pdf>
- [6] <https://www.miteco.gob.es/es/prensa/pniec.asp3>
- [7] [https://www.ree.es/sites/default/files/downloadable/folleto\\_soria\\_chira.pdf](https://www.ree.es/sites/default/files/downloadable/folleto_soria_chira.pdf)

# Game theory and the evolution of cancer

Bernat Ramis

supervised by Tobias Galla

Instituto de Física Interdisciplinar y Sistemas Complejos, IFISC (CSIC-UIB)  
Campus Universitat de les Illes Balears, E-07122 Palma de Mallorca, Spain

## Abstract

This project aims to use evolutionary game theory to develop a model based on Moran processes for two different kinds of individuals competing for reproduction and survival. Our model takes into account the different fitnesses of species, mutation and ageing. We implemented the model with stochastic simulations in order to draw conclusions. As an application, it can model the evolution of a community of cancer cells.

## 1 Introduction

This introduction to evolutionary game theory is inspired by [1].

### 1.1 Game theory: Prisoner's dilemma and its variations

In game theory, one studies situations involving a number of individuals whose decisions or strategies affect the whole community. The canonical example is the *prisoner's dilemma*.

Concerning our interest, imagine a system consisting of two kinds of individuals that interact (e.g. for survival or reproduction). So-called A individuals adopt a certain strategy while B individuals behave according to other rules. This interaction may be modeled using "rewards" or "costs", which depend on which strategies encounter. For two different strategies, we have four possible situations, as depicted in Tab. 1.

	<b>A</b>	<b>B</b>
<b>A</b>	R	S
<b>B</b>	T	P

Table 1: Payoff matrix. R, S, T and P (standing for Reward, Sucker's payoff, Temptation and Punishment, respectively, as in the *prisoner's dilemma*) represent real positive numbers, which are the payoffs for the player on the leftmost column when an encounter of strategies takes place. The uppermost row collects the possible strategies of the opponent. For instance, a B individual battling against an A individual would be rewarded an amount of T.

Here, the concept of Nash equilibrium arises.

**Definition 1.1.** A set of strategies for some given players is called to be a **Nash equilibrium** if any change in the strategy of any player would not improve their chances of beating the others. These configurations fully depend on the values of R, S, T and P.

### 1.2 First-order ODE approach

**Definition 1.2.** According to Tab. 1, the **fitness** of a given strategy (say strategy A) is defined as follows:

$$\pi_A(a) := 1 + Ra + Sb = 1 + Ra + S(1 - a) \tag{1}$$

where  $a := N_A/N$  is the fraction of individuals of kind A present in the whole population considered. Here, we used that only two strategies are possible (A and B), thus  $b = 1 - a$ .

**Observation 1.1.** The additive term 1 present in the formula is the background fitness, and it is mainly added so that the fitness is strictly positive, which is required in later definitions. The remaining terms are the average payoff expected when playing the game (performing strategy A, in the case considered in Eq. (1)).

**Definition 1.3. Average fitness:**

$$\bar{\pi}(a) := a\pi_A(a) + b\pi_B(b) = a\pi_A(a) + (1-a)\pi_B(a) \quad (2)$$

This magnitude is useful to measure the mean gain of an individual in a community where different strategies coexist.

We finally get to the first-order ODEs.

**Definition 1.4. Standard replicator equation**

$$\partial_t a = [\pi_A(a) - \bar{\pi}(a)]a \quad (3)$$

**Definition 1.5. Adjusted replicator equation**

$$\partial_t a = \frac{\pi_A(a) - \bar{\pi}(a)}{\bar{\pi}(a)} a \quad (4)$$

Both of the above presented equations tell that the population of A individuals will grow proportionally to the actual amount of A individuals and proportionally to the difference between the fitness of A and the mean fitness. Notice that if the fitness of A is larger than the mean fitness, then the population of A will increase (since, in average, they tend to win more often). Likewise, if the fitness of A is lower than the mean fitness, the population of A will decrease. The previous equations can analogously describe the evolution of the fraction of individuals of other strategies (strategy B with a fraction of individuals  $b$ ).

Eq. (3) can be rewritten as

$$\partial_t a = a(1-a)[\mu_A(1-a) + \mu_B a] =: F(a) \quad (5)$$

where  $\mu_A := S - P$  and  $\mu_B := T - R$  are the relative benefits of A playing against B and B playing against A, respectively. Now the relative payoff matrix looks like in Tab. 2.

	<b>A</b>	<b>B</b>
<b>A</b>	0	$\mu_A$
<b>B</b>	$\mu_B$	0

Table 2: Relative payoff matrix. Only relative payoffs are relevant (difference of gains for each encounter).

The values of the control parameters  $\mu_A$  and  $\mu_B$  make possible a classification into four kinds of games:

Game	control parameters	stable fixed points
Prisoner's dilemma	$\mu_A < 0$ $\mu_B > 0$	$a = 0$
Snowdrift/Coexistence	$\mu_A > 0$ $\mu_B > 0$	$a = \frac{\mu_A}{\mu_A + \mu_B}$
Coordination	$\mu_A < 0$ $\mu_B < 0$	$a = 0, 1$
Harmony	$\mu_A > 0$ $\mu_B < 0$	$a = 1$

Table 3: Game classification using the criterion of the relative benefits  $\mu_A$  and  $\mu_B$ . For the fixed points, recall that it is needed that  $F(a) = 0$  in Eq. (5). Moreover, for a fixed point to be stable, it is sufficient that  $F'(a) < 0$ , because if  $F(a) = 0$  then  $F(a+h) < 0$  for small  $h > 0$  so this means that  $\partial_t a < 0$  and thus  $a+h$  decreases to  $a$ , meaning there is an attraction towards  $a$  (attraction is also concluded assuming  $h < 0$ ). Accordingly, stable fixed points for each set of control parameters can be analytically derived. The names of the games describe the location of the stable fixed points. For example, in a Coordination game, stability arises when all players in the community carry out the same strategy (either A or B).

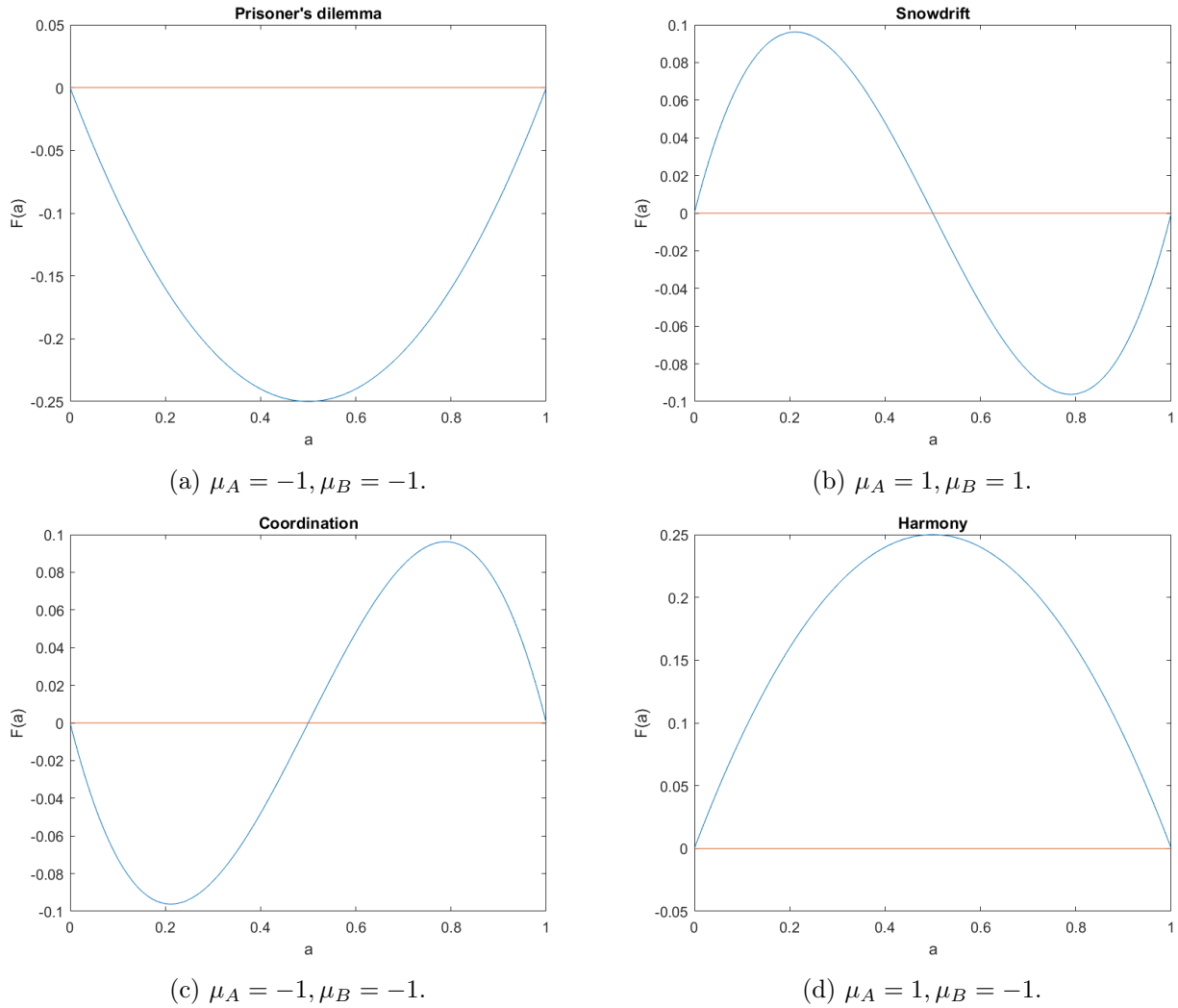


Figure 1: Plots of  $F(a)$  in Eq. (5) split by different cases for different control parameters  $\mu_A$  and  $\mu_B$ . Stable fixed points can be found identifying the values of  $a$  such that  $F(a) = 0$  and  $F'(a) < 0$ . Points for which  $F(a) = 0$  and  $F'(a) > 0$  are unstable fixed points.

For the fixed points, recall that it is needed that  $F(a) = 0$  in Eq. (5). Moreover, for a fixed point to be stable, it is sufficient that  $F'(a) < 0$ , because if  $F(a) = 0$  then  $F(a + h) < 0$  for small  $h > 0$  so this means that  $\partial_t a < 0$  and thus  $a + h$  decreases to  $a$ , meaning there is an attraction towards  $a$  (attraction is also concluded assuming  $h < 0$ ).

The plots in Fig. 1 are perfectly coherent with the above classification: one can detect a stable fixed point in a plot by identifying the points where  $F(a) = 0$  and  $F'(a) < 0$ . In this case, it is often referred to as Nash equilibrium points. Besides, points such that  $F(a) = 0$  and  $F'(a) > 0$  are unstable fixed points.

We would like this theory about the payoff matrix to underlie the model that we develop for confrontation between two different strategies.

## 2 Individual based model

### 2.1 Moran processes

Consider two kinds of individuals, A and B. We use  $N_A$  and  $N_B$  to denote the number of individuals of the type they are labelled.

**Definition 2.1.** A **Moran process** is a stochastic process for modelling populations of a finite number of individuals, each belonging to type A or B. To carry the process out, at each time step two individuals are chosen at random among the available population. Then, according to certain probabilities, which depend on the fitnesses of the selected individuals, maybe one of them is chosen

to die and the remaining one replicates, or maybe nothing happens. Overall, if we focus just on the number of individuals of each type, one of the following transitions may occur at each time step:

- $(N_A, N_B) \rightarrow (N_A + 1, N_B - 1)$
- $(N_A, N_B) \rightarrow (N_A - 1, N_B + 1)$
- $(N_A, N_B) \rightarrow (N_A, N_B)$

Observe that  $N_A + N_B = N$  is constant during the process. It is useful to introduce a variable  $i$  that counts the number of A individuals  $N_A$  present in the system at any time, as in Fig. 2.  $T_i^+$  and  $T_i^-$  denote the probabilities of transition of number of A individuals. Also take into account that these probabilities for each transition at each time step can be different (usually, these probabilities depend on  $i$ ).

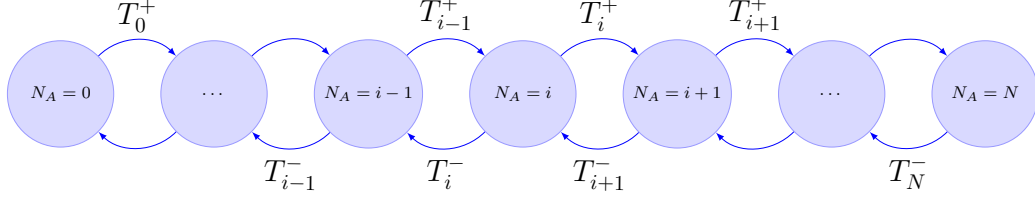


Figure 2: Diagram of a Moran process. At each time step, the  $i$  variable (which takes the value of the number of A individuals present in the community in that moment) may increase or decrease its value by 1, meaning that a new A individual replaced a B individual or vice versa. The probabilities for this to happen, which depend precisely on  $i$ , are denoted as  $T_i^+$  for increasing  $i$  transitions and  $T_i^-$  for decreasing  $i$  transitions. It always holds that  $T_i^+ + T_i^- \leq 1$  for  $i = 1, \dots, N$ .

In Moran processes, fixation times are an interesting magnitude to study.

**Definition 2.2. Unconditional fixation time:** expected time elapsed starting with 1 individual of kind A and ending up with only one kind of individuals (either A or B).

**Definition 2.3. Conditional fixation time (for A individuals):** expected time elapsed starting with 1 individual of kind A and ending up with only A individuals.

Fixation time analytical expressions may be derived from recurrences, see [2]. In an attempt to study them with simulations, the results look like in Fig. 3.

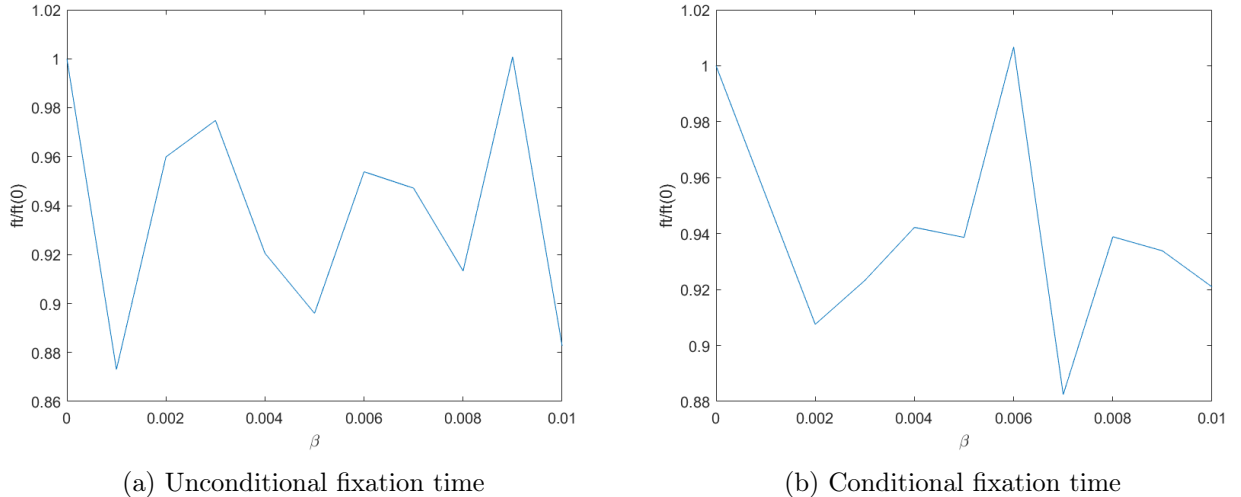


Figure 3: Relative fixation time  $\frac{\text{fixation time}(\beta)}{\text{fixation time}(\beta=0)}$  as a function of the fitness importance parameter  $\beta$ . Parameters chosen are  $N = 10$ ,  $M = \begin{pmatrix} 5 & 2 \\ 3 & 1 \end{pmatrix}$  and initially  $N_A = 1$ . Only 500 samples for each averaged  $\beta$  value. Since the variance of the fixation time is huge, we get nothing close to linear plots.

Theory says that for small  $\beta$ , one can get decent linear approximations for fixation times as a function of  $\beta$ . However, this is not what Fig. 3 depicts. In order to fix this issue, we need a set of

the order of  $10^7$  samples to reduce the effect of the variance in fixation times, which is large. For less samples, the results are more like in Fig. 3.

As Fig. 4 and Fig. 5 show, outputs from simulations follow the theoretical results obtained in [2].

At least for  $0 < \beta < 0.01$  the linear approximation is valid. Observe that according to the  $M$  payoff matrices, Fig. 4 stems from a drag game whereas Fig. 5 comes from a coordination game.

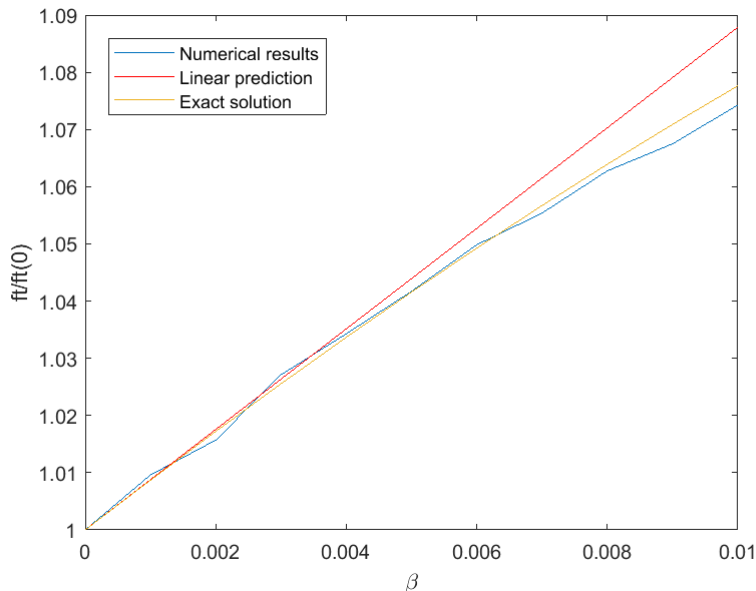


Figure 4: Relative unconditional fixation time  $\frac{\text{fixation time}(\beta)}{\text{fixation time}(\beta=0)}$  as a function of the fitness importance parameter  $\beta$  (see Eq. (15)). Parameters chosen are  $N = 100$ ,  $M = \begin{pmatrix} 5 & 2 \\ 3 & 1 \end{pmatrix}$  and initially  $N_A = 1$ .  $10^7$  samples taken. Now the averaged fixation times obtained from simulations do follow the theoretical results, as well as they both graze the linear prediction.

## 2.2 Evolutionary games with ageing

We will now consider a population of agents interacting in an evolutionary game, but subject to ageing. By this we mean a setup in which the success or otherwise of an agent depends on their "age", that is the time since they were born.

To this end we consider a population of  $N$  agents, who can each be of type A or type B. We write  $N_A$  for the number of agents of type A, the number of agents of type B is then  $N - N_A$ . Each of the agents has an age  $\tau_i$ , where  $i = 1, \dots, N$  labels the agents.

We choose a discrete-time setup for convenience (but can also generalise to continuous time later). The model proceeds as follows:

1. Time  $t = 0$ . Initialise the population. All agents have age zero ( $\tau_i \equiv 0 \forall i$ ). The initial number of agents of type A is set to  $N_A = N_{A,0}$ .
2. At each step of the simulation pick two distinct agents  $i$  and  $j$  ( $i \neq j$ ). Let  $\pi^{(i)}$  and  $\pi^{(j)}$  be their fitnesses.  $\pi^{(i)}$  will only depend on what type agent  $i$  is of (A or B) and on the composition of the population, i.e. the number  $N_A$  of agents of type A. For example, if  $i$  is of type A, then  $\pi^{(i)} = \pi_A(N_A)$ .
3. We now need to decide if agent  $i$  reproduces (and  $j$  dies) or vice versa. We do this with the following probabilities:

$$\begin{aligned} i \text{ reproduces with probability } p_i &= g(\pi_i - \pi_j) \times h(\tau_i, \tau_j), \\ j \text{ reproduces with probability } p_j &= g(\pi_j - \pi_i) \times h(\tau_j, \tau_i). \end{aligned} \quad (6)$$

4. Once decided what agent reproduces (if any does), kill the other one. The reproducing agent reproduces. With probability  $1 - \mu$  the offspring will be of the same type (A or B) as

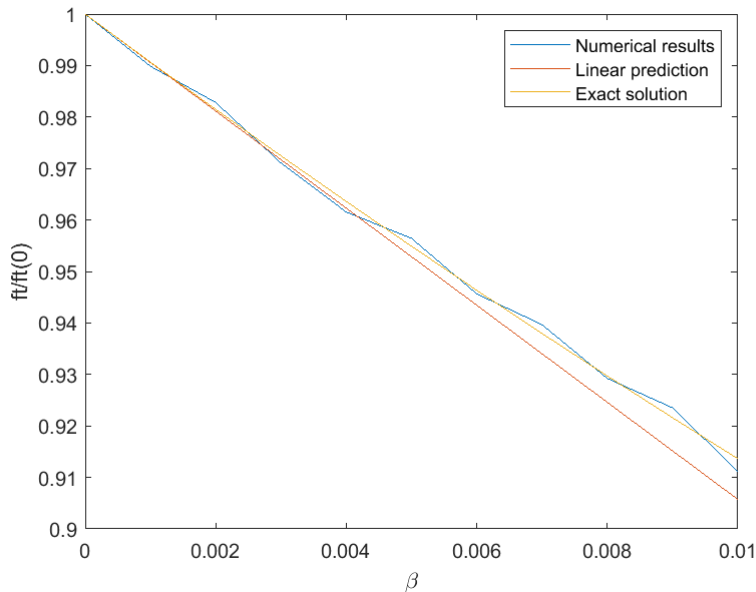


Figure 5: Relative unconditional fixation time  $\frac{\text{fixation time}(\beta)}{\text{fixation time}(\beta=0)}$  as a function of the fitness importance parameter  $\beta$ . Parameters chosen are  $N = 100$ ,  $M = \begin{pmatrix} 5 & 1 \\ 3 & 2 \end{pmatrix}$  and initially  $N_A = 1$ .  $10^7$  samples taken. Once again, numerical results agree with theoretical expressions.

the reproducing agent, i.e., no mutation occurs. With probability  $\mu$  a mutation occurs, the offspring is of the opposite type as the parent. The age of the offspring is set to zero.

5. The ages of all agents increase by  $\Delta t$  (the length of the time step), and overall time is also incremented by  $\Delta t$ . Then go to step 2.

#### Choice of time step:

The natural choice for the time step is  $\Delta t = 1/N$ . This means that order  $N$  events happen per unit time, so each agent is picked order one times per unit time.

#### Further remarks:

- The function  $g(\cdot)$  describes selection based on fitness difference. This could be chosen as the Fermi function

$$g(\Delta\pi) = \frac{1}{1 + e^{-\beta\Delta\pi}}, \quad (7)$$

but other choices are possible as well. Note that  $g(\cdot)$  needs to be an increasing function of  $\Delta\pi$ . The parameter  $\beta$  characterises the intensity of selection.

- We also need to decide how the ages of the agents affect the process. This is what the function  $h(\cdot, \cdot)$  does. There are several simple choices:
  - Age only affects the probability to reproduce,  $h(\tau_i, \tau_j) = h(\tau_i)$ .
  - Age only affects the probability to die,  $h(\tau_i, \tau_j) = h(\tau_j)$ .
  - Only age difference matters,  $h(\tau_i, \tau_j) = h(\tau_i - \tau_j)$ .

In each of these cases the resulting function  $h(x)$  can be increasing or decreasing (depending on whether young individuals should have advantage over old ones or the other way around) and could take different shapes (e.g. exponential, power law, etc.).

## 2.3 Comparison of fixation times

In order to study how ageing affects fixation times compared with the lack of ageing case, it would not be fair to multiply the probability to reproduce  $g(\cdot)$  by the new ageing probability function  $h(\cdot)$ , because in such a case the probability for nothing to happen would be increased and thus the process slows down, in the sense that more rounds without anything happening occur.

If an A individual meets a B individual, let  $p^+$  be the probability that the A participant replicates substituting the B one, and let  $p^-$  be the vice versa probability. Coherently,  $p^+ + p^- \leq 1$ . An

alternative we propose is defining two coefficients  $\alpha = \alpha(\tau)$  and  $\beta = \beta(\tau)$  that reward or punish the probabilities  $p^+$  and  $p^-$  according to the age of the fighters chosen, keeping the probability for nothing to happen unchanged:

$$\begin{aligned} p^+ + p^- &=: s \\ \alpha p^+ + \beta p^- &= s \end{aligned} \quad (8)$$

Now defining the ratio  $r := \frac{\alpha}{\beta}$  and manipulating Eq. (8),

$$r = \frac{\alpha}{\beta} = \frac{\frac{s}{\beta} - p^-}{p^+} \implies \beta = \frac{s}{rp^+ + p^-}. \quad (9)$$

At this point, we may choose the ratio  $r$ . Then,  $\alpha$  and  $\beta$  become uniquely determined. Here, although many possibilities arise, we wish that:

- $r \in [\frac{1}{2}, 2]$  so that the weights  $\alpha$  and  $\beta$  are not extremely unbalanced.
- $r$  should depend on the age of the pair of individuals considered. Let  $r\left(\frac{\tau_i}{\tau_j}\right)$  depend on the ratio of ages,  $R := \frac{\tau_i}{\tau_j}$ .
- It is reasonable to ask that  $r\left(\frac{1}{R}\right) = \frac{1}{r(R)}$ , for all  $R$ . This way,  $r$  (or  $\frac{1}{r}$ ) does not depend on the order of the ages of the pair of individuals (up to inverse).
- Consequently, it is natural to require that  $r(1) = 1$  and  $r(0) = \frac{1}{2} \equiv r(\infty) = 2$ .

**Observation 2.1.** Functions of the kind

$$r(R) = \frac{\sum_{i=0}^k d_i R^i}{\sum_{i=0}^k d_{k-i} R^i} \quad (10)$$

with  $k \in \mathbb{N}$  and  $d_i \in \mathbb{R}$  for  $i = 1, \dots, k$ , solve the functional equation  $r\left(\frac{1}{R}\right) = \frac{1}{r(R)}$ .

For simplicity, we choose

$$r(R) = \frac{AR + B}{BR + A} = \frac{R + \gamma}{\gamma R + 1} \quad (11)$$

with  $\gamma := \frac{B}{A}$ , which is determined imposing the point conditions. It is already fulfilled that  $r(1) = 1$ . Now,  $r(0) = \gamma = \frac{1}{2}$ , so we end up with

$$r(R) = \frac{2R + 1}{R + 2}. \quad (12)$$

**Observation 2.2.** The greater  $N$ , the greater the lifetimes  $\tau_i$  of the individuals tend to be. However, since the ratios  $R := \frac{\tau_i}{\tau_j}$  are the variables, it is not needed to take into account an  $N$  dependency in the function  $r(R)$ .

To sum up, including ageing in the model the way proposed implies updating the probabilities  $p^+$  and  $p^-$  as follows:

- $p^+ \rightarrow \alpha p^+$
- $p^- \rightarrow \beta p^-$

where  $r(R)$  is Eq. (12),  $\beta$  is Eq. (9) and  $\alpha = r(R)\beta$ .

## 2.4 Deterministic equations

We derive equations for the designed model, inspired by [3].

- $x$ : fraction of A individuals
- $x_i^+$ : fraction of A individuals and age  $i$
- $x_i^-$ : fraction of B individuals and age  $i$
- $p_d^+(i)$ : probability that an A individual of age  $i$  dies
- $p_d^-(i)$ : probability that a B individual of age  $i$  dies
- $s^{-\rightarrow+}(i)$ : probability to switch from B and age  $i$  to A and age 0 (without mutating)
- $s^{+\rightarrow-}(i)$ : probability to switch from A and age  $i$  to B and age 0 (without mutating)

$$\begin{cases} \frac{dx_i^+}{dt} = -x_i^+ + x_{i-1}^+(1 - p_d^+(i-1)) \\ \frac{dx_i^-}{dt} = -x_i^- + x_{i-1}^-(1 - p_d^-(i-1)) \\ \frac{dx}{dt} = \sum_{i=0}^{\infty} x_i^- s^{-\rightarrow+}(i) - \sum_{i=0}^{\infty} x_i^+ s^{+\rightarrow-}(i) \end{cases} \quad (13)$$

To include ageing in the infinite system of equations, it is required to take ageing into account in  $p_d^+(i)$ ,  $p_d^-(i)$ ,  $s^{-\rightarrow+}(i)$  and  $s^{+\rightarrow-}(i)$ , as follows.

$$\begin{aligned} p_d^\pm(i) &= \frac{\sum_j p_d(i|\text{opponent's age is } j)x_j^\pm}{\sum_j x_j^\pm} \\ s^{-\rightarrow+}(i) &= p_d^-(i)(1 - \mu) \\ s^{+\rightarrow-}(i) &= p_d^+(i)(1 - \mu) \end{aligned} \quad (14)$$

$\mu$  is the probability of mutation.

### 3 Results and discussion from simulations

#### 3.1 Lifetime distribution for Moran processes

Now the question to be answered is, in an ageingless Moran process, what does the distribution of individual lifetimes look like? To dive into the context, imagine a population of individuals of kinds A and B, together with a certain payoff matrix  $M$  that induces a set of probabilities for the individuals to die or reproduce. If one focuses on a specific individual, say of kind A, how long is it expected to live and what is the probability distribution behind?

Hereinafter, the choices for the setup are the following.

- Consider the distribution of deaths for a kind A individual.
- Fermi distribution of probability of death for direct encounters:

$$p_-(\Delta\pi) = \frac{1}{1 + e^{-\beta\Delta\pi}}. \quad (15)$$

- Coexistence payoff matrix, in particular  $M = \begin{pmatrix} 3 & 2 \\ 5 & 1 \end{pmatrix}$ .
- Probability of mutation of 5%. Mutation will prevent the system from fixation.
- Initial conditions with one only individual of kind A.
- The number of individuals  $N$  and the parameter  $\beta$  remain free for later exploration.
- Lifetime is computed as the number of rounds that an individual survives since it was born.

We now compute of the probability that a given individual dies. Firstly, the individual has to be chosen, event that takes place with probability  $1/N$ . Afterwards, the second competitor can either be of kind A or B. An A would be picked with probability  $\frac{i-1}{N-1}$ . If two A's compete, the probability of losing is 0.5 according to the Fermi distribution, Eq. (15).

If instead of being A, the second individual were B, which would happen with probability  $\frac{N-i}{N-1}$ , then the given individual would die with probability  $p^-(i)$ .

Finally, since the pair of individuals can be chosen in two different orders, a factor 2 is introduced, leading to

$$p_d(i) := p_{death}(i) = \frac{1}{N(N-1)}(i-1 + 2(N-i)p_-(i)). \quad (16)$$

Imagine for a moment that  $p_d(i)$  was constant on the number of A individuals  $i$ . Then, the distribution for the lifetime random variable  $LT$  would be geometric of parameter  $p_d$ ,  $LT \sim \text{Geom}(p_d)$ , i.e.

$$p(LT = t) = (1 - p_d)^t p_d, \quad t = 0, 1, 2, \dots \quad (17)$$

where  $t$  is the number of rounds survived.

In general,  $p_d(i)$  will not be constant, so in principle Eq. (17) does not necessarily work. It will if the fluctuations of  $p_d(i)$  with time are little, although for large fluctuations the distribution may be deformed to an extent that it is no longer geometric. The work now is to study this by varying  $\beta$  and  $N$  in the simulations. As a start, let  $N = 100$  and focus on the order of magnitude of  $\beta$ .

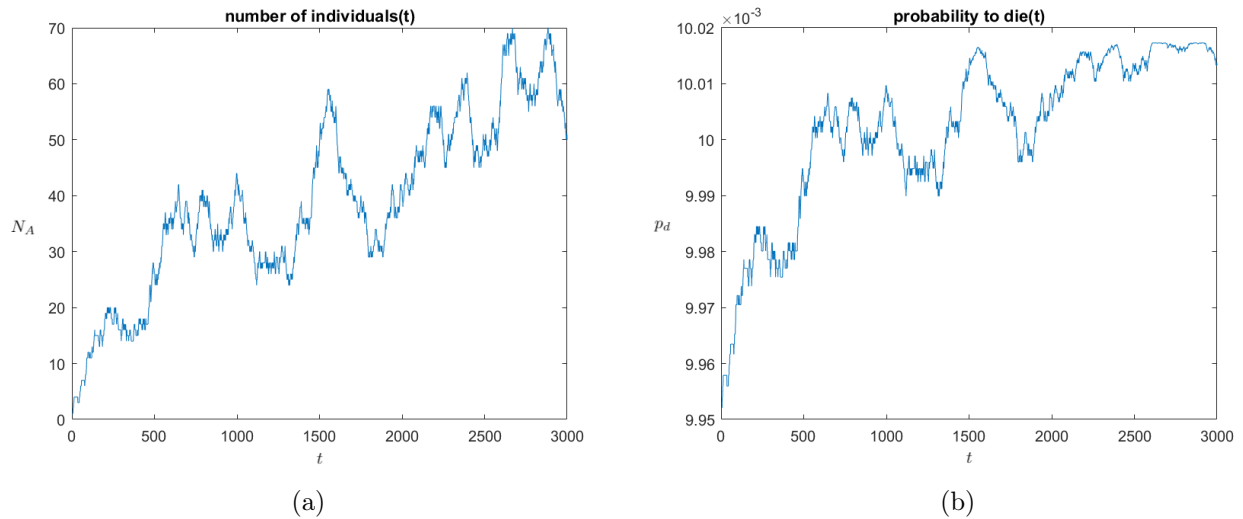


Figure 6: Number of A individuals  $N_A$  and probability of an A individual to die  $p_d$  as a function of time  $t$ , from a stochastic simulation with parameters  $N = 100$ ,  $N_{A,0} = 1$ ,  $10^5$  lifetime samples taken, probability of mutation  $\mu = 5\%$ ,  $M = \begin{pmatrix} 3 & 2 \\ 5 & 1 \end{pmatrix}$  and  $\beta = 0.01$ . Both magnitudes tend to oscillate around their equilibrium values, given by the equilibrium  $N_A$ , which at the same time is determined by the payoff matrix  $M$ . This is a case of so-called weak selection, since the value of  $\beta$  is small. Consequently, oscillations around equilibrium values are larger than for stronger selection.

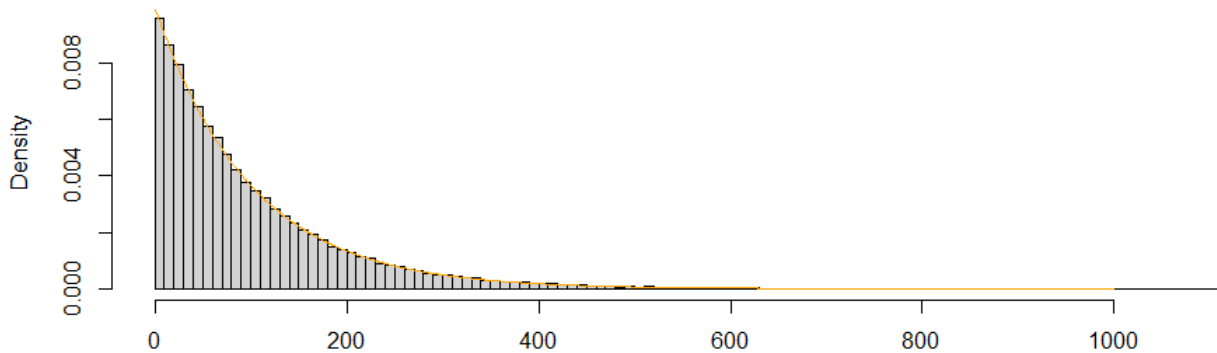


Figure 7: In grey, the normalised histogram or empiric probability density function of the simulation that yielded Fig. 6. In orange, the theoretical shape of a  $\text{Geom}(1/100)=\text{Geom}(1/N)$  distribution. We observe coincidence.

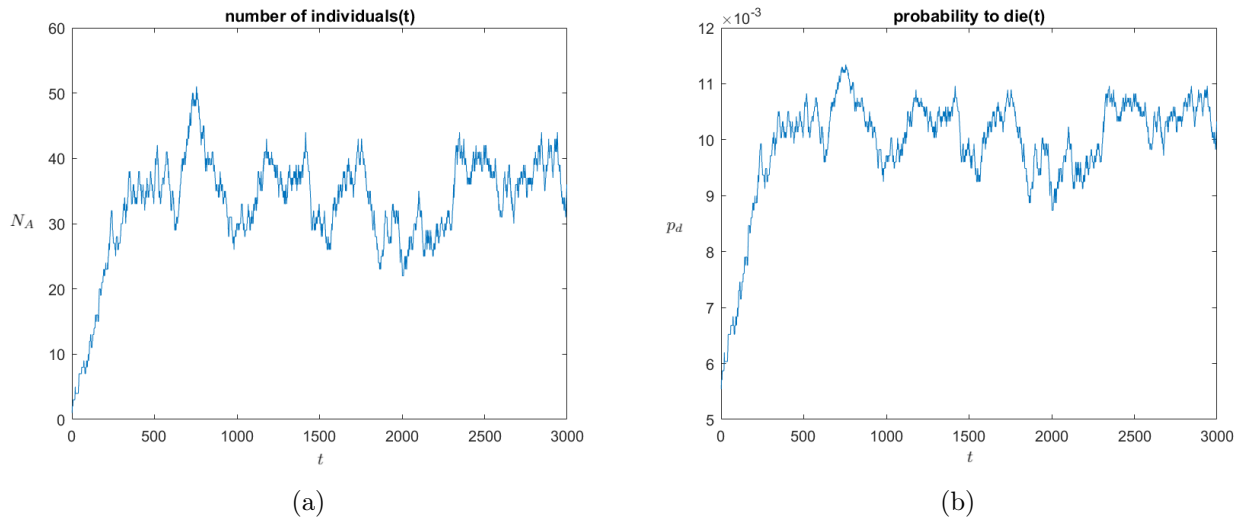


Figure 8: Number of A individuals  $N_A$  and probability of an A individual to die  $p_d$  as a function of time  $t$ , from a stochastic simulation with parameters  $N = 100$ ,  $N_{A,0} = 1$ ,  $10^5$  lifetime samples taken, probability of mutation  $\mu = 5\%$ ,  $M = \begin{pmatrix} 3 & 2 \\ 5 & 1 \end{pmatrix}$  and  $\beta = 1$ . Both magnitudes tend to oscillate around their equilibrium values, given by the equilibrium  $N_A$ , which at the same time is determined by the payoff matrix  $M$ . Oscillations are weaker than those in Fig. 6 due to a larger  $\beta$ .

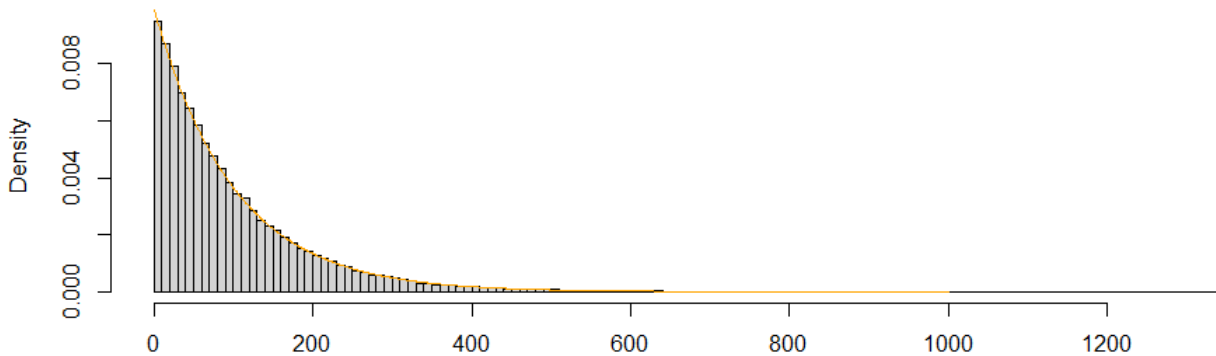


Figure 9: In grey, the normalised histogram or empiric probability density function of the simulation that yielded Fig. 8. In orange, the theoretical shape of a  $\text{Geom}(1/100) = \text{Geom}(1/N)$  distribution. We observe coincidence.

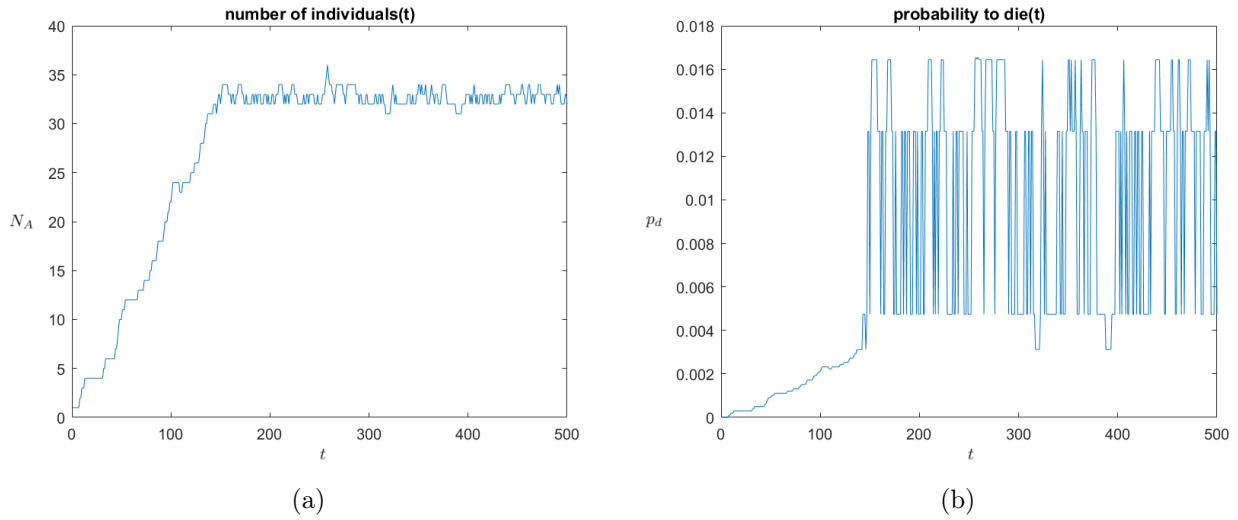


Figure 10: Number of A individuals  $N_A$  and probability of an A individual to die  $p_d$  as a function of time  $t$ , from a stochastic simulation with parameters  $N = 100$ ,  $N_{A,0} = 1$ ,  $10^5$  lifetime samples taken, probability of mutation  $\mu = 5\%$ ,  $M = \begin{pmatrix} 3 & 2 \\ 5 & 1 \end{pmatrix}$  and  $\beta = 100$ . Both magnitudes tend to oscillate around their equilibrium values, given by the equilibrium  $N_A$ , which at the same time is determined by the payoff matrix  $M$ . A large value for  $\beta$ , like in this case, yields tight oscillations.

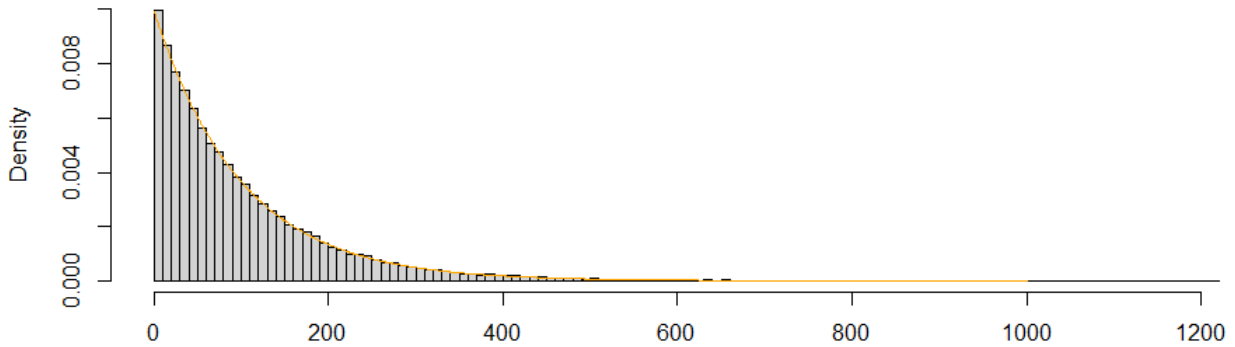


Figure 11: In grey, the normalised histogram or empiric probability density function of the simulation that yielded Fig. 10. In orange, the theoretical shape of a  $\text{Geom}(1/100) = \text{Geom}(1/N)$  distribution. We observe coincidence.

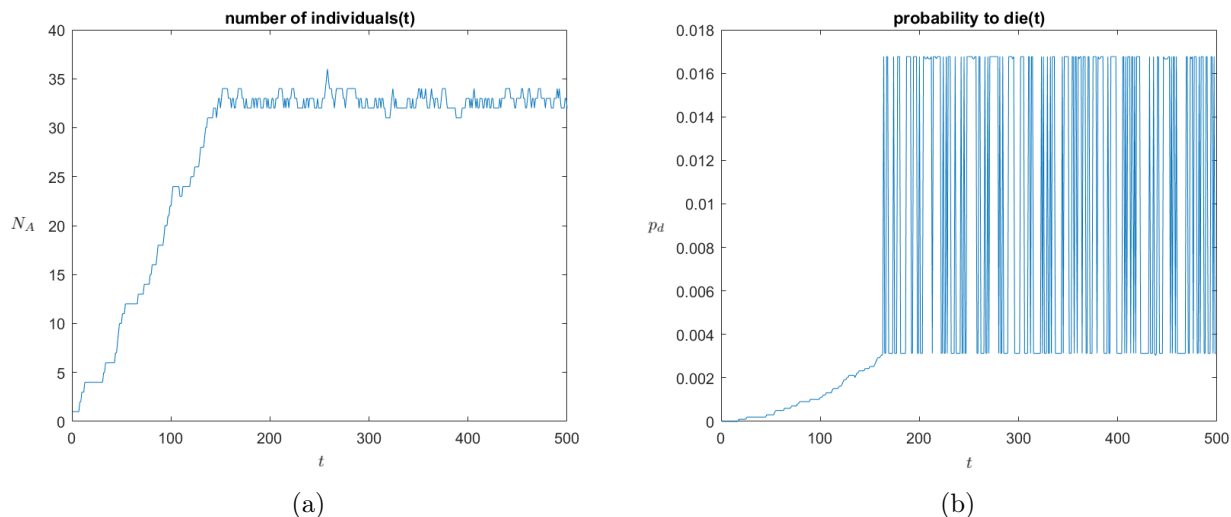


Figure 12: Number of A individuals  $N_A$  and probability of an A individual to die  $p_d$  as a function of time  $t$ , from a stochastic simulation with parameters  $N = 100$ ,  $N_{A,0} = 1$ ,  $10^5$  lifetime samples taken, probability of mutation  $\mu = 5\%$ ,  $M = \begin{pmatrix} 3 & 2 \\ 5 & 1 \end{pmatrix}$  and  $\beta = 10000$ . Both magnitudes tend to oscillate around their equilibrium values, given by the equilibrium  $N_A$ , which at the same time is determined by the payoff matrix  $M$ . The value for  $\beta$  used is even unrealistic, but we try to see if the lifetime distribution is deformed when the range of frequent values of  $N_A$  is smaller than 5 values. Fig. 13 shows that this is not the case.

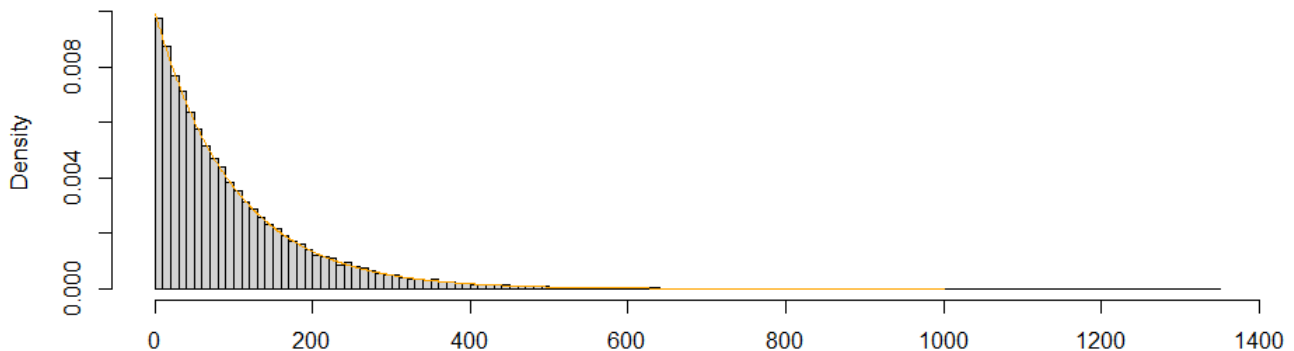


Figure 13: In grey, the normalised histogram or empiric probability density function of the simulation that yielded Fig. 12. In orange, the theoretical shape of a  $\text{Geom}(1/100)=\text{Geom}(1/N)$  distribution. We observe coincidence.

It is concluded that for  $N = 100$ , even though  $\beta$  varies, the empiric density functions are fitted by the orange theoretical geometrical with parameter  $1/N = 1/100$  density function. Introducing logarithms in Eq. (17),

$$\log(p_d(i)) = t \log(1 - p_d) + \log(p_d) \quad (18)$$

so  $[\log(p_d)](t)$  should be a linear dependency under the hypothesis that  $p_d$  can be considered constant. It turns out to be true for  $N = 100$ , Fig. 14.

Recall the fixed point of the coexistence/snowdrift game in Tab. 3, that for this particular case ( $N = 100$  and  $\beta = 1$ ) is position  $N \frac{\mu_A}{\mu_A + \mu_B} \simeq 33$ , for which  $p_d(33) = 0.0100342 \simeq 0.01 = 1/100$ . The conclusion is that fluctuations were not strong enough to disrupt the distribution. This causes no surprise after checking the probability values around the stable position in Tab. 4.

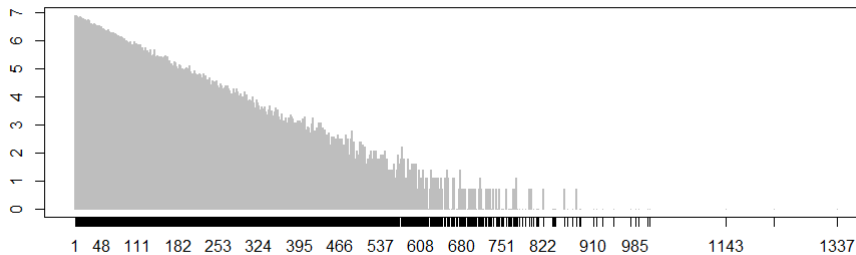


Figure 14: Plot of the logarithm of histogram in Fig. 9. Corroboration of linearity that confirms a distribution  $\text{Geom}(1/100)$  for  $N = 100$  and  $\beta = 1$ , so with the setting that yielded Fig. 8 and Fig. 9. Noise for large lifetimes is due to the finite run time of the simulation, which does not let all potential "long livers" die (the simulation stops when the desired number of lifetime samples is reached).

To get a feeling of how much the magnitude of the fluctuations of  $p_d$  deforms the geometric distribution, we made a short script in *R*. It created  $100000/2$   $\text{Geom}(0.01+\epsilon)$  samples and other  $100000/2$   $\text{Geom}(0.01-\epsilon)$  samples (since the simulation produced 100000 samples). Applying the statistical t-test to check whether the mean of the distribution behind the samples was  $p = 0.01$ , the smallest order of magnitude of  $\epsilon$  for the mean not to be the corresponding  $\frac{1}{p}-1$  (with significance value  $\alpha = 0.05$ ) was  $\epsilon = 0.0009$  (thus  $\Delta\epsilon = 0.0018$ ), which is greater than the fluctuations in Tab. 4. As a consequence, the fluctuations did not modify the mean of the distribution of lifetimes.

position $i$	$p_d$
27	0.00936845
28	0.00948662
29	0.00960198
30	0.00971447
31	0.00982403
32	0.00993062
33	0.0100342
34	0.0101347
35	0.010232
36	0.0103262
37	0.0104172
38	0.010505
39	0.0105895

Table 4: Probabilities  $p_d$  around equilibrium position 33, in the setting of simulations that led to Fig. 8. The order of magnitude of the fluctuations ( $10^{-4}$ ) was not big enough to disrupt the geometrical distribution.

Essentially, the parameter  $p_d$  does not significantly change. The same happens for small values of  $\beta$  (neutral/weak selection) and for large ones (strong selection), as seen in Fig. 6 - Fig. 13. Having a look back at Eq. (16), since there appears a strong factor  $\frac{1}{N(N-1)}$ , to get larger fluctuations it is probably required small  $N$  to obtain stronger fluctuations that may break the geometrical distribution.

However, it turns out that for small  $N$ , the resulting distribution is still geometric, as Fig. 15 shows, even though probabilities in Tab. 5 fluctuate stronger than before.

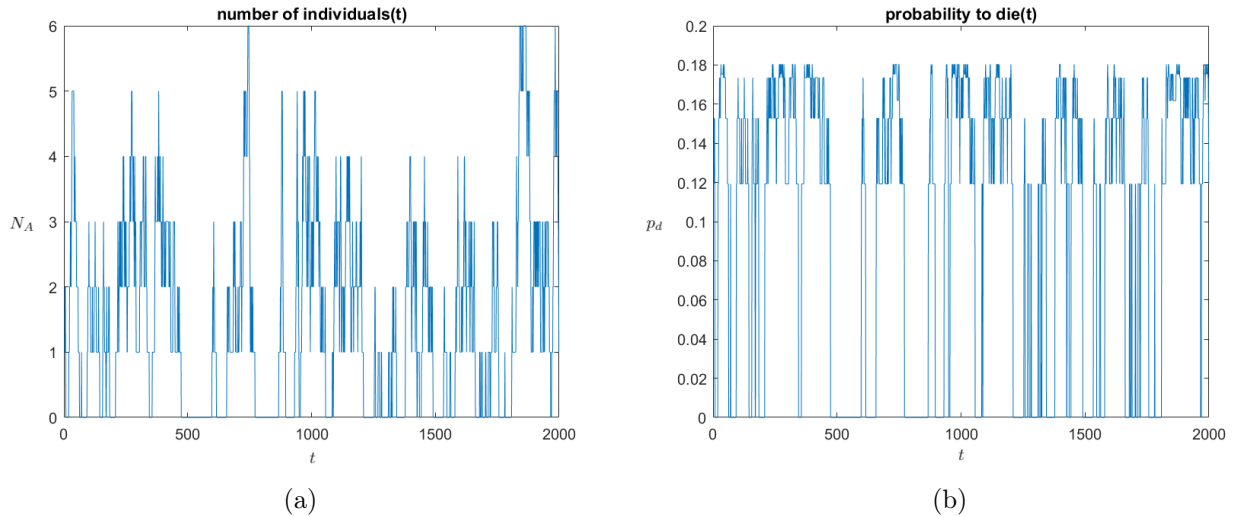


Figure 15: Number of A individuals  $N_A$  and probability of an A individual to die  $p_d$  as a function of time  $t$ , from a stochastic simulation with parameters  $N = 7$ ,  $N_{A,0} = 1$ ,  $10^5$  lifetime samples taken, probability of mutation  $\mu = 5\%$ ,  $M = \begin{pmatrix} 3 & 2 \\ 5 & 1 \end{pmatrix}$  and  $\beta = 1$ . It is now harder to observe clear equilibrium values for both variables. However, as Tab. 5 also shows, we obtained stronger fluctuations in the death probability  $p_d$ .

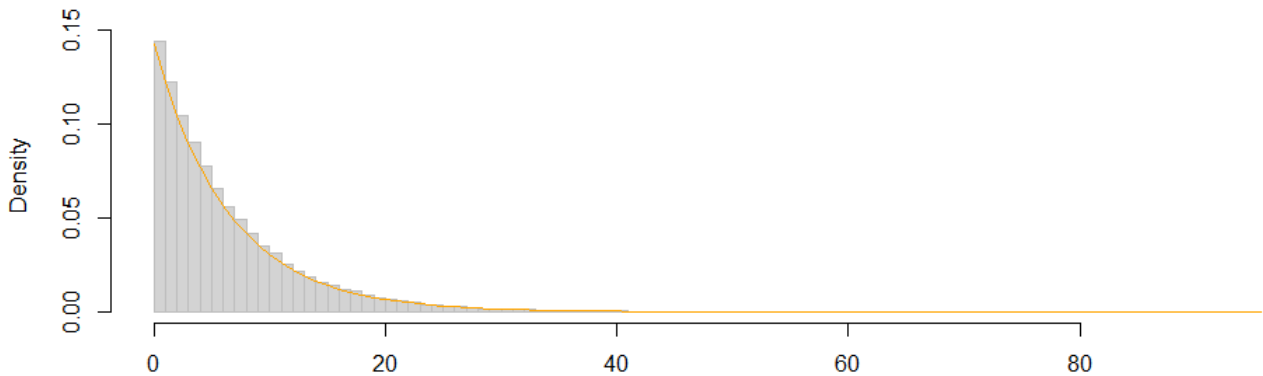


Figure 16: In grey, the normalised histogram or empiric probability density function of the simulation that yielded Fig. 15. In orange, the theoretical shape of a  $\text{Geom}(1/7) = \text{Geom}(1/N)$  distribution. Once again, we observe coincidence.

If we perform the t-test as before, this time picking the parameter  $p = 1/7 = 1/N$ , the result is that the mean is not  $\frac{1}{p} - 1$  (with significance value  $\alpha = 0.05$ ) for  $\epsilon > 0.017$  (thus  $\Delta\epsilon > 0.034$ ), so the tolerance is increased for  $N = 7$  compared to the case  $N = 100$ . The tolerance is again similar to the fluctuations around the Nash equilibrium position in Tab. 5. The reason why the tolerance  $\epsilon$  has increased when lowering  $N$  is that the function for the mean of the geometric distribution,  $\frac{1}{p} - 1$ , has more sensitivity for smaller  $p$ , or equivalently for greater  $N$ .

For the case we have just analysed (with  $\beta = 1$ ), the number of individuals fluctuates between 0 and 6. If we wanted a stronger selection (say  $\beta = 100$ ), so that this range is reduced (maybe to 1 – 2) and the fluctuating values are more controlled, we have to be careful because as Tab. 6 shows, probabilities can be arbitrarily close to 0. The geometric distribution is not defined for the parameter  $p = 0$ , thus close values may lead to anomalies or unreliable results, Fig. 17, since lifetimes are greatly increased but simulation run time may be not so long.

position $i$	$p_d$
1	0.119266
2	0.152755
3	0.173477
4	0.180363
5	0.175346
6	0.161772
7	0.142857

Table 5: Probabilities  $p_d$  around equilibrium position 2, for the setting associated to Fig. 8 ( $\beta = 1$ ) but instead taking  $N = 7$ . More noticeable fluctuations than in Tab. 4, this time of the order of  $10^{-2}$ . However, not even this time the fluctuations beat the geometric distribution, Fig. 16.

position $i$	$p_d$
1	9.53782e-016
2	0.261905
3	0.238095
4	0.214286
5	0.190476
6	0.166667
7	0.142857

Table 6: Probabilities  $p_d$  around equilibrium position 2, for the setup of Fig. 10 ( $\beta = 100$ ) but instead taking  $N = 7$ .  $p_d$  for  $i = 1$  is too close to 0, meaning that it takes too long for the simulation to get deaths of A individuals when  $i = 0$ , and perhaps leading to anomalies (Fig. 17).

### 3.2 Model including ageing

**One possible starting point:** We consider a case in which age only affects the probability to die (so the probability that the other player beats you). This means that  $h(\tau_i, \tau_j) = h(\tau_j)$ , or in other words:

$$\begin{aligned} i \text{ reproduces with probability } p_i &= g(\pi_i - \pi_j) \times h(\tau_j), \\ j \text{ reproduces with probability } p_j &= g(\pi_j - \pi_i) \times h(\tau_i). \end{aligned} \quad (19)$$

Our initial choice is

$$h(\tau) = \frac{\tau}{10 + \tau}, \quad (20)$$

Note that it holds that  $h(\tau) \leq 1$  for all  $\tau \geq 0$ . Also, realise that  $h$  in Eq. (20) is increasing, so older individuals yield greater values of  $h$ , meaning that the probability that their opponents reproduce is greater. In other words, in this setup older individuals are more likely to die.

Taking this implementation of ageing in the model, now the probability to die is much harder to compute because each individual has a specific age, thus Eq. (16) is no longer valid.

Our simulations yield Fig. 18, which shows the lifetime distribution is not geometric. It is likely that its distribution is not one of the common ones: we should determine the expression for  $p_d$  taking ageing into account and plugging it in the geometric distribution formula.

## 4 Cancer modelling

Moran processes models suit in general for situations in which two distinct communities clash for dominance. A particular application is cancer modelling. Let us suggest ideas for this purpose.

Firstly, in a tumor, the number of cells is not constant along time. Tumors tend to grow because cancer cells reproduce at high rates and do not die. To take this into account in a Moran process, we should not work with the exact number of cells but with the proportion of normal vs cancer cells.

Starting with one A individual in the community, which represents a mutant cancerous cell, makes sense for the scenario of a kick-off. The payoff matrix should give advantage to cancer (A) cells, so we should choose a drag payoff matrix like  $M = \begin{pmatrix} 3 & 2 \\ 2 & 1 \end{pmatrix}$ .

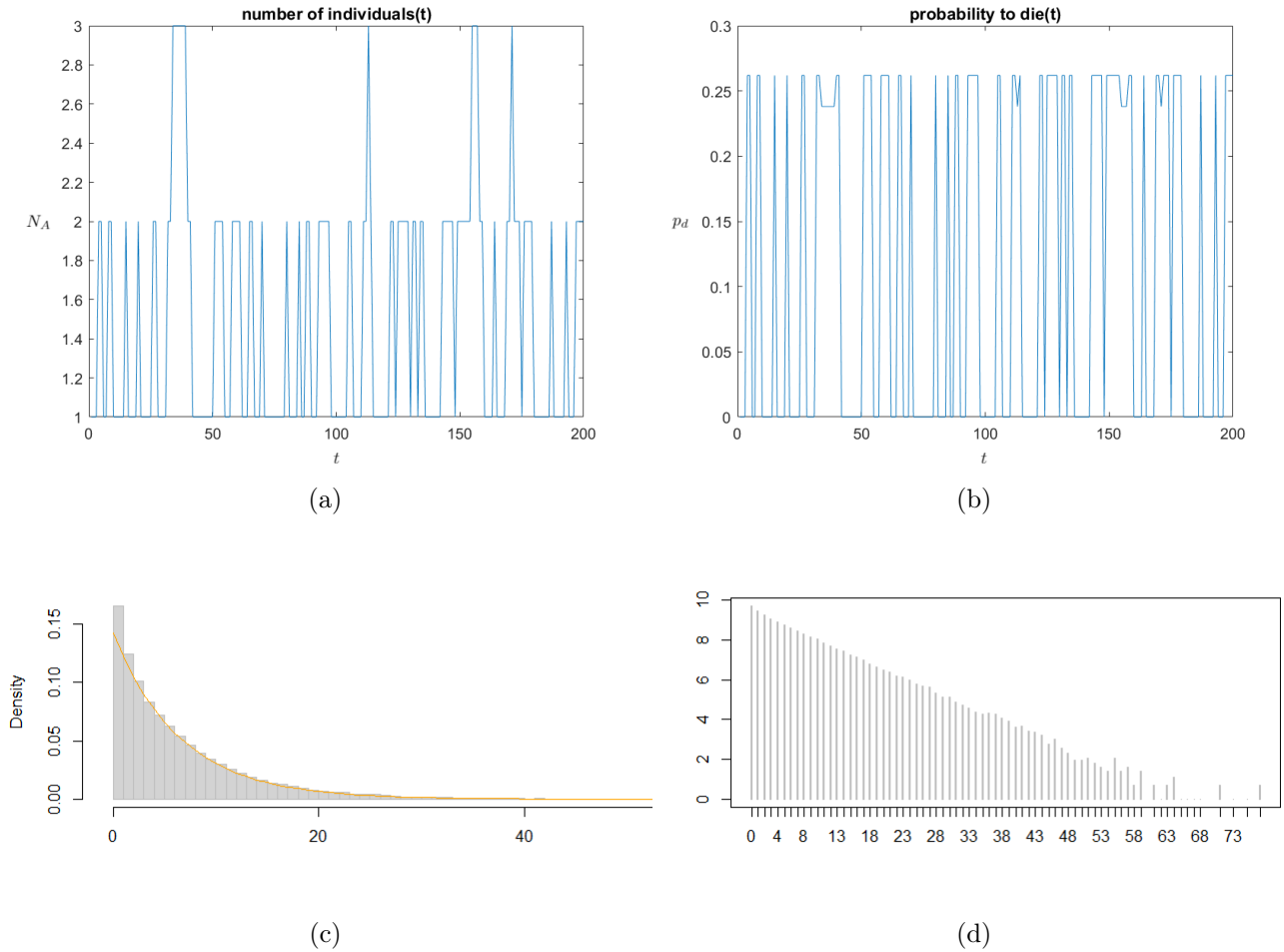


Figure 17: (a) Number of A individuals  $N_A$  and (b) probability of an A individual to die  $p_d$  as a function of time  $t$ , from a stochastic simulation with parameters  $N = 7$ ,  $N_{A,0} = 1$ ,  $10^5$  lifetime samples taken, probability of mutation  $\mu = 5\%$ ,  $M = \begin{pmatrix} 3 & 2 \\ 5 & 1 \end{pmatrix}$  and  $\beta = 100$ . (c) In grey, the normalised histogram or empiric probability density function of the simulation. In orange, the theoretical shape of a  $\text{Geom}(1/7)=\text{Geom}(1/N)$  distribution. (d) Plot of the logarithm of (c) to check linearity. There is danger of anomalies since  $p_d$  takes values too close to zero. In (c) the orange function does not fit so well this time, but this outcome is not useful to draw conclusions due to the issue about  $p_d$ .

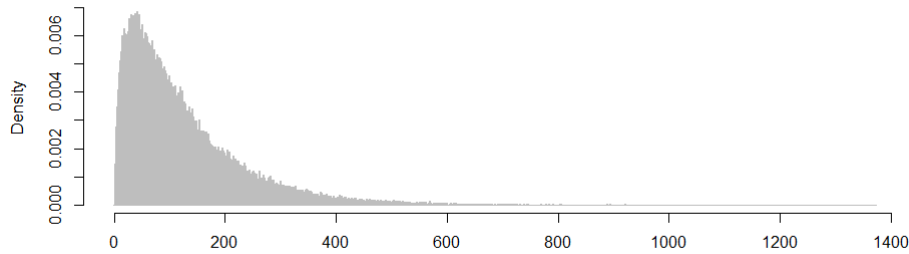


Figure 18: Empiric lifetime distribution in our model considering ageing. The setup is as in Fig. 8 (so  $N = 100$  and  $\beta = 1$ ) and we implement ageing using the ageing function of Eq. (20). Clearly not a geometric distribution, as expected, due to the ageing effect.

A realistic value for the kind of mutation we considered (A-B strategy mutation) would be  $\mu = 10^{-6}$ . However, we may want to take into account other types of mutation.

**Definition 4.1. Driver mutations** are those mutations that confer a growth advantage to cancer cells.

**Definition 4.2. Passenger mutations** are those mutations that do not confer a growth advantage to cancer cells.

We could forget about passenger mutations since they do not significantly affect the reproducing rates. Nevertheless, driver mutations are interesting to be included. According to the fact that they provide cancer cells with a growth advantage, we suggest to add a probability  $\mu_d = 10^{-6}$  for the payoff matrix to change, for instance  $M \rightarrow M + \begin{pmatrix} 2 & 1 \\ 1 & 0 \end{pmatrix}$ , to strengthen the rewarding strategy A drag.

The case of human cells would not be the ideal situation to include ageing, because cancer spreads faster than cells die (human cells are replaced, on average, each 7-8 years).

Another option would be studying the treatment of cancer. One question to be answered could be: When should doctors start a treatment before chances of recovery are too low? The treatment may be implemented in the model through the payoff matrix as well, and it could depend on the proportion of cancer cells present. Consider, for example, an update of the payoff matrix for every time step like the following.

$$M(t) = M(t-1) + \begin{pmatrix} -\epsilon(a) & 0 \\ 0 & +\epsilon(a) \end{pmatrix} \quad (21)$$

$a$  denotes the proportion of A individuals present, and  $\epsilon$  is a monotonous function of  $a$  to be chosen.

As we mentioned before, it would be interesting to study how late can the treatment be provided so that the proportion of cancer cells  $a$  do not surpass a certain threshold, or so that full recovery ( $a = 0$ ) is possible after a time.

## 5 Conclusions

As we have checked, Moran processes are simultaneously a relatively simple, versatile and powerful tool to study processes involving two competing communities. Simple in the sense that Fig. 2 essentially captures what a Moran process is. Versatile because it lets us include or remove features like mutation or ageing, amongst others, at our will. And powerful, taking into account that they come in handy in transcendental tasks such as cancer modelling.

This report paid special attention to the study of the lifetime distribution of individuals in a Moran process. In the lack of ageing case, we checked that the lifetime distribution follows a geometric distribution, no matter what the magnitudes of both  $N$  or  $\beta$  are, as justified in Section 3.1.

All in all, Moran processes unlock a vast collection of topics to explore, in many applied physics branches, such as biophysics, medicine and telecommunications.

## Acknowledgments

We thank the coordinators of the SURF program, Manuel Matías and Marta, as well as Tobias's Master and PhD students, Annalisa, Fer, Rubén, and Teresa for their welcome.

This work was supported by the SURF@IFISC fellowship.

## References

- [1] Erwin Frey, *Evolutionary Game Theory: Theoretical Concepts and Applications to Microbial Communities*, 3-11, 2010.
- [2] Philipp M Altrock and Arne Traulsen 2009 New J. Phys. 11 013012.
- [3] A.F. Peralta, N. Khalil and R. Toral, *Ordering dynamics in the voter model with aging*, Physica A (2019) 122475, <https://doi.org/10.1016/j.physa.2019.122475>.

# Particle motion in a Bose-Einstein Condensate

Jorge Valencia, Emilio Hernández-García, Cristóbal López  
 Instituto de Física Interdisciplinar y Sistemas Complejos, IFISC (CSIC-UIB)  
 Campus Universitat de les Illes Balears, E-07122 Palma de Mallorca, Spain

## Abstract

We study the motion of a test particle or impurity immersed in a three-dimensional Bose-Einstein condensate (BEC) confined in a cylinder. The behaviour of the particles of the condensate is modelled by an effective wavefunction which follows Gross-Pitaevskii equation. We consider a weak interaction condensate and a Gaussian repulsive potential between the impurity and the particles of the BEC. The force experienced by the particle is calculated with the Ehrenfest theorem. Therefore, due to Madelung transform we are able to treat the system as a quantum fluid and compare the force exerted on the particle by the BEC with the force that would act on it in the case of classical fluid dynamics. Two simple cases are analyzed in this report: the motion of a particle in a BEC in a gravitational field and in a sound-wave field.

## 1 Introduction

When atoms of a gas are cooled, their energy decreases and so their speed. As speed is reduced, if it is known more precisely, the probability density of finding a particle in some specific point becomes broader, as stated by Heisenberg uncertainty principle. If the temperature keeps decreasing, the quantum nature of the atoms rises above the corpuscular nature, increasing the wave length of each of them and becoming non-localized particles. When temperature reaches the order of  $500 \sim 800$  nK, the atoms of the gas can collapse into the same quantum state, the ground state generally (where all of them have the same energy, the minimum energy) and form a new state of matter called Bose-Einstein condensate (BEC) [1], as shown in Fig. 1. This state of matter can only be formed by bosons (particles with integer spin) due to Pauli exclusion principle that avoids two or more fermions to stay at the same quantum state simultaneously.

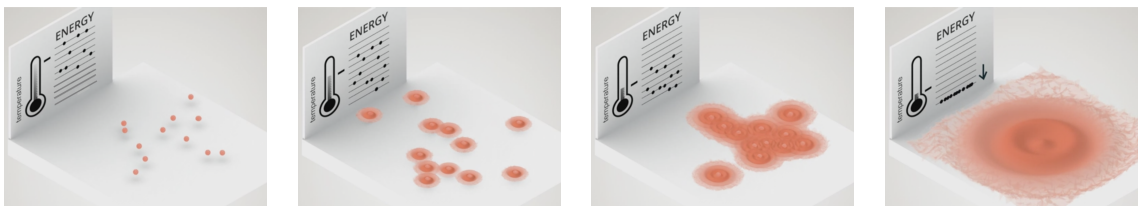


Figure 1: Illustrative scheme of the formation of a Bose-Einstein condensate [5].

At non-zero temperature, the atoms of the BEC can interact with each other and be promoted to the first excited state. However, in the ideal case with zero temperature, all particles stay at the ground state. Our study centers in atomic BECs where the interactions between their particles are weak due to extreme diluteness [1]. In order to analyze the system, we do not study the N-body wavefunction formed by each of the atoms of the BEC. Instead of that, and due to the great diluteness of the condensate, we are able to approximate the system with a unique effective wavefunction. This macroscopic wavefunction is modelled by the Gross-Pitaevskii equation (GPE).

GPE can be rewritten using the Madelung transform in terms of the density number and velocity of the BEC, that is now treated as a quantum fluid. In this way, analogies with classical forces of fluid dynamics can be made.

The aim of this paper is to study the forces acting on a impurity moving in a three-dimensional BEC and compare them to the forces of classical fluid dynamics studied by Maxey-Riley [2]. Previous studies have been done in two-dimensional BEC [3, 4] considering a thermal bath in contact with the condensate. In that case, a damping force appears similar to a drag force in the classical

fluid dynamics. However, in our case, we study an ideal condensate with zero temperature, i.e. no thermal bath exists. Then, there is not any drag force caused by the interaction between the BEC and the external bath. Our objective is to generalize some of the results reached in [3] to three dimensions.

Weak interactions between the impurity and the atoms of the condensate are also taken into account in GPE through a Gaussian repulsive potential and the force is calculated through Ehrenfest theorem as done in [3].

In this work two simple cases are analyzed: the BEC in a gravitational field, Sec. 3.1, and the BEC in a sound-wave field, Sec. 3.2. In the first case, the main force will be the buoyancy exerted by the BEC on the particle caused by the existence of a density number gradient due to gravitational force. This force is compared with the classical buoyancy force of Arquimedes' principle exerted by an steady and homogeneous fluid. Two situations are considered. The first approximation neglects quantum effects as the quantum pressure that appears near the walls of the cylinder where the BEC is confined. Analytical solutions for GPE, in its hydrodynamic form, can be obtained for this ideal case. Then in the second situation, quantum pressure is considered and GPE is solved numerically setting boundary conditions such that density must vanish at the base and the top of the cylinder. The results obtained are compared with the ones neglecting quantum pressure, in the areas far from the walls, i.e. the center of the cylinder. In Sec. 3.2, the methodology followed consists on treating inhomogeneities introduced by the impurity as small perturbations of the ground state of the BEC and linearize GPE. Then, assuming travelling waves solutions Bogoliubov dispersion relation is obtained and the force is calculated by the Ehrenfest theorem and by different approximations.

## 2 Theoretical model

We model the motion of an impurity with size of the same order than the healing length, i.e. the minimal distance over which the wavefunction,  $\psi$ , changes spatially [1]. We denote the healing length as  $\xi$ , with a typical value of  $10^{-6}$  m.

Systems in which condensates are at non-zero temperature are ruled by the damped Gross-Pitaevskii equation (dGPE) that includes the damping coefficient  $\gamma$ . This coefficient takes into account the interactions between the thermal bath formed by excited atoms and the atoms of the BEC which stay in the ground state [3]. In this work we study ideal systems where temperature is zero and the BEC is well described by Gross-Pitaevskii equation, GPE:

$$i\hbar \frac{\partial \psi}{\partial t} = \left( -\frac{\hbar^2}{2m_B} \nabla^2 + g_B |\psi|^2 - \mu + V + g_p \mathcal{U}_p \right) \psi, \quad (1)$$

where  $\psi$  is normalized to the number of particles,  $\int |\psi|^2 d^3\mathbf{r} = N$ , and the interaction between the impurity and the particles in the BEC is modelled by a 3-dimensional Gaussian repulsive potential  $\mathcal{U}_p(\mathbf{r} - \mathbf{r}_p) = \mu / (\sqrt{2\pi}\sigma)^3 e^{-(\mathbf{r}-\mathbf{r}_p)^2/2\sigma^2}$ . With  $\mu$ , the chemical potential;  $\sigma$ , the effective size of the impurity and  $\mathbf{r}_p$ , its center-of-mass position. In Eq. (1),  $m_B$  is the mass of the condensate atoms,  $V$  is the external potential,  $g_p$  is a positive (repulsion) parameter (with volume units) related to the interaction between the impurity and the BEC and  $g_B$  is an effective scattering parameter between the particles of the condensate:

$$g_B = \frac{4\pi a_s \hbar^2}{m_B}, \quad (2)$$

being  $a_s$  the s-wave scattering length [1].

The Gross-Pitaevskii equation can be written in a hydrodynamic form substituting the wave function in Eq. (1) by  $\psi(\mathbf{r}, t) = \sqrt{n(\mathbf{r}, t)} e^{iS(\mathbf{r}, t)}$ , known as the Madelung transform. Where  $n$  is the density number, related to the module of the wavefunction as  $|\psi|^2 = n$  and  $S$  is its phase, which can be expressed as a function of the condensate velocity [1]:

$$\mathbf{v} = \frac{\hbar}{m_B} \nabla S. \quad (3)$$

Applying the Madelung transform to Eq. (1), two equations, similar to fluid dynamics, are obtained:

$$\frac{\partial n}{\partial t} + \nabla \cdot (n\mathbf{v}) = 0, \quad (4)$$

which is identical to a continuity equation of classical fluid dynamics and

$$m \frac{\partial \mathbf{v}}{\partial t} = -\nabla \left( \frac{m_B \mathbf{v}^2}{2} + V + g_B n - \frac{\hbar^2}{2m_B} \frac{\nabla^2 \sqrt{n}}{\sqrt{n}} + g_p \mathcal{U}_p \right) \quad (5)$$

similar to Euler equation for a inviscid fluid if some algebraic manipulation is done. In this hydrodynamic view, the pressure can be interpreted as  $P = g_B n^2/2$ , which means the BEC is a barotropic fluid [1]. Also,  $\frac{\hbar^2}{2m_B} \frac{\nabla^2 \sqrt{n}}{\sqrt{n}}$  is called the quantum pressure term.

The force exerted by the BEC on the impurity is determined by the Ehrenfest theorem [3]:

$$\mathbf{F}_p(t) = -g_p \int d^3\mathbf{r} \mathcal{U}_p(\mathbf{r} - \mathbf{r}_p, t) \nabla |\psi(\mathbf{r}, t)|^2, \quad (6)$$

where in the hydrodynamic interpretation  $\nabla |\psi|^2$  is substituted by  $\nabla n$ . This equation gives the exact force exerted on the particle by the condensate. In some simpler situations such weak velocity variations at scales smaller than  $\xi$ , the force can be approximated by [3]:

$$\mathbf{F}_p(t) = \frac{g_p}{g_B} m_B \frac{D\mathbf{v}}{Dt} \quad (7)$$

with  $\mathbf{v}$  the velocity of the condensate in the position of the impurity observed in the laboratory frame (at rest). For 1D motion in the  $z$  direction Eq. (7) can be simplified to:

$$\mathbf{F}_p(t) = \frac{g_p}{g_B} m_B \left( \frac{\partial v}{\partial t} + v \frac{\partial v}{\partial z} \right) \hat{z}. \quad (8)$$

The velocity in Eq. (7) can be calculated from Eq. (3) which can be manipulated algebraically and rewritten as:

$$\mathbf{v} = \frac{\hbar}{\rho_0} \text{Im}(\psi^* \nabla \psi), \quad (9)$$

where  $\rho_0 = m_B n_0$  denotes the BEC density in the absence of external potential.<sup>12</sup>

## 3 Results and discussion

### 3.1 Gravitational field

In this section we will study the motion of a particle immersed in a gravitational field and located in a steady BEC ( $|\mathbf{v}| = 0$ ) which is confined in a cylindrical potential ( $R \rightarrow \infty$ ) with height  $L = 10\xi$ . The external potential,  $V$ , of Eq. (1) takes the form of a gravity potential,  $m_B g z$ .  $m_B$  is the mass of the particles of the BEC.

#### 3.1.1 Neglecting quantum pressure

Neglecting quantum pressure term in Eq. (5) and assuming a steady BEC leads to a linear density number profile:

$$n(z) = \frac{\mu}{g_B} - \frac{m_B g}{g_B} z \quad (10)$$

where  $\mu$  is a constant (with Joules units) that can be identified as the chemical potential and it is calculated taking into account the conservation of the number of particles:

$$\int n(z) d^3\mathbf{r} = N \Rightarrow \mu = n_0 g_B + \frac{1}{2} m_B g L. \quad (11)$$

where  $n_0 = N/(AL)$  (with  $A$  the area of the base of the cylinder) is the density number profile in the absence of external potential. In that case, the term  $\frac{1}{2} m_B g L$  disappears and  $\mu_0 = n_0 g_B$ .

With Eq. (10) and Eq. (11) the density number profile in dimensionless variables is:

$$n(z) = \frac{\mu}{\mu_0} - k z, \quad (12)$$

with the dimensionless parameter  $k \equiv m_B g \xi / \mu_0$ . The dimensionless process of [3] has been followed.

Note that this expression describes a non-real BEC in which the number density is different from zero at the base of the cylinder, at  $z = 0$ , and diverges for large heights. However, Eq. (10) and Eq. (12) can be used as a first approximation of the behaviour of  $n$  far from the walls of the cylinder, where quantum pressure is negligible. In those areas, the number density decays linearly with height.

<sup>1</sup>The subindex 0 refers to the absence of external potential,  $V = 0$ .

<sup>2</sup>See Appendix for a detailed derivation of Eq. (9).

To determine the force the BEC is exerting on the impurity, the number density profile above must be substituted in Eq. (6). That yields:

$$\mathbf{F}_p(t) = g_p \rho g \hat{z} \quad (13)$$

with  $\rho = m_B n$  the BEC density.

The expression of the force in Eq. (13) can be compared with the buoyancy force in classical fluids for which a particle in a fluid has an upward force proportional to its submerged volume. For the case the impurity is a sphere of radius  $\sigma$  fully submerged in a fluid, this force is:

$$\mathbf{F}_p(t) = \frac{4}{3} \pi \sigma^3 \rho g \hat{z} \quad (14)$$

This is equivalent to Eq. (13), where the factor  $g_p$  plays the role of the volume of the particle. This analogy is supposed to be valid only if inhomogeneities introduced by the presence of the impurity can be neglected and changes of the velocity are weakly varying [3].

In order to consider these small perturbations the impurity introduces, one can treat them as small disturbances of the homogeneous state [3]. First, following [3] Eq. (4) and Eq. (5) can be expressed in dimensionless variables (we will avoid different notation to identify dimensionless variables to simplify):

$$\frac{\partial n}{\partial t} + \nabla \cdot (n \mathbf{v}) = 0, \quad (15)$$

which is identical to Eq. (4) but now with no dimension, and Eq. (5) becomes:

$$\frac{\partial \mathbf{v}}{\partial t} = -\nabla \cdot \left( \frac{1}{2} \mathbf{v}^2 + kz + n + g_p \mathcal{U}_p \right). \quad (16)$$

Once dimensionless variables equations are reached, we substitute:

$$\begin{aligned} n(\mathbf{r}, t) &= n_h(z) + g_p \delta n(\mathbf{r}, t) \\ \mathbf{v}(\mathbf{r}, t) &= g_p \delta \mathbf{v}(\mathbf{r}, t) \end{aligned} \quad (17)$$

where  $n_h$  denotes the density number profile without impurity, given by Eq. (12). Note that the velocity of a steady BEC with no impurity in it is zero ( $|\mathbf{v}_h| = 0$ ), only a small velocity  $\delta \mathbf{v}$  is introduced by the particle.

First order perturbations described in Eq. (17) introduced into Eq. (15) and Eq. (16) drives to a wave equation for  $\delta n$ :

$$\frac{\partial^2}{\partial t^2} \delta n = \nabla \cdot [n_h \nabla (\delta n + \mathcal{U}_p)], \quad (18)$$

which could be solved for  $\delta n$  and calculate the force on the impurity with Eq. (6).

### 3.1.2 Considering quantum pressure

Considering quantum pressure term in Eq. (5) in a steady, cylindrically confined BEC where we can neglect derivatives with respect to  $x$  and  $y$  (because the radius of the cylinder tends to infinity); drives to the equation, in dimensionless variables:

$$\frac{\partial^2 \lambda}{\partial z^2} = 2 [(kz - q) \lambda + \lambda^3], \quad (19)$$

with  $\lambda \equiv n^2$  and being  $k \equiv m_B g \xi / \mu_0$  and  $q \equiv C / \mu_0$  dimensionless parameters. The constant  $C$  (with Joules units) is determined due to particle number conservation.

Numerical solutions for Eq. (19), with different values for  $k$  and  $q$ , are shown in Fig. 2. The degree of freedom of studying a steady BEC allows us to choose a value of  $C$ , in the definition of  $q$ , that preserves the total number of particles,  $N$ . As we treat Eq. (5) only in 1D, the area under the curves in panel (A) of Fig. 2 represents the total number of particles per unit of area, which is also a constant. The density number,  $n$ , is higher near the base of the cylinder as the dimensionless parameter  $k$  is increased. Also, as  $k$  is augmented particles tend to lay closer to the base, that means, the effective healing length reduces when  $k$  increases.

Far from the base and the top of the cylinder, quantum pressure can be neglected and the density number profile has a linear behaviour with  $z$ , as expected from Eq. (10), see panel (A) of Fig. 2. The values of the gradient (the derivative with respect to  $z$ ) of the density number profiles in these points are close to the ones of the slope showed in Eq. (10). In Fig. 3 is shown the linear

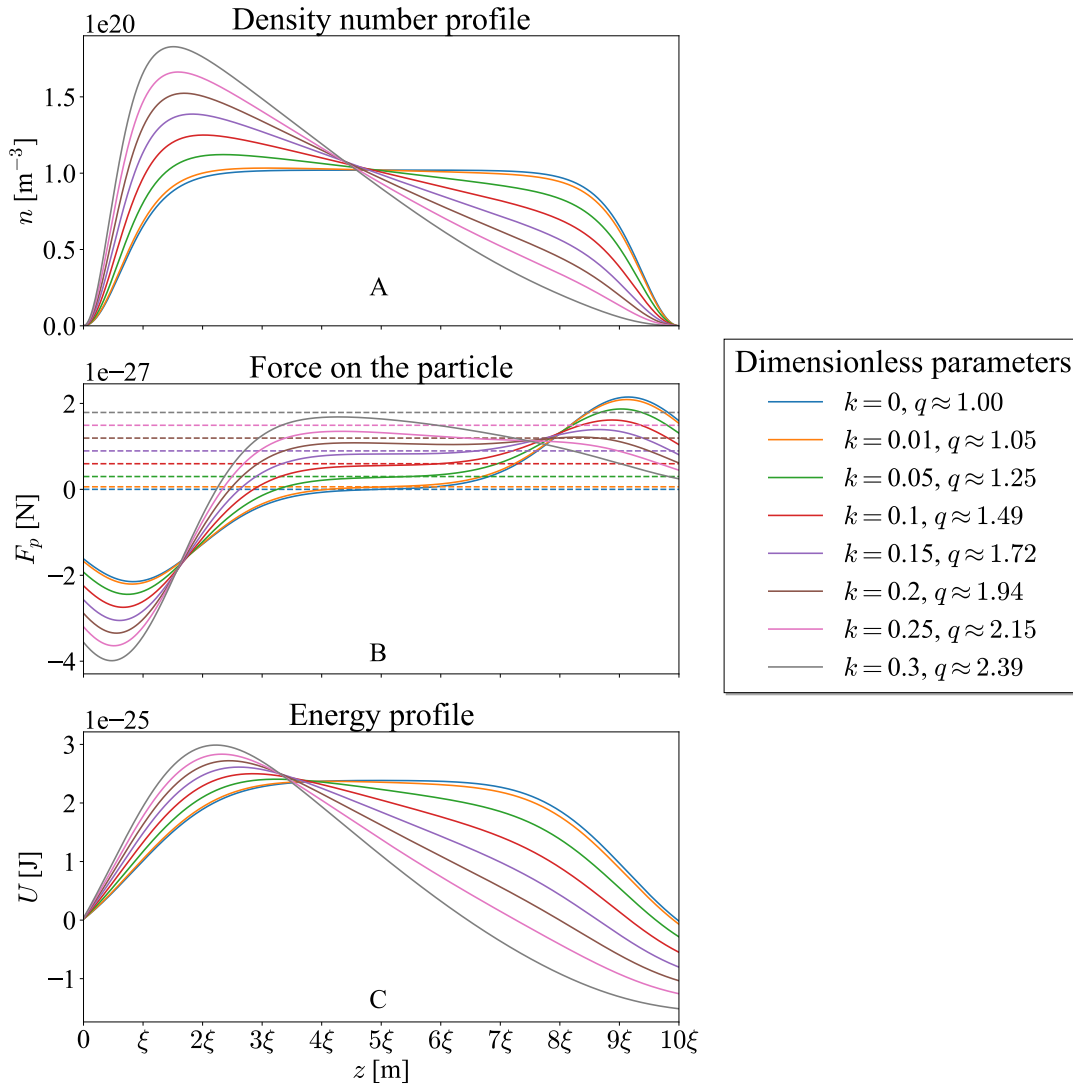


Figure 2: Panel (A) shows the result, with dimensional variables, of the direct numerical simulation of Eq. (19) considering a BEC with homogeneous density number  $n_0 \sim 10^{20} \text{ m}^{-3}$ . Panel (B) is the force exerted on a test particle submerged in the BEC as a function of height,  $z$ , which is labeled in units of the typical healing length scale  $\xi$ . This force is calculated using numerical integration of Eq. (6). In this panel, dashed lines represent the force in the case in which quantum pressure is not considered. Panel (C) shows the energy profile,  $U$ , where the force is  $\mathbf{F} = -\nabla U$ .

density number profiles when quantum pressure is not considered, which match the non-linear density number profiles in areas located far from the base and top of the cylinder for values of  $k$  up to 0.15 (see panel (A)). When  $k$  becomes higher: 0.2, 0.25 and 0.3 (panel (B)) quantum pressure changes density profile behaviour even far from walls and it cannot be underestimated.

If an impurity is submerged in the condensate at a certain height, the force it will suffer, that we can call buoyancy force, is represented in panel (B) of Fig. 2. At a certain height, different for each  $k$ , there is a change of sign in the force that locates a critical point below which the particle will sink until it reaches the base of the cylinder. Right at the critical point the buoyancy force exerted by the BEC on the particle is zero. Above the critical point the particle will float as long as buoyancy force is greater than its weight. That behaviour can easily be observed in panel (C) of Fig. 2 where the energy profile,  $U$ , calculated from  $\mathbf{F} = -\nabla U$ , is shown. The critical point is located at the maximum of each curve. The sinking zone is to the left of that maximum and the buoyancy zone (if the particle weight allows it) is to the right of it. For small  $k$ 's like 0 or 0.01 tiny perturbations around  $z \sim 5\xi$  will trigger the sinking or the flotation of the particle.

In addition, the force exerted on a test particle far from the walls of the cylinder must be approximately constant, as shown in panel (B) of Fig. 2 between  $z \sim 3\xi$  and  $z \sim 7\xi$ . Numerically, this force matches with Eq. (13) (dashed lines) for  $k = 0, 0.01, 0.05, 0.1$  and 0.15 and starts to fail

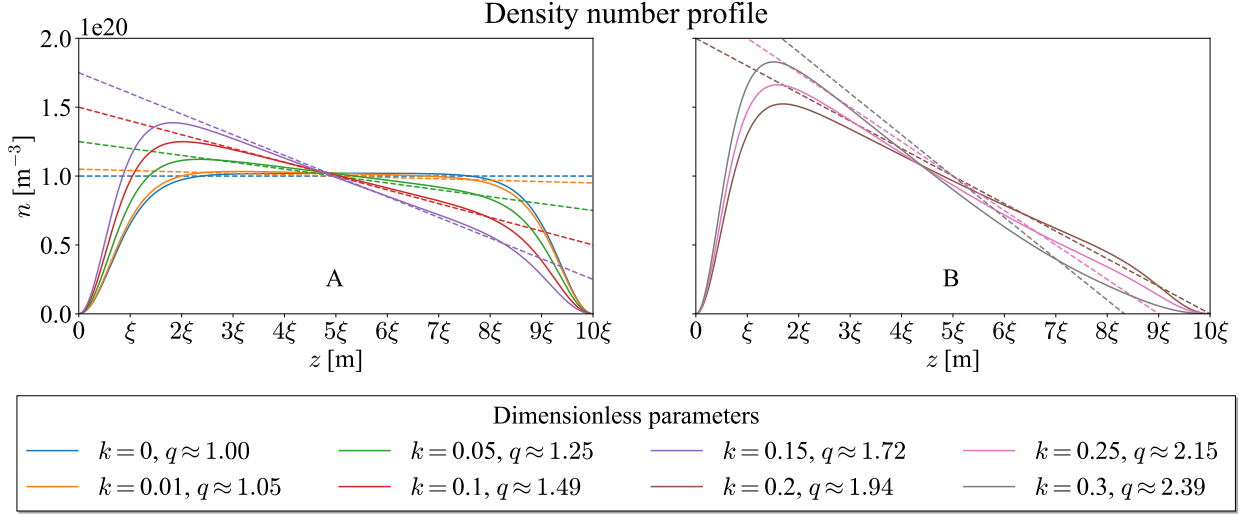


Figure 3: y axis is shared between both plots which represent the density number profile,  $n$ , as a function of  $z$  when quantum pressure is neglected (dashed lines) and when it is not neglected (solid line) for different values of  $k$  and  $q$ .

with larger  $k$ 's.

### 3.2 Sound-wave field

In this section we study the force acting on an impurity, submerged in a BEC, driven by a sound-wave field.

Small perturbations of the BEC in absence of external potential ( $V = 0$ ) can include sound waves, which are small oscillating density perturbations of the ground state of the condensate. For one dimensional motion in the  $z$  direction, the Gross-Pitaevskii equation is [1]:

$$i\hbar \frac{\partial \psi}{\partial t} = \left( -\frac{\hbar^2}{2m_B} \frac{\partial^2}{\partial z^2} + g_B |\psi|^2 - \mu \right) \psi, \quad (20)$$

whose homogeneous solution is  $\psi_0 = \sqrt{\mu_0/g_B}$ . This solution has a density number profile  $n_0 = |\psi_0|^2 = \mu_0/g_B$ , as mentioned in the previous section.

Perturbing the uniform state to first order:  $\psi(z, t) = \psi_0 + \delta\psi(z, t)$  and neglecting quadratic terms in  $\delta\psi$  [1]:

$$i\hbar \frac{\partial}{\partial t} \delta\psi = -\frac{\hbar^2}{2m_B} \frac{\partial^2}{\partial z^2} \delta\psi + \mu_0 (\delta\psi + \delta\psi^*). \quad (21)$$

Assuming wave solutions, i.e.:  $\delta\psi(z, t) = A e^{i(kz - \omega t)} + B^* e^{-i(kz - \omega t)}$  with  $A$  and  $B$  being complex amplitudes,  $k$  the wave number and  $\omega$  the angular frequency of the wave, we arrive to the Bogoliubov dispersion relation [1]:

$$\omega(k) = \sqrt{\left( \frac{\hbar k^2}{2m_B} \right)^2 + \frac{n_0 g_B}{m_B} k^2}. \quad (22)$$

The dependence of  $\omega$  on the wave number described in Eq. (22) foretells a linear and parabolic behaviour for small and large  $k$ , respectively, as shown in Fig. 4. The magnitude of  $k$  is compared with the length scale,  $\xi$ .

We study the general case of two opposite travelling waves with different wave numbers and angular frequencies:  $\psi = A e^{i(k_1 z - \omega_1 t)} + B^* e^{-i(k_2 z - \omega_2 t)}$  where  $\omega_1$  and  $\omega_2$  are given by Bogoliubov dispersion relation, Eq. (22). The force exerted by this sound-wave field on the impurity can be obtained analitically with Eq. (6):

$$F_p(t) = 2\mu_0 g_p (k_1 + k_2) e^{-\frac{\sigma^2}{2} (k_1 + k_2)^2} (C_1 \sin \alpha + C_2 \cos \alpha), \quad (23)$$

where  $\alpha = (k_1 + k_2)z_p - (\omega_1 + \omega_2)t$  with  $z_p$  the position of the particle,  $C_1 = \text{Re}(A) \text{Re}(B) - \text{Im}(A) \text{Im}(B)$  and  $C_2 = \text{Re}(A) \text{Im}(B) + \text{Im}(A) \text{Re}(B)$ . In the limit of a point-like particle, the expression of the force is obtained making  $\sigma \rightarrow 0$  in Eq. (23) or by substituting the Gaussian potential  $\mathcal{U}_p(\mathbf{r} - \mathbf{r}_p)$  to a delta potential  $\delta_p(\mathbf{r} - \mathbf{r}_p)$  in Eq. (6).

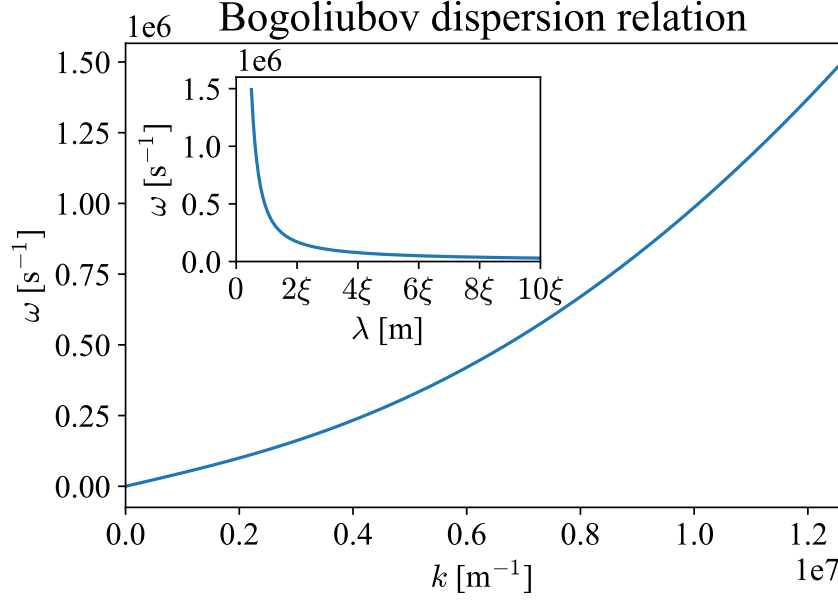


Figure 4: Angular frequency,  $\omega$ , dependence on the wave number,  $k$ , for wave lengths,  $\lambda$ , between  $\xi/2$  and  $10\xi$ . The small plot shows how  $\omega$  changes as a function of  $\lambda$  taking into account the relation  $k = 2\pi/\lambda$ . Standard values of  $m_B = 6 \times 10^{-27}$  kg,  $n_0 = 10^{20}$  m $^{-3}$  and  $g_B$  calculated from Eq. (2) with  $a_s = 5.8$  nm [1] have been used.

Assuming weak velocity variations we can calculate the velocity of the BEC with Eq. (9) and the force exerted on the impurity given by Eq. (8), in the approximation in which the particle does not alter the fluid:

$$F_p(t) = \frac{\hbar}{\mu_0} g_p (k_1 - k_2) \left[ \omega_1 + \omega_2 - \frac{\hbar}{\rho_0} (k_1^2 - k_2^2) (C_1 \cos \alpha + C_2 \sin \alpha + \lambda) \right] (C_1 \sin \alpha + C_2 \cos \alpha) \quad (24)$$

with  $\lambda = (k_1|A|^2 - k_2|B|^2)/(k_1 - k_2)$ .

Fig. 5 shows the force exerted on an impurity at rest in the center of the cylinder where the condensate is confined,  $z_p = 5\xi$ . Panel (A) gives the exact force obtained with Eq. (6) for a wide variety of wave numbers. The force is sinusoidal and the period changes minimally between plots. Interestingly, as  $k_1$  and  $k_2$  increase or the wavelengths reduce, the force is smaller. This feature is due to the negative exponential term in Eq. (23), which disappears in the limit  $\sigma \rightarrow 0$  for a point-like particle as shown in panel (B). Comparing this panel with panel (A), we observe that the force is greater as the effective size of the impurity decreases.

In the case of two opposite travelling waves with the same wave number and angular frequency, the force acting on the impurity, given by Eq. (6), is  $F_p(t) = 4\mu_0 g_p k e^{-2\sigma^2 k^2} (C_1 \sin \beta + C_2 \cos \beta)$  being  $\beta = 2(kz_p - \omega t)$ . However, in the weak velocity variations approximation, showed in panel (C), we get no net force acting on the particle as the factor  $(k_1 - k_2)$  of Eq. (24) becomes zero. That fact describes an imprecise approximation for the system under study. Therefore, the behaviour described in Eq. (23) is opposed to the one of Eq. (24) where the smaller the wave numbers, the smaller the force on the impurity.

For plotting solutions of Eq. (24) and Eq. (23) in Fig. 5, the condition  $\delta n(\mathbf{r}, t) \ll n_0$  must be satisfied in order to achieve small perturbations of the homogeneous state of the condensate introduced by the impurity. Following Madelung transform, we can approximate  $\delta\psi \sim \sqrt{\delta n}$  and the previous condition rewrites as  $\delta\psi \ll \sqrt{n_0} \sim 10^{10}$  m $^{3/2}$ , considering  $n_0 \sim 10^{20}$  m $^3$ . Then, the modulus of amplitudes  $A$  and  $B$  in the wave solution  $\psi = Ae^{i(k_1 z - \omega_1 t)} + B^* e^{-i(k_2 z - \omega_2 t)}$  must be much less than  $10^{10}$  m $^{3/2}$ . The values  $|A| \sim |B| \sim 10^6$  m $^{3/2}$  have been chosen.

## 4 Conclusions

We have studied the motion of an impurity in a 3D BEC under a gravity field and a sound-wave field. In each situation the forces acting on the particle have been calculated and compared with forces of classical fluid dynamics.

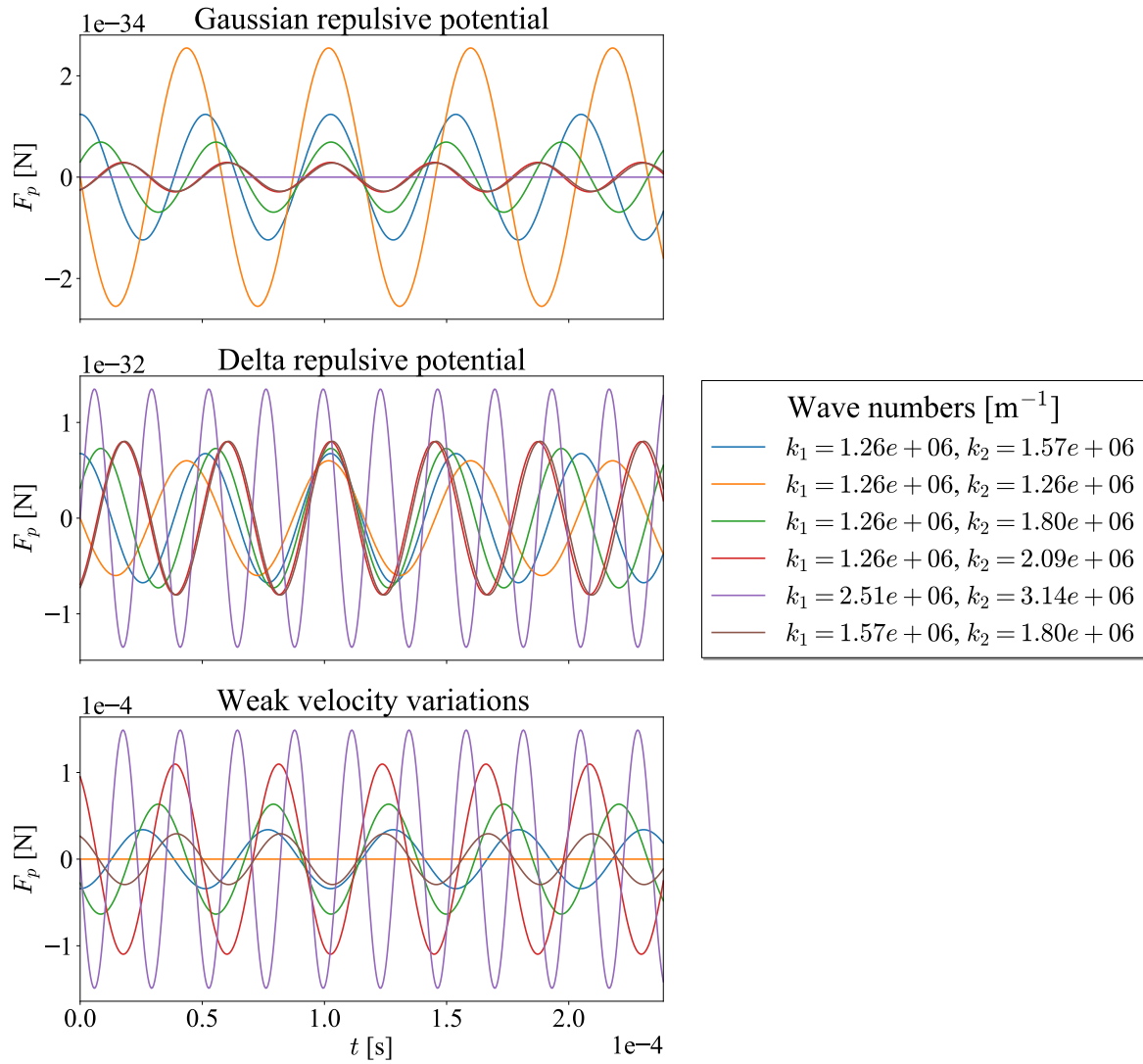


Figure 5: It is represented the 1D force the BEC exerts on an impurity of size  $\sigma \sim \xi$  and located at  $z_p = 5\xi$ , as a function of time for different cases. Panel (A) gives the exact force given by Eq. (6) assuming a gaussian repulsive potential. Panel (B) represents the force experimented by the particle in the limit  $\sigma \rightarrow 0$ , i.e: a delta potential. Finally, panel (C) shows the approximation of weak velocity variations in which the force is calculated with Eq. (8). For plotting we have assumed real values of the amplitudes  $A$  and  $B$ ,  $C_2 = 0$ , and  $C_1 = 10^{12} \text{ m}^{3/2}$ .

When the condensate is affected by an external gravitational potential, exits a density gradient which causes a buoyancy force in any test particle introduced in it. If quantum pressure is neglected, the density profile is linear and decreasing with height. Although it is not a coherent result, because it does not vanish at the walls of the cylinder, it is useful to compare with the case when quantum pressure is considered. Then, in that case, the density profile is not linear near the base and the top of the cylinder and it fits the boundary conditions. Therefore, far from the walls, where quantum pressure is insignificant, we observe a linear behaviour, as expected.

On the other hand, we have shown that the force exerted by the BEC on the impurity is reasonably related to the buoyancy force term studied by Maxey and Riley in [2] except that the coefficient of the mass of the fluid fitting the volume of the impurity is substituted by  $g_p$  [3]. We also have shown how buoyancy force considering quantum pressure has a constant value far from the walls, which matches the expected value when quantum pressure is neglected (for small values of the dimensionless parameter  $k$ ). Not only the homogeneous BEC exerts a force on the impurity, the latter also perturbs the nearby condensate causing other forces. One future line of study would be to solve Eq. (18) and obtain a more accurate density profile to calculate this forces the particle introduces.

The other part of the paper has consisted of an impurity immersed in a sound-wave field. We

have obtained analytical expressions for the force experienced by a test particle using Eq. (6) and Eq. (8). The latter equation is only useful when considering weak velocity variations. Unfortunately, we have seen this approximation has some incompatibilities with the exact force given by the Ehrenfest theorem. Maybe Eq. (7) does not take into account quantum pressure. It would be nice to study in which cases Eq. (7) does a good approximation.

Finally, another interesting extension of this paper would be to study a 3D condensate at low temperature ruled by the damped Gross-Pitaevskii equation as done in [4] and comparing the forces with the classical ones by using the damped-hydrodynamic form of the previous equation, given by [6].

## 5 Appendix

Let derivate Eq. (9) starting from the Madelung transform  $\psi = \sqrt{n}e^{iS}$  (where we have omitted the variable dependences to simplify notation). Some easy algebraic manipulation leads to:

$$S = \frac{1}{i} \ln \left( \frac{\psi}{\sqrt{n}} \right) \quad (25)$$

where using the definition of the density number  $\sqrt{n} = |\psi| = \sqrt{\psi\psi^*}$ , becomes:

$$S = \frac{1}{2i} (\ln \psi - \ln \psi^*) . \quad (26)$$

The next step is to take the gradient of both sides of Eq. (26):

$$\begin{aligned} \nabla S &= \frac{1}{2i} (\nabla \ln \psi - \nabla \ln \psi^*) \\ &= \frac{1}{2i} \left( \frac{\partial \ln \psi}{\partial \psi} \nabla \psi - \frac{\partial \ln \psi^*}{\partial \psi^*} \nabla \psi^* \right) \\ &= \frac{1}{2i} \left( \frac{\nabla \psi}{\psi} - \frac{\nabla \psi^*}{\psi^*} \right) \\ &= \frac{1}{2i} \frac{\psi^* \nabla \psi - \psi \nabla \psi^*}{\psi \psi^*} \\ &= \frac{1}{n} \text{Im}(\psi^* \nabla \psi) . \end{aligned} \quad (27)$$

Finally, with Eq. (3) and Eq. (27) we easily obtain Eq. (9) taking into account that  $\rho = m_B n$  (or  $\rho_0 = m_B n_0$  in the case when the external potential is zero).

## Acknowledgments

The autor of the paper would like to acknowledge Emilio Hernández-García and Cristóbal López for their help, critical view and discussions.

This work was supported by the SURF@IFISC fellowship.

## References

- [1] Barenghi, Carlo F. and Parker, Nick G. (2016). A Primer on Quantum Fluids. Springer.
- [2] Maxey M. R. and Riley J. J. 1983 Phys. Fluids 26 883-9
- [3] Jonas Rønning et al 2020 New J. Phys. 22 073018
- [4] Astrakharchik G.E. and Pitaevskii L.P. 2004 Phys. Rev. A 70 013608
- [5] [https://en.wikipedia.org/wiki/BoseEinstein\\_condensate](https://en.wikipedia.org/wiki/BoseEinstein_condensate)
- [6] Bradley A S, Gardiner C W and Davis M J 2008 Phys. Rev. A 77 033616